Title
AN OBSERVATION OF THE SUBMILLIMETER COSMIC BACKGROUND SPECTRUM

Author
Woody, David Paul.

Publication Date
1975-11-01

LBL-4188

AN OBSERVATION OF THE SUBMILLIMETER COSMIC BACKGROUND SPECTRUM

David Paul Woody
(Ph. D. thesis)

November 13, 1975

Prepared for the U. S. Energy Research and Development Administration under Contract W-7405-ENG-48

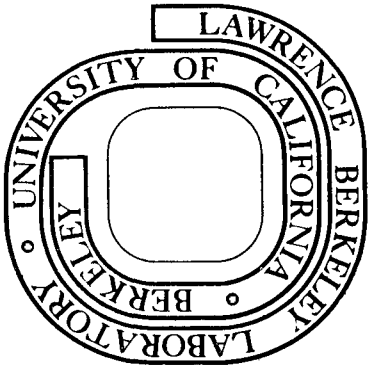

LBL-4188

DISCLAIMER

TABLE OF CONTENTS

LIST OF FIGURES

LIST OF TABLES

AN OBSERVATION OF THE SUBMILLIMETER COSMIC BACKGROUND SPECTRUM

David Paul Woody

Materials and Molecular Research Division, Lawrence Berkeley Laboratory
and Department of Physics, University of California
Berkeley, California 94720

ABSTRACT

We describe an experimental measurement of the spectrum of the submillimeter cosmic background radiation. The experiment consists of measuring the night sky emission at an altitude of 39 km, correcting for the atmospheric molecular line emission, and placing limits on the contamination from sources of continuum radiation such as the apparatus itself and the earth. The observations were made on 24 July 1974 using a fully calibrated liquid-helium-cooled balloon-borne spectrophotometer. Important features of the apparatus include a cooled antenna, a polarizing interferometer, and a germanium bolometric detector. The characterization of the spectrophotometer includes the large angle response and emission of the antenna.

The calibration of the instrument and corrections to the observed sky spectrum are based on measurements made during the flight. A simple model of the molecular line emission is used to determine the atmospheric contribution. The resulting spectrum covers the frequency range from 4 to 17 cm^{-1} and establishes that the cosmic background radiation follows the high frequency quantum cutoff for a 3K blackbody. A blackbody temperature of $2.99\ ^{+.07}_{-.14}$ K is deduced from our data.

We also analyze the present status of the cosmic background observations, which span more than three decades in frequency, and conclude that they are all consistent with a blackbody temperature of $2.90 \pm .04$K ($\pm 1\sigma$). This firmly supports the Big Bang cosmological model of the universe.

I. INTRODUCTION

The universe is apparently filled with radiation characteristic of a 3K blackbody. The discovery and measurement of this Cosmic Background Radiation (CBR) is one of the most fasinating developments in observational cosmology. The only cosmological model which satisfactorily explains the existence of this radiation is the "Big Bang" theory of the universe. The CBR, according to this theory, is a remnant from the Primordial Fireball. Firmly establishing the spectrum of the CBR will aid in understanding the details of the evolution of the universe and will place severe limits on any proposed cosmological model.

This paper describes the first successful measurement of the submillimeter CBR spectrum. The data were obtained on July 24, 1974 using a cooled balloon-borne spectrophotometer. The data show that the CBR has the spectral shape and intensity of a 3K blackbody in the frequency range from 4 to 17 cm^{-1}. The results have been published by Woody, Mather, Nishioka, and Richards (1975).

A. Elementary Theory

The theory of the Primordial Fireball has been extensively treated in the literature. Peeble's book, Physical Cosmology (1971), gives an excellent description of the accepted "Big Bang" cosmological model and its relationship to the observed universe. A lengthy chapter is devoted to the Primordial Fireball. The monumental works by Weinberg (1972) and Misner, Thorne, and Wheeler (1973) cover the general relativistic aspects of cosmology in great detail.

Historically, the first discussion of the behavior of blackbody radiation in a nonstatic universe was given by Tolman (1934, p.427). As early as 1948, Alpher and Herman (1948) calculated a value of 5K for the present temperature of the CBR. The identification of the first measurement of the CBR (Penzias and Wilson, 1965) as the remnant from the Primordial Fireball was made by Diche, Peebles, Roll, and Wilkinson (1965). They used the measured radiation temperature and an estimated helium abundance to calculate the thermal history of the universe.

"Big Bang" cosmology is based on the assumption that the universe is homogeneous and isotropic. These assumptions together with Einstein's gravitational field equations yield the equations which govern the evolution of the universe. In comoving coordinates these equations are

$$\dot{R}^2 + k = \frac{8\pi}{3} G\rho R^2$$

$$\frac{d}{dR}(\rho R^3) = -3PR^2 \qquad \text{(I.1)}$$

(Weinberg, 1972,p.472). P and ρ are the pressure and density of the universe while R is the expansion parameter which tells how the distance between points fixed to the matter of the universe scales; ie. the scale size for comoving coordinates. k is a constant equal to -1, +1 or 0 which determines whether the universe is open (will expand forever), closed (will eventually collapse upon itself) or exactly in between (will expand forever according to the Einstein-de Sitter model). The evolution of the universe is determined once the equation of state (relationship between density and pressure) and the initial conditions

are specified. Since the expansion parameter, R, must be either increasing or decreasing, a static universe is precluded by these equations.

Observation of the relationship between red-shift and distance for distant galaxies indicates that the universe is presently expanding. An extrapolation back in time predicts that the universe was denser and hotter in the past and that it possibly started near a singularity of infinite density and temperature. Fairly reliable extrapolations have been made back until the temperature was $\approx 10^{12}$K. At this temperature, the populations of the elementary particles (photons, neutrinos, muons , electrons, nucleons, etc.) were in thermal equilibrium.

The evolution can be traced forward from this time (some 10^{-4} sec after the singularity). The unstable particles, such as muons , annihilated or decayed as the universe expanded and the thermal energy (kT) dropped below their equivalent rest energy (mc^2). There were only photons, neutrinos, electrons, protons, and a few light nuclei (^{2}H and He) left by the time the temperature had dropped to $\approx 3\times 10^3$ K ($\approx 10^{12}$ sec after the singularity); at which time the electrons combined with the protons and nuclei to form neutral atoms. Previous to this time, the photons were kept in thermal equilibrium with the matter by various annihilation, bremstrahlung, and compton processes. This was also about the time that the particle rest energy started to dominate the radiation energy in determining the expansion rate. With only neutral atoms present, the interaction between the 3,000K blackbody radiation and the matter became limited to those photons with energy

equal to the resonant atomic transitions or greater than the ionization energy. Thus, the radiation and matter became effectively decoupled and they evolved separately; the matter formed galaxies and stars, while the photons (the Primordial Fireball) became the CBR we see today.

The evolution of the Primordial Fireball after it became decoupled from the matter can be followed by examining the covariant photon distribution function. This is the photon number density in phase space (momentum and position). It is measured at the observer's position and is a function of the momentum, $\vec{p}$, of the photons as seen by the observer. It reduces to a function of the energy, $E=|\vec{p}|$, for an isotropic distribution. An invariant scalar quantity, $N(\vec{p})$, is obtained if the distribution function is multiplied by a contravariant phase space volume element. If the volume used is that of a single quantum mode, h^3, then the scalar quantity is just the photon occupation number. Thus the number of photons in any mode remains constant as the universe evolves, although the momentum or energy of the mode may change. This can be derived rigorously by applying Liouville's theorem in curved spacetime to the system of noninteracting photons (Misner, Wheeler and Thorne, 1973, p.584).

The energy of a photon (or mode) scales as the inverse of the expansion parameter, R, for an observer fixed to the matter of the universe (comoving coordinates). This is a geometrical effect in the homogeneous and isotropic universe and gives rise to the red-shift versus distance relation observed for distant galaxies. Thus the photon occupation number for photons of energy E_t now is given by the

occupation number at the time of decoupling for photons of energy

$$E_o = E_t \frac{R_t}{R_o} \quad . \tag{I.3}$$

The occupation number for a blackbody retains its blackbody character as the universe expands. Initially, it is given by Bose-Einstein statistics

$$N(E_o,T_o) = \left[\exp\left(\frac{E_o}{kT_o}\right) - 1\right]^{-1} \quad . \tag{I.4}$$

At a later time, the occupation number is given by

$$\begin{aligned} N(E_t) &= N(E_o,T_o) \qquad (I.5) \\ &= \left[\exp\left(\frac{E_o}{kT_o}\right) - 1\right]^{-1} \\ &= \left[\exp\left(\frac{E_t \frac{R_t}{R}}{kT_o}\right) - 1\right]^{-1} \\ &= \left[\exp\left(\frac{E_t}{kT_t}\right) - 1\right]^{-1} \\ &= N(E_t, T_t) \end{aligned}$$

where

$$T_t = T_o \frac{R_o}{R_t} \quad . \tag{I.6}$$

Hence, the Primordial Fireball remains a blackbody but has a temperature which scales as the inverse of the scale parameter. This transformation conserves the number of photons and entropy, but does not conserve energy; the photons do work against the expanding universe.

This same analysis can be applied to an observer moving relative to the comoving coordinate system. In this case, an anisotropic Doppler shift is seen. The observer still measures radiation characteristic of a blackbody, but at a temperature which is a function of the direction of observation

$$T(v,\theta) = T_o \frac{\left(1 - \frac{v^2}{c^2}\right)^{1/2}}{(1 - \frac{v}{c}\cos\theta)} \quad . \qquad (I.7)$$

The CBR plays a key role in establishing a self consistent picture of the origin of the universe. Many of the events in the early history of the universe occurred over a relatively small temperature range, and a measurement of the present CBR temperature establishes a relationship between the temperature and density throughout the evolution of the universe. For example, the formation of neutral atoms occurred at a temperature of ≈3,000K which is 10^3 higher than the present radiation temperature. Thus the universe was 10^3 times smaller, or 10^9 times more dense, then than it is now.

Another critical point was at a temperature of $\approx 10^{10}$K when the thermal creation of electrons and positrons stopped and the neutrons began to decay. The expansion rate and density of the universe at this time determines how many neutrons form ^{2}H and He nuclei before decaying. The helium abundance is fairly insensitive to the density and is predicted

to be ≈25% by mass in good agreement with observations (Peebles, 1971, p.242). The deuterium abundance is a sensitive function of the density and its measured abundance has recently been used to place limits on the present density of the universe (Gott, Gunn, Schramm, and Finsley, 1974).

B. Previous Observations

Previous measurements of the CBR can be divided into three categories: microwave radiometer measurements, indirect measurements based on interstellar molecules, and broadband submillimeter observations.

Penzias and Wilson (1965) used a ground based microwave radiometer operating at a frequency of 0.136 cm^{-1} (7.35 cm) to make the first observation of the CBR. This first measurement was quickly followed by many other ground based microwave radiometer measurements covering the range from 0.013 to 3.00 cm^{-1}. Peebles (1971, p.134) analyzes these measurements and arrives at a value of 2.72±0.08K for the CBR temperature. Although these measurements all lie on the low frequency side of the 6 cm^{-1} peak in the 3K Planck spectrum, he shows that they are sufficient to rule out a simple Rayleigh-Jeans spectrum. The microwave data tabulated by Peebles (1971, p.134) are plotted in Fig. I.1 along with the indirect measurements and the spectrum of a 3K blackbody. These measurements appear to be in good agreement with the "Big Bang" hypothesis.

The indirect measurements come from an entirely different kind of observation. The relative intensity of optical transitions from different rotational levels in interstellar molecules is measured. This yields a temperature which corresponds to the CBR temperature at the

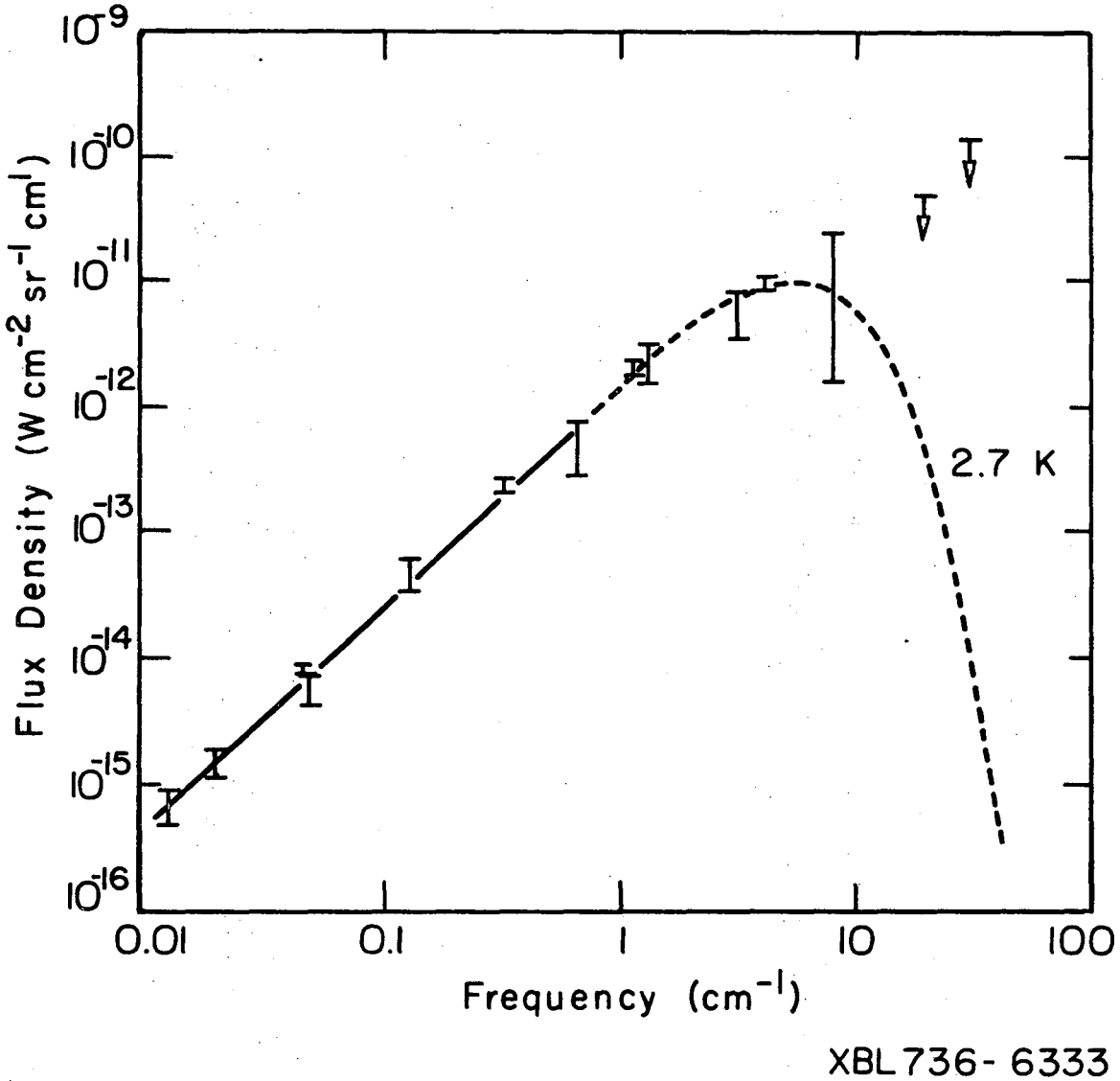

Fig. I.1. Ground based microwave measurements and indirect interstellar observations.

energy of the rotational level in the absence of any other heating mechanism. Measurements of the molecule CN gives CBR temperatures at 3.79 cm^{-1} (see tabulation by Peebles, 1971, p.134) and 7.58 cm^{-1} (Hegyi, Traub and Carleton, 1974). Upper limits are provided by CH and CH^{+} at frequencies of 17.9 cm^{-1} and 27.9 cm^{-1} (Bortolot, Clauser, and Thaddeus, 1969). These results are significant in that they are measurements of the CBR at distant points in our galaxy.

Observations on the high frequency side of the Planck curve have been particularly difficult. The feature which makes these observations important (large deviation of the Planck curve from a Rayleigh Jeans spectrum) also makes them difficult (the signal is decreasing with frequency while contaminating radiation from warm objects is still increasing). In addition, the atmospheric radiation in the submillimeter region requires that the measurements be carried out above most of the atmosphere. Three groups have been especially active in making broadband observations of the submillimeter CBR: a balloon group at M.I.T., a rocket group at Cornell, and another rocket group at Los Alamos. The published results of these groups are tabulated in Table I.1. The earliest measurements indicated that the CBR was much larger than that of a 3K blackbody. As the measurements were repeated, the deviation from a 3K blackbody diminished. The status of the broadband submillimeter measurements at three different times is shown in Figs. I.2(a), (b) and (c).

Table I.1. Broadband submillimeter observations.

Flight Date	Group	Frequency Band [cm^{-1}]	Spectral Flux[a] [10^{-12} W/cm^2 sr cm^{-1}]	Equivalent Blackbody Temperature [K]	Reference
11 Nov. 1968	Cornell	7.7-25	300^{+300}_{-150}[b]	$8.3^{+2.3}_{-1.3}$	Shivanandan, et al. 1968
29 Sept 1969	M.I.T.	1 -10	< 12	< 3.6	Muehluer and Wein, 1970
"	"	10 -12	< 300	< 7	"
"	"	12 -18	< 50	< 5.5	"
19 Dec. 1969	Cornell	7.7-25	300^{+300}_{-150}[b]	$8.3^{+2.3}_{-1.3}$	Houch and Harwit, 1970
2 Dec. 1970	"	6.7-25	70^{+5}_{-8}	---	Pipher, et al., 1971
29 May 1971	Los Alamos	1.7-12	15±7	$3.1^{+0.5}_{-2.0}$	Blair, et al., 1971
5 June 1971	M.I.T.	1 - 5.4	6.5±3.5	$2.5^{+0.4}_{-0.7}$	Muehlner and Weiss, 1973
"	"	5.4-7.9	11±5	$2.5^{+0.3}_{-0.4}$	"
"	"	7.9-11.1	6^{+4}_{-3}	$2.6^{+0.3}_{-0.2}$	"
"	"	11.1-18.5	60±10	4.3±0.2	"
29 Sept 1971	"	1 -5.4	8±3	$2.7^{+0.4}_{-0.6}$	"
"	"	5.6-7.9	12±3	2.8±0.2	"
"	"	7.9-11.1	< 6	< 2.7	"
"	"	11.1-18.5	< 20	< 3.4	"
17 May 1972	Los Alamos	1.7-13	< 16	< 4.8	Williamson, et al. 1973
"	"	1.7-17	23±17	$5.1^{+0.8}_{-1.5}$	"
"	"	1.7-33	.61±.59	$3.8^{+0.8}_{-1.9}$	"
18 July 1972	Cornell	7.7-25	< 20	---	Houch, et al. 1972
1 Oct	M.I.T.	1 -11.5	6.0±3.0	$2.5^{+0.25}_{-0.45}$	Muehlner and Weiss, 1973
"	"	1 -13.5	4.9±4.3	$2.4^{+0.45}_{-1.05}$	"
"	"	1 -18.5	< 16	< 3.6	"

[a] The spectral flux was deduced from the reported total flux and bandwidth when the spectral flux was not reported.

[b] These values were later decreased by a factor of two after recalibration.

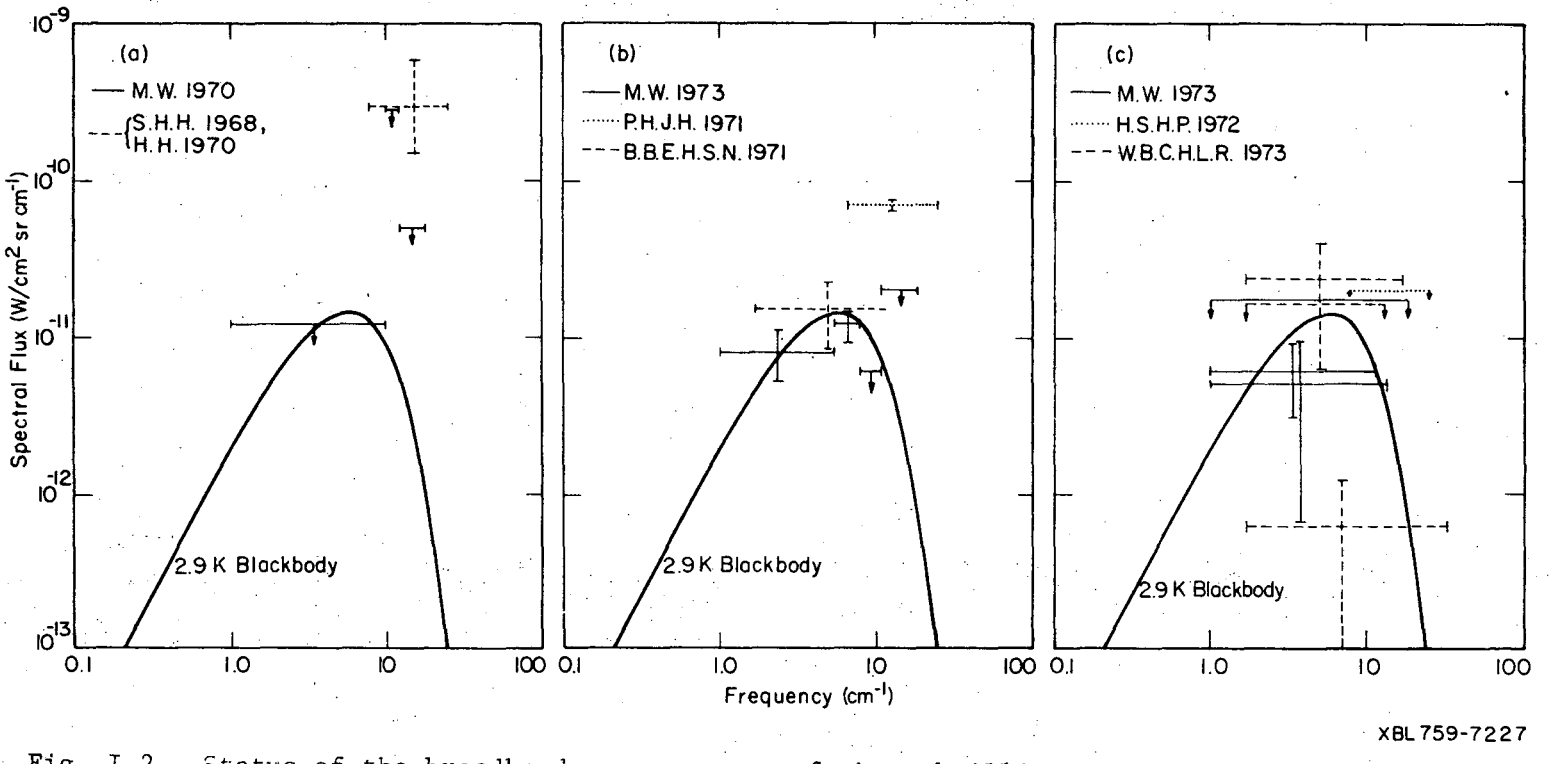

Fig. I.2. Status of the broadband measurements of the submillimeter CBR at three different times: a) November 1970, b) April 1971, c) June 1974.

Our initial motivation for undertaking a measurement of the submillimeter CBR was the early report of a large excess flux in this frequency range. As the reported measurements improved, we upgraded the quality of our instrument. It soon became apparent that eliminating contaminating sources of continuum radiation was of the utmost importance and a large effort was made in designing and characterizing our radiation collecting optics. It was also apparent that a spectrometer would be required to adequately subtract out the atmospheric emission in any balloon-borne experiment (Muehlner and Weiss, 1973). We believe our cooled spectrophotometer with its fully characterized antenna is ideally suited for this measurement.

A balloon group from Queen Mary College, University of London has recently reported the preliminary results of an observation of the submillimeter CBR (Robson, Vichers, Huizinga, Beckman, and Clegg, 1974). Their results are from the flight of a balloon borne cooled spectrometer on March 13, 1974. The spectrum they give includes a large amount of continuum emission but appears to show the CBR turning over above 9 cm^{-1} and following the curve for a ≈3K blackbody. We can not evaluate the significance of their results from the information given in the one page article.

C. Thesis Organization

The purpose of this thesis is to describe our measurement of the submillimeter CBR in enough detail that the reader will understand the major difficulties in the experiment and be able to evaluate the merits of our results.

The construction and operation of the instrument is described in chapter II. The major features of the apparatus are described, including the advantages and peculiarities of the polarizing interferometer used for Fourier transform spectroscopy. Special emphasis is placed on the characterization of the beam pattern and emission of the antenna.

Chapter III presents the raw data obtained during the flight. The first order data reduction and signal averaging are also described.

The analysis of the data is described in chapter IV. This includes the determination of the antenna emission, earthshine, and atmospheric radiation. The model used to simulate the atmosphere and the fitting procedure is discussed in detail. Finally, the observed CBR spectrum together with error limits is presented.

The last chapter discusses the significance of our measurement and its relation to previous observations. A short discussion of possible deviations from an ideal blackbody is given. Lastly, future developements, problems, and limitations of measuring the submillimeter CBR are examined.

II. APPARATUS DESCRIPTION AND CHARACTERIZATION

A. General Description

The small magnitude of the CBR flux places stringent requirements upon any apparatus used to make an absolute measurement of its spectrum. In the submillimeter frequency range the flux from a 3K blackbody falls nearly exponentially while that from a room temperature blackbody increases as the frequency squared. At 15 cm^{-1} the flux from a 300K blackbody is 18,000 times larger than that from a 3K blackbody. Hence, it is necessary that the apparatus reject by many orders of magnitude the radiation coming from warm objects such as the earth. Similarly, the apparatus itself must not contribute any significant amount of radiation to the observed spectrum. The presence of strong atmospheric emission lines in the submillimeter frequency range requires that the measurement be done above most of the atmosphere.

Much of the description of the apparatus presented in this chapter has been given elsewhere (Mather, 1974; Mather, Richards, and Woody, 1974). The work by Mather (1974) is his Ph.D. thesis. It contains a large amount of useful information, including a detailed description of the detector development and the techniques used to measure the antenna pattern. It also contains a good discussion of Fourier transform spectroscopy in the presence of noise.

The instrument we developed for measuring the cosmic background spectrum is a balloon-borne liquid helium cooled spectrophotometer. Figure II-1 is a schematic diagram of the instrument. A scale drawing

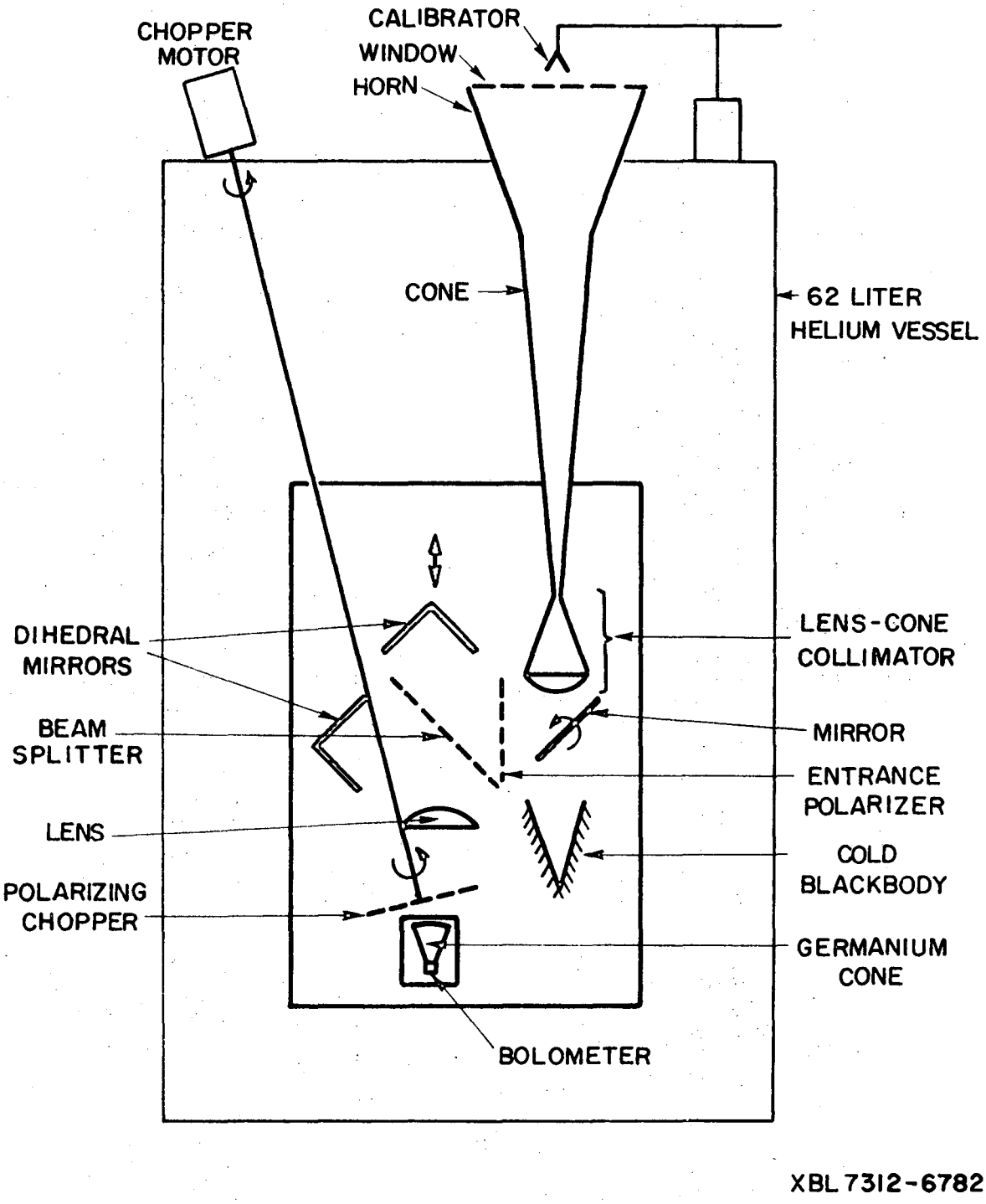

Fig. II.1. Schematic diagram of the submillimeter spectrophotometer.

is shown in Fig. II.2. The radiation is collected by the reflecting horn and cone antenna; then recollimated and sent through the polarizing interferometer; and finally focused onto the germanium bolometric detector. The polarizing interferometer is used for Fourier transform spectroscopy. The instrument is mounted in a 60 liter liquid helium cryostat. This keeps the detector and interferometer immerged in liquid helium and cools the antenna. On the ground and during the ascent, the antenna is protected from atmospheric condensation by two removeable windows at the top of the horn. Two blackbodies are used for inflight calibration.

The flight configuration is shown schematically in Fig. II.3. The cryostat containing the instrument is mounted on pivots in the balloon gondola which is suspended below the balloon. This allows the zenith angle of the instrument to be varied. A large plywood calibration body mounted on the back of the gondola serves as a calibration source when the cryostat is tilted backwards. At the same time, a small glass mirror allows us to check for atmospheric condensation in the antenna by taking photographs looking down the throat of the horn and cone. The gondola is suspended 0.6 km below the balloon by means of a let-down line deployed after launch. This keeps the 3.3×10^5 m^3 balloon well out of the field of view. The azimuthal angle is monitored by two magnetometers, but the gondola is free to rotate about the vertical axis.

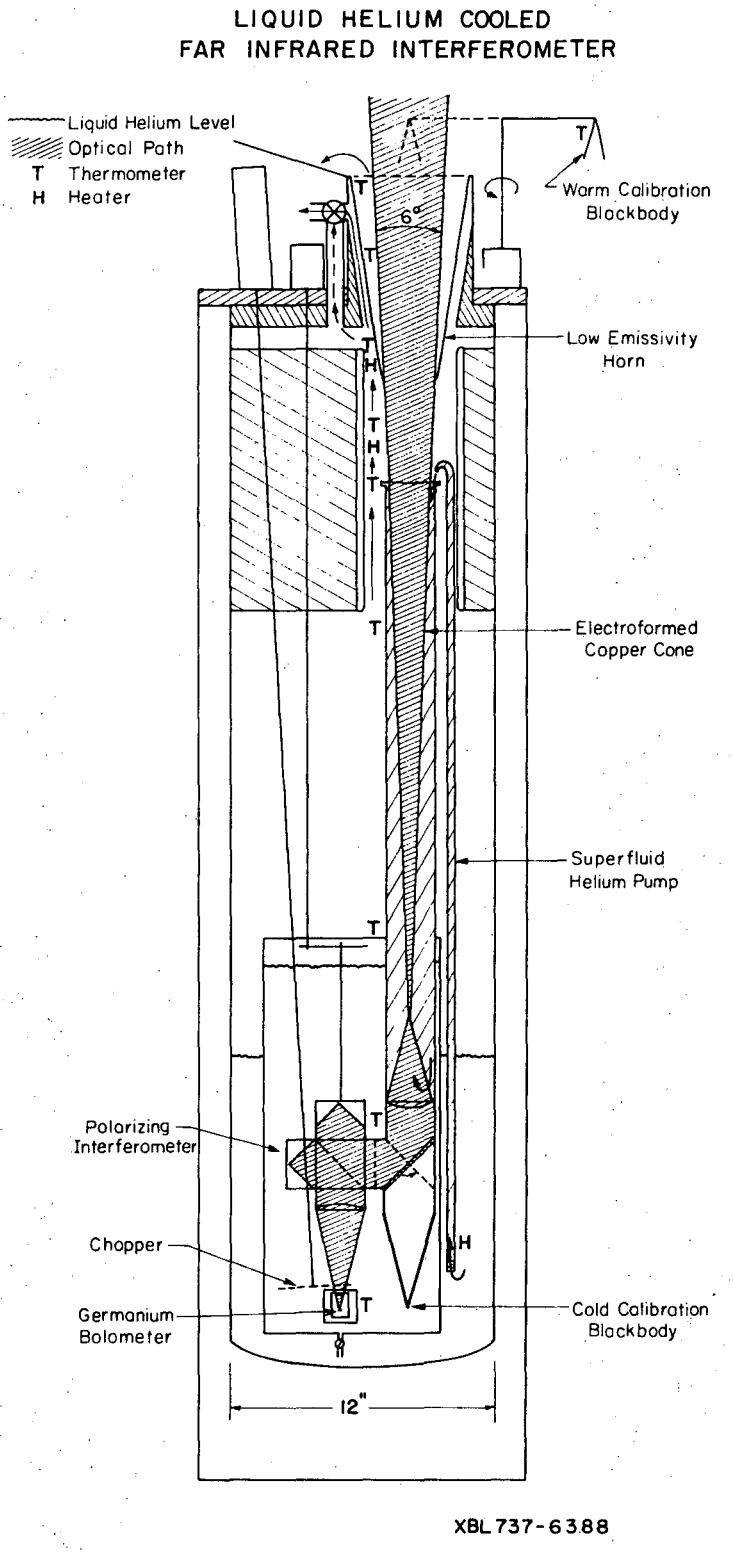

Fig. II.2. Scale drawing of the submillimeter spectrophotometer.

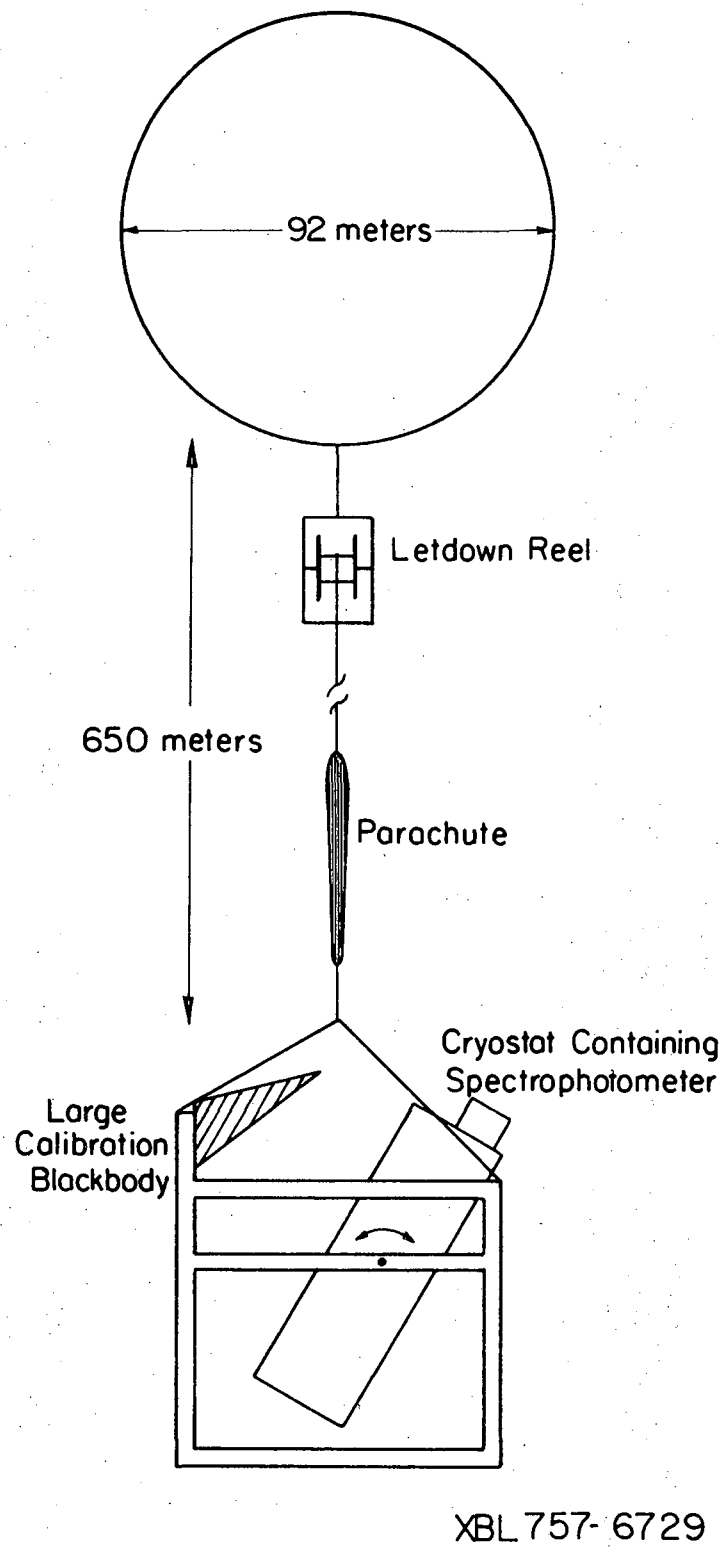

Fig. II.3. Flight configuration.

The telemetry system was developed by J. Henry Primbsch of the Space Sciences Laboratory. The data is transmitted as 8-bit words by a pulse code modulated (PCM) system with a bit rate of 8,000 bits/sec. The raw detector preamp output and chopper reference signal along with 32 channels of housekeeping data, one of which is multiplexed into 16 additional channels, are received on the ground and decoded by the ground station. The preamp and reference signals are each sampled 250 times per second. A PDP-11™ computer interfaced and programmed to do Fourier transform spectroscopy provides us with spectra during the flight. The raw bit stream is recorded on an audio recorder for replay after the flight. The command system is a tone-reed system with ten tones multiplexed to give 40 different commands. The telemetry required to drop ballast, deploy the let-down line, etc., is provided by the National Center for Atmospheric Research (NCAR) at Palestine, Texas.

B. Detector System

The detector is a doped germanium bolometer purchased from Infrared Laboratories, Inc. At the operating conditions of a 1.6K bath temperature and 17 Hz chopping frequency, the electrical noise equivalent power (NEP_e) is 6×10^{-14} $W/\sqrt{Hz}$ and the responsitivity is 0.7×10^{6} V/W. The absorptivity of the $0.8\times0.8\times0.3$ mm^3 detector element was measured to be between 0.05 and 0.2 in the frequency range from 3 to 20 cm^{-1} (Mather, 1974).

An immersion optics system is used to illuminate the bolometer. This greatly increases the radiation thruput to the bolometer over that of other methods. The method used is similar the technique developed by Vystavkin, et al. (1971) to improve the radiation coupling to InSb detectors. The radiation is coupled directly to the detector from a solid whose index of refraction matches that of the detector, thus avoiding the factor of $(n_1/n_2)^2$ reduction in solid angle given by Snell's law upon passing from a medium of refractive index n_1 to one of refractive index n_2. Germanium has a refractive index of 4, so there is a potential increase of a factor of 16 in thruput to the detector (or a decrease in area for the same thruput) using immersion optics. Since the NEP_e generally scales as the square root of the area, a factor of 4 improvement in flux sensitivity is possible. The area of germanium required to accept our system thruput of 0.25 $cm^2 sr$ is only 0.5 mm^2 using immersion optics compared to 8.0 mm^2 without.

High purity germanium is transparent to submillimeter radiation and can be used to match the refractive index of the doped germanium bolometer. In our system the radiation is collected and condensed down to a small area and large solid angle using a 2.5 cm long solid germanium total internal reflection condensing cone. The bolometer gently contacts the small end of the condensing cone. This establishes optical contact without disrupting the thermal isolation necessary for the operation of a bolometeric detector.

The condensing cone and bolometer are mounted in a vacuum can. The vacuum can has a 0.005 cm thick Mylar window. There is a 0.3 cm thick piece of Fluorogold T.M. used as a low pass scatter filter (Muehlner and Weiss, 1973) on top of the window.

The signal from the detector is amplified by a variable gain preamplier. The gain can be switched from 10^3 to 10^6 in one decade stops by the balloon command link. The balloon telemetry converts the 0 to 5 Volt analog signal into an 8-bit word giving a resolution of 0.02 Volts. The signal is sampled 250 times per sec so that the resolution for a single 2 sec measurement can be improved to 9×10^{-4} Volts if the bits are randomly exercised. At a gain of 10^5 this corresponds to 9×10^{-9} Volts resolution referred to the detector. The detector noise for a similar 2 sec measurement is 2×10^{-8} Volts.

C. Spectrometer

The spectrometer is a polarizing interferometer of the type invented by Martin and Puplett (1969). It is used for Fourier transform spectroscopy in the same way as a Michelson interferometer. In fact, the wealth of literature pertaining to Michelson interferometers and Fourier transform spectroscopy is directly applicable. An excellent book on this subject is Bell's Introductory Fourier Transform Spectroscopy (1972). A short discussion of techniques used in Fourier transform spectroscopy is given by Richards (1967).

A Fourier transform spectrometer operates by separating the incoming radiation into two beams and then coherently recombining

them to produce the output beam. Interference effects are produced by varying the relative lengths of the optical paths traveled by the separate beams. This path difference is usually controlled by a moveable mirror in one of the beam paths. The interference effects directly modulate the intensity of the exit beam in a Michelson interferometer. Whereas, only the polarization of the radiation is modulated in a polarizing interferometer, and an analyzing polarizer is required to achieve a modulation of the intensity. The modulation is proportional to $\cos(2\pi\nu x)$ in both cases, where $\nu[cm^{-1}]$ is the frequency and x [cm] is the path difference.

The intensity I(x) [Watts] as a function of path difference is called an interferogram. The interferogram for an ideal interferometer with an incident spectral intensity $S(\nu)$ [Watts/cm^{-1}] is given by

$$\begin{aligned} I(x) &= \text{const} \times \int_0^\infty T(\nu)S(\nu)d\nu + \int_0^\infty T(\nu)S(\nu)\cos(2\pi\nu x)d\nu \\ &= \text{const} \times I(0) + \int_0^\infty T(\nu)S(\nu)\cos(2\pi 2\nu x)d\nu \ . \end{aligned} \tag{II.1}$$

$T(\nu)$ is the transmission efficiency of the interferometer. The spectral intensity $S(\nu)$ is recovered by taking the inverse cosine transform

$$S(\nu) = \frac{2}{T(\nu)} \int_{-\infty}^{\infty} [I(x)-\text{const}\times I(0)] \cos(2\pi\nu x)dx \ . \tag{II.2}$$

In practice, the interferogram I(x) is sampled at discrete values of x over a finite interval. The integral in Eq. (II.2) then is approximated by a summation. The manipulations and limitations encountered in recovering $S(\nu)$ from a discretely sampled finite length interferogram are explained by Bell (1972). The important considerations are that for a path difference Δx between samplings of I(x) the maximum spectral frequency at which data can be obtained without aliasing is

$$\nu_{max} = \frac{1}{2\Delta x} \quad . \tag{II.3}$$

If N samples are taken past the zero path difference point, the maximum resolution possible is

$$\Delta\nu_{min} = \frac{1}{2N\Delta x} \quad . \tag{II.4}$$

The use of a Fourier transform spectrometer offers several advantages over other types of spectrometers. Chief among these is the multiplexing or Fellgett advantage (Fellgett, 1958; and Bell, 1972, p.23). At each point in the interferogram, information is collected over the full spectral bandwidth. However, a grating or Fabry-Perot spectrometer looks at only one resolution width at a time. For this type of experiment, where the system is limited by detector sensitivity, the multiplexing advantage gains a factor of $\sqrt{N}$ in signal to noise where N is the number of resolution elements. The Fourier transform spectrometer also avoids the problem of order sorting when spectra covering many octaves in frequency are desired.

An advantage shared with the Fabry-Perot spectrometer is a large optical thruput. The thruput of a grating spectrometer and a Michelson interferometer having the same resolving power and collimator area can be compared. The ratio of their thruputs (E) is

$$\frac{E_{Michelson}}{E_{grating}} = 2\pi \frac{F}{\ell} \; 2\tan\theta \qquad \text{(II.5)}$$

(Bell, 1972, p.22). F, ℓ, and θ are the collimator focal length, slit height, and grating angle respectively of the grating spectrometer. A typical spectrometer has $\theta \approx 30°$ and F/ℓ greater than 30, thus giving it less than 0.5% of the thruput for a similar Michelson interferometer. This is often called the Jacquinot advantage and is again important for measurements limited by detector noise.

The standard Michelson interferometer has two disadvantages which are not present in a polarizing interferometer. The constant term in front of Eq. (II.1) is $\approx \frac{1}{2} I(o)$ when it is operated in the usual slow scan mode with an external chopper for lock-in detection of the signal. Any fluctuation in the source brightness will modulate this term and introduce spurious features in the interferogram and thus produce errors in the computed spectrum. The polarizing interferometer eliminates this constant term by using the exit (or entrance) polarizer as a chopper. A description of how this is done will be given later in this section. The rapid-scan or phase modulation versions of the Michelson interferometer also eliminate this constant term (Chamberlain and Gebbie, 1971).

The other disadvantage of the Michelson interferometer is its low efficiency at low frequencies. This is a result of the dielectric film used as a beamsplitter. Its efficiency is proportional to the product of the films reflectivity and transmissivity, which are determined by the Airy formula (Born and Wolf, 1970). The efficiency is periodic in frequency, with a period proportional to one over the film thickness, and has zero efficiency at zero frequency. The beamsplitter in a polarizing interferometer is a linear polarizer. At low frequencies, the efficiency is uniformly high and goes to zero at wavelengths short compared to the polarizers grid spacing.

An exploded diagram of our polarizing interferometer is shown Fig. II.4. The optics are 5 cm in diameter. The incident radiation is linearly polarized by the entrance polarizer. This radiation is then split into two orthogonally polarized beams by a wire grid beamsplitter oriented at an angle of 45° with respect to the entrance polarizer. The beams are reflected back to the beamsplitter by corner mirrors. One of the corner mirrors is mounted on a micrometer screw so it can be translated paralled to the beam to introduce a change in the optical path length. The screw has 5 cm of travel. At the beamsplitter, the beams recombine to form the exit beam. This beam is then focused onto the polarizing chopper and detector by a teflon lens. The chopper wheel has eight sectors containing polarizers with alternating orientation.

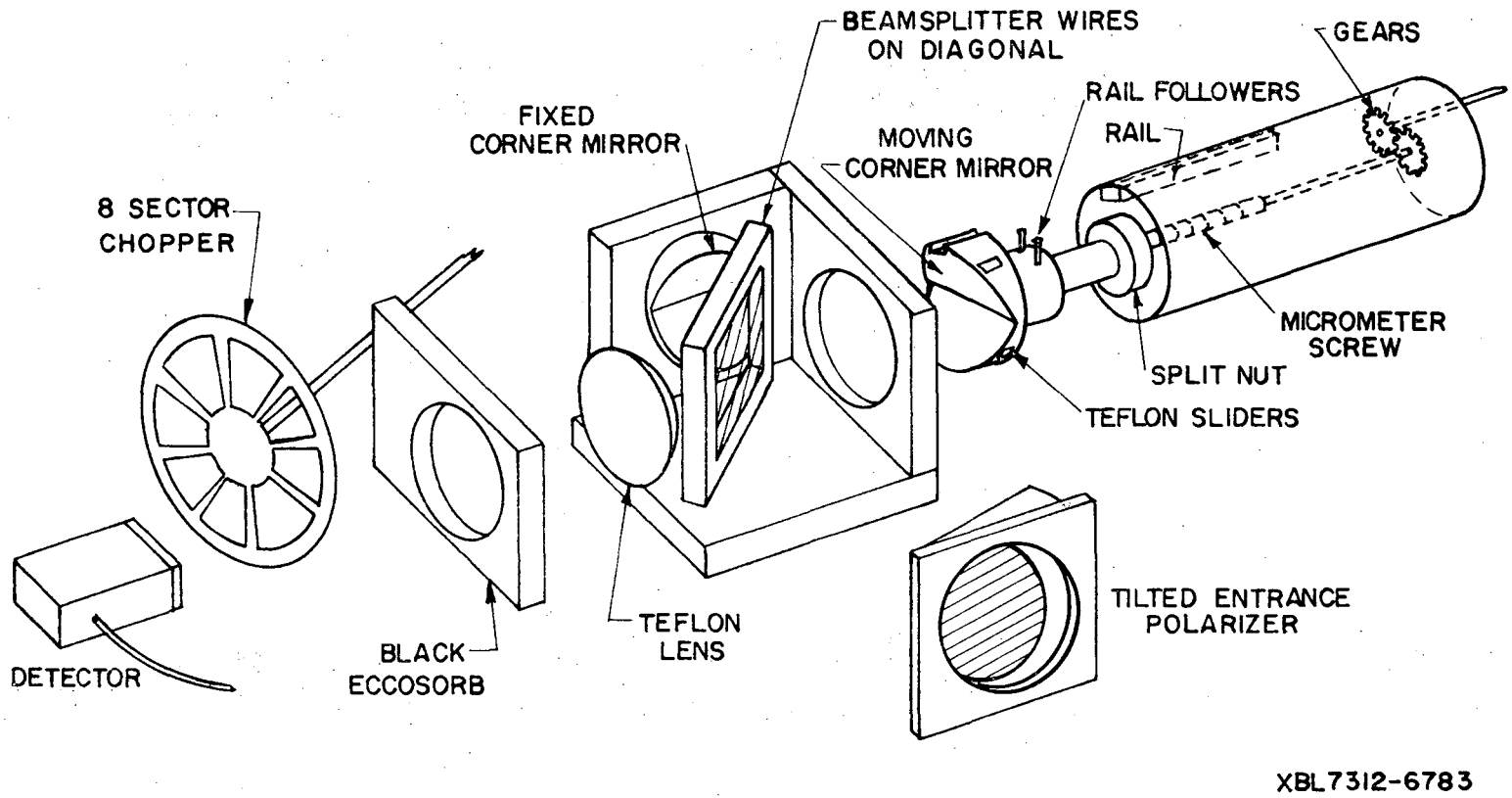

Fig. II.4. Exploded view of the polarizing interferometer.

The clever feature in Martin and Puplett's design is the use of corner mirrors to return the beams to the beamsplitter. The plane of polarization of linearly polarized radiation is reflected across the corner line of the mirror upon reflection from a corner mirror. That is, the incident and reflected beams will be orthogonally polarized if the plane of polarization of the incident beam is oriented at angle of 45° with respect to the corner line. In this way, the beam which was initially reflected from the polarizing beamsplitter will be transmitted upon its return and vice versa. The polarizer serves as a nearly perfect beamsplitter with all of the radiation from the input beam being channeled into the exit beam.

Ordinary machine shop techniques were sufficient to achieve the fraction of a wavelength tolerances necessary in constructing the interferometer. The interferometer frame was made of Invar to minimize the problems of thermal contraction. The corner mirrors are hand polished aluminum blocks. A Starrett T.M. micrometer connected to a Slo-Syn T.M. stepper motor at the top of the cryostat is used to translate the moving corner mirror. The micrometer was degreased and lubricated with teflon powder for operation in liquid helium. The chopper wheel is driven by a synchronous motor and speed reducer assembly at the top of the cryostat to give a chopping frequency of 17.1 Hz.

A finely spaced grid of linear conductors serves as a nearly ideal polarizer for submillimeter radiation. In the long wavelength limit, radiation with electric field polarization parallel to the conductors

sees the grid as a conductor and is reflected; and to a good approximation, radiation with polarization perpendicular to the conductors does not see the grid. Buchbee-Mears Inc. sells linear grids consisting of evaporated gold lines on a Mylar substrate with grid spacing as small as 25.4 μm. The entrance and chopper polarizer were made from this material.

Freestanding polarizers can also be made. It is a fairly simple task to use the automatic feed on a slowly turning lathe to wind a wire grid onto a frame. Our beamsplitter consists of 25 μm dia. tungsten wires with 153 μm spacing. The tungsten wires were first wound on a frame and then copper plated. The grid was then soldered to a flat Invar frame. These steps were necessary to build a beamsplitter which survived cycling to 1.6K and remained flat at this low temperature.

The polarization efficiency of linear wire grids can be calculated by representing the grids as lumped impedence equivalent circuits. In the long wavelength limit the efficiencies are above 99% (Casey and Lewis, 1952). Möller and Rothschild (1971, p.103) give multielement equivalent circuits valid for wavelengths less than twice the grid spacing. Using these equivalent circuits Aurbach (to be published) shows that the efficiency remains high until $\lambda \approx 2d$ at which time it quickly drops.

The alignment requirements for a polarizing interferometer are similar to those for a Michelson interferometer. At the exit port,

the wave fronts of the two beams must be parallel to within a wavelength across the whole aperture. The degradation of the interferogram for an allignment error of α radians in a circular aperture of radius r at a frequency ν is given by

$$I'(x,\nu) = \frac{2J_1(4\pi\nu\alpha r)}{4\pi\nu\alpha r} \; I(x,\nu) \qquad \text{(II.6)}$$

where J_1 is the first order Benel function (Williams, 1966). For our 5 cm dia optics and a frequency of 20 cm^{-1}, an error of α = .00045 rad. will degrade the interferogram by only 1%; while an error of α = .0061 rad. is the first zero of the Bessel function, and there is no interferogram.

The alignment of the interferometer is conveniently done is several steps. The first step is to adjust the individual corner mirrors so that the angle between the two surfaces is 90°. This is analogous to requiring that a plane mirror not be bent. One corner mirror is then mounted so that when you sight along the beam direction the corner line is at a 45° with respect to the beamsplitter wires. The other mirror is mounted in the same way but with two adjustments for orienting the corner line. Two optical flats are now placed against the freestanding wire grid beamsplitter to serve as a visible light beamsplitter. You now look through the interferometer at a distant object. There are two images corresponding to the two interferometer beams. There will be a total of four images if the corner mirror angles are not 90°. By adjusting the corner line of the second corner mirror, the two images can be made to superimpose. The

superposition of the two images must be within the ≈ .001 rad. tolerance required for efficient interference. A low magnification large aperture telescope (alignment scope) is very useful for achieving a precise alignment. The final step is to adjust the entrance and exit (chopper) polarizers so that when you sight along the beam direction the polarizer wires and beamsplitter wires are at 45° with respect to each other. The tolerances on adjusting the first corner mirror and the entrance and exit polarizers are not high since the errors only enter in second order in the transmission efficiency of the interferometer.

There are several features which are peculiar to a polarizing interferometer. These can be demonstrated by tracing the radiation through the interferometer. The electric field strength after the entrance polarizer is $|\vec{E}_{in}(\nu)| = \sqrt{S_{in}(\nu)/2}$ for unpolarized incident radiation of intensity $S(\nu)$. After the beams have been separated and recombined, the electric field in the exit beam traveling in the z-direction is

$$\vec{E}_{out}(\nu,x) = \frac{1}{2}\sqrt{S_{in}(\nu)}\,[(\gamma_x+\varepsilon_x e^{i\phi})\hat{x} + (\gamma_y e^{i\phi}+\varepsilon_y)\hat{y})] \qquad \text{(II.7)}$$

with $\phi \equiv 2\pi\nu x$. γ_x and γ_y are the efficiencies with which the desired polarizations in the separate beams are transmitted, and ε_x and ε_y are the transmissivities for the wrong polarizations. The unit vectors $\hat{x}$ and $\hat{y}$ are parallel and perpendicular respectively to the beamsplitter wires when viewed along the z-direction. An ideal interferometer has $\gamma_x = \gamma_y = 1$ and $\varepsilon_x = \varepsilon_y = 0$, in which case, Eq. (II.7) simplifies to

$$\vec{E}_{out}(\nu,x) = \frac{1}{2}\sqrt{S_{in}(\nu)}\ [\hat{x} + e^{i\phi}\ \hat{y}]\ . \qquad \text{(II.8)}$$

The $\hat{x}$ and $\hat{y}$ components come from the separate beams. It is seen that the interferometer behaves like a variable thickness birefringent medium.

The exit polarizer, which is tilted at an angle θ with respect to $\hat{x}$ direction, is used to analyze the output beam. The intensity of the transmitted radiation is given by

$$\begin{aligned} S_{out}(\nu,x,\theta) &= \frac{1}{4} S_{in}(\nu)\left|(\gamma_x+\varepsilon_x e^{i\phi})\cos\theta + (\gamma_y e^{i\phi}+\varepsilon_y)\sin\theta\right|^2 \\ &= \frac{1}{4} S_{in}(\nu)[(\varepsilon_x\cos\theta+\gamma_y\sin\theta)^2 + (\gamma_x\cos\theta+\varepsilon_y\sin\theta)^2] \qquad \text{(II.9)} \\ &+ \frac{1}{2} S_{in}(\nu)(\varepsilon_x\cos\theta+\gamma_y\sin\theta)(\gamma_x\cos\theta+\varepsilon_y\sin\theta)\cos(2\pi\nu x). \end{aligned}$$

This can be integrated over frequency to obtain an interferogram of the same form as Eq. (II.1). For the ideal interferometer with $\theta=45°$, Eq. (II.9) simplifies to

$$S_{out}(\nu,x,45°) = \frac{1}{4} S_{in}(\nu)\ [1 + \cos(2\pi\nu x)]\ . \qquad \text{(II.10)}$$

The constant term can be eliminated by looking at the difference between $S_{out}(\nu,x,45°)$ and $S_{out}(\nu,x,135°)$; i.e., using a polarizing chopper. The resulting interferogram is then given by

$$I(x) = \int_0^\infty \frac{1}{2} S_{in}(\nu)\cos(2\pi\nu x)d\nu\ . \qquad \text{(II.11)}$$

Equation (II.9) can be expanded about the ideal conditions to determine the effects of imperfect polarizers, etc. Using the expansions $\gamma_x = \gamma(1-\beta)$, $\gamma_y = \gamma(1+\beta)$, $\varepsilon_x/\gamma = \varepsilon_y/\gamma = \varepsilon$, $\theta_1 = \frac{\pi}{4} + \delta_1$ and $\theta_2 = \frac{3\pi}{4} + \delta_2$ and keeping only the leading terms, one gets

$$I(x) = \int_o^\infty \frac{1}{2}\gamma^2 S_{in}(\nu)[(2\beta(\delta_1+\delta_2) + 2\varepsilon) + (1-\beta^2+\varepsilon^2-\delta_1{}^2-\delta_2{}^2)\cos(2\pi\nu x)]d\nu. \tag{II.12}$$

β is a measure of the beam imbalance; γ is the interferometer transmission efficiency; ε is one minus the polarization efficiency of the beamsplitter; and δ_1 and δ_2 are the exit polarizer (chopper) alignment errors. These errors are separate from the alignment error α. Only ε is frequency dependent; being zero for $\nu d \ll 1$ and increasing as νd goes to one. This shows that there can be a constant term in the interferogram (Eq. II.1), but one which is only proportional to the deviations from an ideal polarizing interferometer.

There is an additional feature which adds to the usefulness of a polarizing interferometer. An opaque chopper at the position of the analyzing polarizer will yield a measurement of the total input intensity since only the polarization and not the beam intensity is modulated by the path difference x. In our experiment the spokes on chopper wheel holding the alternating pieces of polarizer serve as an opaque chopper. These spokes appear twice for each pair of analyzing grids; thus the signal at twice the fundamental chopping frequency is proportional to the input intensity. This technique is used to monitor the integrated spectral intensity while recording the

interferogram with the same detector.

D. Antenna System

The antenna used to collect the radiation is a critical part of the instrument. Radiation from objects outside the apparatus, such as the balloon or earth, must be rejected; and at the same time the antenna itself must not emit a significant amount of radiation into the spectrometer. Minimizing the radiation from extraneous objects requires that the antenna sidelobes, caused principally by diffraction, be suppressed. The antenna emission problem is one of making a low loss, cooled antenna. The antenna we use consists of two parts. A long, cooled cone defines the primary beam in the limit of geometrical optics. Above the cone, an apodizing horn reflects the diffraction sidelobes back into the primary beam.

The 70 cm long primary cone is made from electroformed copper. It has an entrance aperture 6.0 cm in diameter and a 0.3 cm diameter exit aperture. The cone half-angle is 2.2°. It serves as a nearly ideal light condenser; providing Lambertian illumination at the exit aperture, and defining a nearly rectangular beam profile. Möller and Rothschild (1971,p.72) describe the properties of such conical light condensers, and Mather (1974) gives a simple explanation of their characteristics in terms of symmetry and conservation of angular momentum. The smallest possible beam half-angle for a 6.0 cm aperture with a thruput of 0.25 $cm^2 sr$ is 3.1°. For our cone, the extremal limit for the geometrical rays is 5.8° off axis. The whole cone is cooled to liquid helium temperatures.

The apodizing horn starts from the top of the primary cone at a cone half angle of 8.4° and continues for 25 cm, giving it a 15 cm diameter entrance aperture. This horn is outside the geometrical limit of the primary beam. Only those rays which are diffracted at the 6 cm aperture interact with the horn. The geometrical limit for rays accepted by the horn is 37° off-axis. Thus, rays coming from outside this angle must be diffracted twice before they reach the spectrometer. The horn makes the transition from ambient temperature to liquid helium temperatures. It was constructed from a laminated sheet composed of 125 μm stainless steel, ≈ 25 μm copper and 50 μm polyetheylene. The stainless steel provides mechanical strength with low thermal conductivity, the copper gives a high reflectivity surface, and the polyethylene serves as a proreflection coating for grazing incidence rays. The construction technique is described in Appendix A and the theory of the proreflection coating is discussed later in this chapter.

1. Antenna Pattern

The antenna pattern for this system has been measured out to nearly 70° off-axis. The technique used to make the measurements is described by Mather (1974) and Mather, Richards and Woody (1974). It employed a large cylindrical reflector to greatly increase the effective solid angle of a small spherical source. A flask of liquid nitrogen served as a broadband thermal source with a piece of Fluorogold$^{T.M.}$ at the detector to serves as a low pass scatter filter. The high frequency limit was $\approx 40\ cm^{-1}$ with a weighted average frequency of $18\ cm^{-1}$. The measured antenna pattern is plotted in Fig. II.5. The vertical axis, which covers

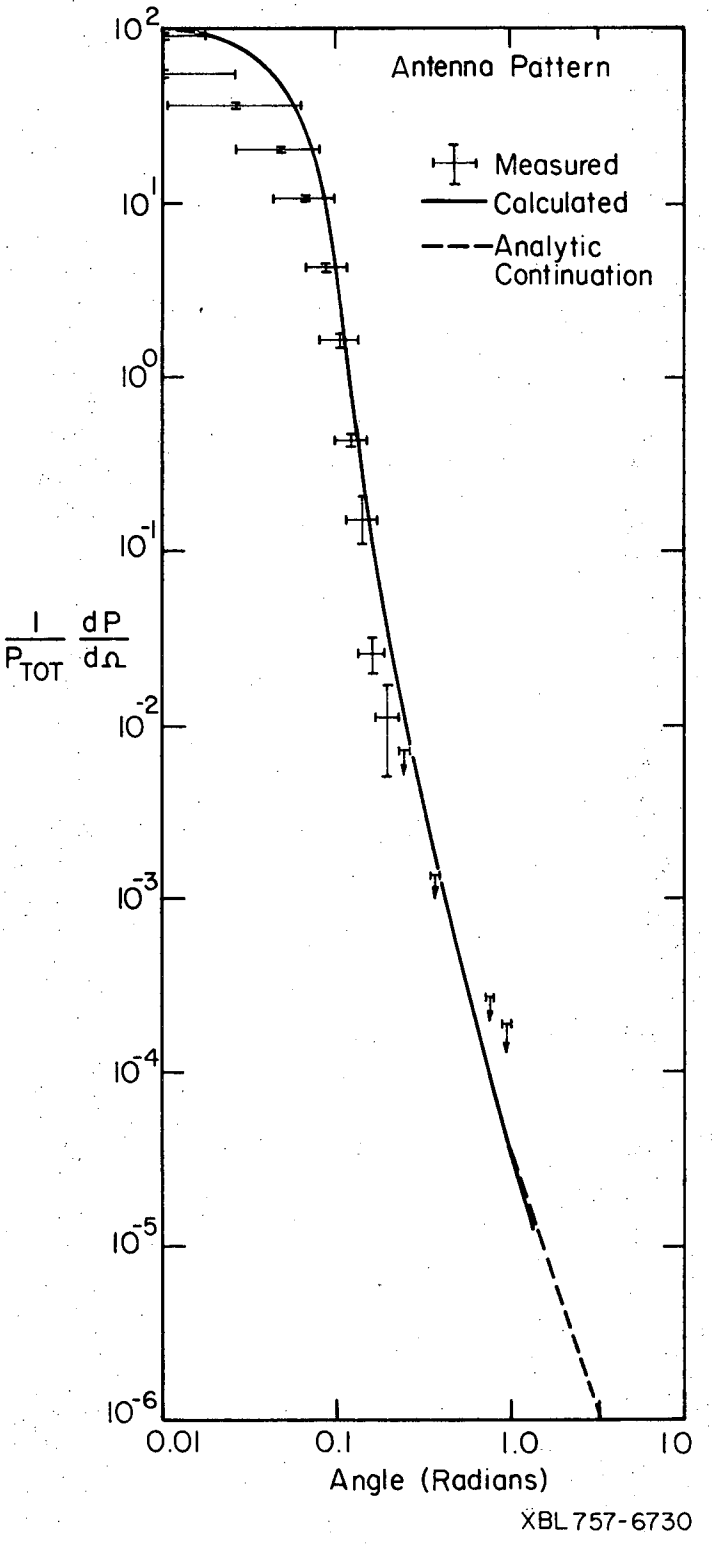

Fig. II.5. Theoretical and measured antenna pattern.

eight decades, is the response to a point source normalized such that the integral over 4π steradians gives unity.

Theoretical calculations of the antenna pattern have been made using a simplified model of the diffraction effects. The model is a modification of the theory of geometrical diffraction developed by Keller (1967). It allowed us to use a very efficient Monte Carlo ray training program to compute the antenna response.

Keller's theory treats diffracted rays as ordinary rays which originate at the diffracting edge. There is a scattering amplitude which determines the magnitude and phase of the diffracted ray. This scattering amplitude is a function only of the local geometry (ie. an edge, surface or point) and the wavelength. It is determined by matching the far field results for problems where rigorous diffraction calculations have been made.

Mather (1974, p.114) presents a version of this theory in terms of scattering cross sections. All the radiation coming within a distance δ of the edge is assumed to be diffracted by an angle greater than $\theta(\delta)$. The relationship between θ and δ is choosen to give results in agreement with rigorous calculations. The oscillating interference effects in the diffracted radiation are lost since there is no phase information in the scattering cross section. An interesting point of this treatment is the close agreement between $\theta(\delta)$ calculated for a circular aperture and for a straight edge.

This line of developement can be extended one step further for the purpose of ray tracing, by assigning a one-to-one relationship between the distance from the ray to the edge and the angle by which it is diffracted. A ray is traced to the plane of the aperture, its distance δ from the edges determined; its direction then altered by an amount $\theta(\delta)$; and finally traced through the rest of the optics.

We are interested in diffraction from circular apertures, so I will use the results for scalar Kirchhoff diffraction to determine the relationship between δ and θ. The diffracted power for normal incidence is

$$\frac{1}{P_{tot}} \frac{dP}{d\Omega} = (k\ a)^2 \frac{1}{4\pi} \left(\frac{1+\cos\theta}{2}\right)^2 \left| \frac{2J_1(k\ a\ \sin\theta)}{k\ a\ \sin\theta} \right|^2 \qquad \text{(II.13)}$$

where "a" is the aperture radius and $k=2\pi/\lambda$ the wavevector (Jackson, 1967, p.296). The large argument limit for the Bessel's function can be used if $a \gg \lambda$ and θ is not small. Averaging over the $\cos^2(k\ a\ \sin\theta)$ term then gives

$$\frac{1}{P_{tot}} \frac{dP}{d\Omega} = \frac{\lambda}{8\pi^2 a} \frac{(1+\cos\theta)^2}{\sin^3\theta} \quad . \qquad \text{(II.14)}$$

The same result is obtained if the following rule is used: rays which pass at a distance $\delta \equiv a-r$ from the edge are diffracted by an angle θ, where r is given by

$$r(\theta) = \left\{ a^2 - \frac{\lambda a}{\pi^2} \left[\frac{1+\cos\theta}{2\sin\theta} - \frac{\pi-\theta}{4} \right] \right\}^{1/2} \quad . \qquad \text{(II.15)}$$

In the limit $\delta \equiv (a-r) \ll a$, this simplifies to

$$\delta(\theta) = \frac{\lambda}{2\pi^2}\left[\frac{1+\cos\theta}{2\sin\theta} - \frac{\pi-\theta}{4}\right] . \qquad \text{(II.16)}$$

The antenna pattern was calculated by tracing a large number of rays through the antenna in the time reversed direction. The rays were traced through the cone starting from a Lambertian distribution of rays at the small end. Their distance from the edge was determined as they passed the junction between the cone and horn, and a corresponding diffraction angle was added to their angle off axis. These rays were then traced through the apodizing horn and similarly diffracted as they passed through the large aperture of the horn. At this point, the net angle off-axis was recorded. On the order of 10^6 rays were traced through the antenna to obtain information about the antenna pattern at large angles where the response is very small. Several sets of rays corresponding to different wavelengths were traced to provide spectral information.

The calculated and measured antenna pattern are shown in Fig. II.5. A weighted average of four wavelengths was used to approximate the broadband thermal source used in the measurements. The agreement is quite remarkable for a calculation containing no free parameters and covering six decades.

These results tempt us to apply the simplified diffraction theory to angles beyond 70° where there are no measurements. The net effect of the antenna system is to illuminate the entrance to the horn

nonuniformly. The intensity is high near the center where the geometric beam enters and tapers off to a small value near the edge; ie. the beam is apodized. The diffraction is determined by the intensity at the edge, but should have the same angular dependence as that of a uniformly illuminated hole

$$\frac{1}{P_{tot}} \frac{dP}{d\Omega} = \text{const} \times \frac{(1+\cos\theta)^2}{\sin^3\theta} \quad . \tag{II.17}$$

This angular function is closely approximated by $1/\theta^3$ from $\theta=0$ to nearly π radians. The constant is determined to be $\approx 3.5\times10^{-5}$ by fitting the measured and calculated antenna pattern to $1/\theta^3$ in the region past 0.7 radians (40°) where diffraction dominates. This is drawn as an analytic continuation of the calculation in Fig. II.5. The ray tracing calculations show that this constant scales as λ^2 as expected for double diffraction. Using 18 cm^{-1} as the weighted average frequency, the far off-axis pattern is given by

$$\frac{1}{P_{tot}} \frac{dP}{d\Omega} = 1\times10^{-2} \frac{\lambda^2}{\theta^3} \tag{II.18}$$

for λ in cm and θ in radians.

2. Antenna Emission

It is necessary to determine the emissivities of the antenna surfaces in order to calculate the contribution the antenna makes to any observed signal. The theory of reflection from a conducting medium is treated in Jackson (1967, p.222). Applying Ohm's law and Maxwell's equations, we obtain the classical result that the fields decay

exponentially from the metal surface in a characteristic distance, called the "classical" skin depth, given by

$$\delta_{cl} \equiv \sqrt{\frac{c^2}{2\pi\sigma\omega}} \quad . \tag{II.19}$$

Here ω[radian/sec] is the optical frequency and $\sigma[\text{sec}^{-1}]$ is the conductivity.* The absorption in the metal can be found by calculating the Ohmic losses in the thin surface layer. Ohm's law breaks down when the electron mean free path ℓ is much greater than δ_{cl} or the electron relaxation time τ is much longer than $1/\omega$. These situations arise in the case of good conductors at high frequencies and are referred to as the anomalous skin effect and relaxation effect regions respectively.

At 4.2K the measured D.C. conductivity of the electroplated copper cone is greater than 1.6×10^{22} sec^{-1}. This is 300 times larger than the room temperature value. Applying the simple free electron gas theory for metals (Kittel, 1966), this implies a mean free path of 1.3×10^{-3} cm and a relaxation time of 8.1×10^{-17} sec. Thus, at a frequency of 10 cm^{-1} we have $\omega\tau \gtrsim 15$ and $\ell/\delta_I \gtrsim 1.9\times10^3$, and we are well into the region where both the anomolous skin and relaxation effects are important.

There are several good articles on the relaxation and anomolous skin effects. The pioneering article is that of Reuter and Sondheimer (1948). Dingle (1953) presents some useful series expansions for doing

*All formulas in this section are given in esu.

calculations and an excellent summary and discussion is given by Pippard (1954).

The absorption and reflection properties of a semi-infinite medium can be determined if the complex surface impedence Z is known. The surface impedence of a medium filling the +z region of space for radiation with electric field in the x-direction is given by

$$Z = 4\pi \left. \frac{E_x}{H_y} \right|_{z=+0} , \qquad \text{(II.20)}$$

where E_x and H_y are the complex field amplitudes at the surface. The references mentioned above use a nonlocal integral form of Ohm's law to calculate the surface impedence. The transmissivity across the conductors surface (ie. absorptivity of the conductor) for normal incidence is obtained from the transmission line analogy

$$T = 1 - \left| \frac{\frac{4\pi}{c} - Z}{\frac{4\pi}{c} + Z} \right|^2 . \qquad \text{(II.21)}$$

$4\pi/c$ is the impedence of free space.

The surface impedence can be used to calculate an effective complex index of refraction for the conductor. The relationship between impedence Z and index of refraction n is obtained by applying the differential form of Faraday's law to a homogeneous plane wave propagating in a medium of refractive index n. The result is

$$n = \frac{4\pi}{cZ} . \qquad \text{(II.22)}$$

The Fresnel formulas can now be used to calculate the reflectivity and transmissivity at the conductor's surface. For normal incidence these agree with the transmission line formula. Dingle (1953) shows that for good conductors the complex index of refraction computed above is valid for use in the Fresnel formulas at arbitrary angles of incidence.

We have written a simple program which calculates the complex index of refraction for a metal. It is based on the series expansions given by Dingle (1953, Eqs. 6.3 and 6.4). It is valid for diffuse reflection of the electrons from the metal surface and takes into account both the anomalous skin effect and the relaxation effect. The input parameters are the electron number density, Fermi velocity and the D.C. electrical conductivity. The computer code is a subroutine in the program STRAD described in Appendix B.

A plot of the calculated absorption in room temperature copper as a function of the angle of incidence is shown in Fig. II.6. The calculation was done for a frequency of 10 cm^{-1} with the TM and TE modes treated separately. The important feature of the plot is the high absorption for the TM mode near grazing incidence. This is similar to the Brewster's angle phenomenon for reflection from glass. It occurs in metals near grazing incidence because of the very large magnitude of the index of refraction.

One way to avoid the large absorption near grazing incidence is to coat the metal surface with a dielectric. The grazing incidence rays are then refracted towards normal incidence before striking the metal.

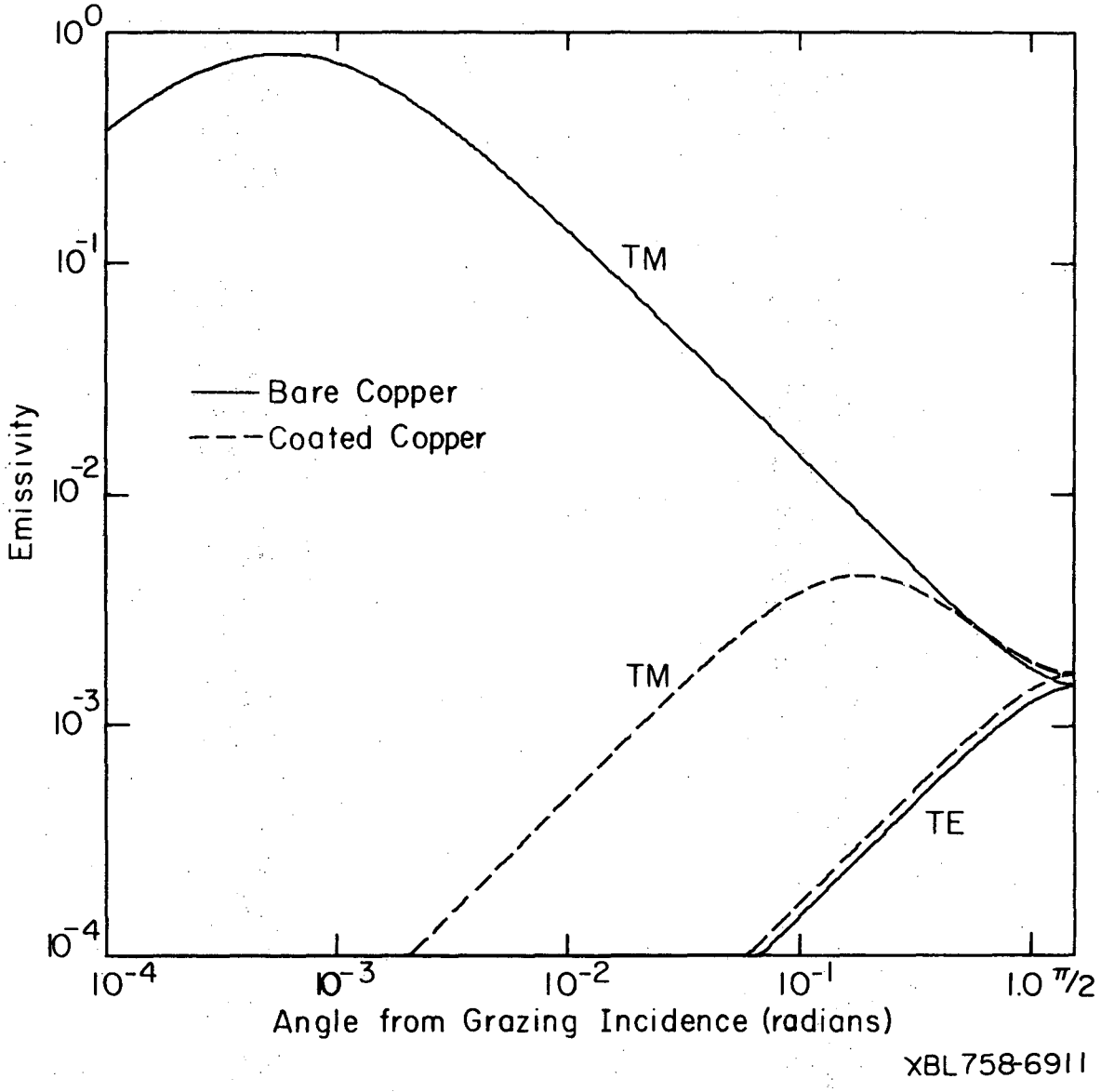

Fig. II.6. Emissivity of copper as a function of incidence angle at 10 cm^{-1}.

To examine this and similar problems, we have written a program which rigorously calculates the reflectivity, transmissivity and absorptivity in a plane stratified medium. The program is based on the method of characteristic matrices for a homogeneous medium described by Born and Wolf (p.51, 1970) and Stone (p.415,1963). Appendix B contains a description and listing of the program.

The apodizing horn is coated with 50 μm of polyethylene to decrease its emission. Its calculated absorptivity is also plotted in Fig. II.6. The polyethylene was bonded to the copper surface without additional adhesive. The recipe is given in Appendix A.

The copper cone could not be coated in this way. It was polished in a chemical polishing solution (100 ml glacial acetic acid, 100 ml phosphoric acid, 200 ml concentrated nitric acid, 0.5 gm sodium nitrate, and 0.5 gm ammonium chloride) and rinsed in a passivating solution (4 oz. of sodium dichromate, 1/2 oz. nitric acid, and 1 gal. of water). The passivating solution kept the surface shiny and had no measureable effect on the submillimeter absorption.

The emissivity of the cone and horn surfaces were measured using a cavity transmission technique. The usual method of measuring emissivities is to construct a resonant cavity of the material to be tested and measure its Q. If the cavity has only a few modes, then you can calculate the fields at the surfaces and deduce a surface impedence from the measured Q. Another approach is to construct a nearly random cavity so that the energy density will be nearly uniform and measure the transmission through the cavity. This is the technique we used.

It is broadband and useful in the submillimeter frequency range where single mode resonant cavities are difficult to construct. If the cavity is fed with a 2π steradian beam (Lambertian source) and the exit port accepts a 2π steradian beam, then the transmission can be written simply as

$$T = \frac{\text{Area of exit}}{\text{Area of exit} + \text{Area of input} + \bar{\varepsilon} \times \text{Area of cavity}} . \qquad \text{(II.23)}$$

This is just the ratio of the signal reaching the detector to that being absorbed in the cavity or lost out the cavity ports. $\bar{\varepsilon}$ is the emissity of the cavity surface averaged over 2π steradians and is given by

$$\bar{\varepsilon} = \int_0^{\frac{\pi}{2}} \varepsilon(\theta) 2\pi \sin\theta \cos\theta d\theta \qquad \text{(II.24)}$$

The exit and entrance ports should have the same area for easy normalization. A transmissivity in the easy to measure range from 10 to 90% is easily achieved by adjusting the cavity surface area.

We performed transmission measurements using the antenna itself as a cavity. The results of these measurements together with the theoretically calculated values for the emissivity are shown in Table II.1. The measured emissivities are slightly above the theoretical values. This could be a result of imperfections in the surface (roughness, impurities, strains, etc.) which increase its D.C. conductivity above that for the bulk material. Radiation leaks in the cavity would have a similar effect. The temperature and frequency dependence of the emissivities are in

Table II.1. Average Surface Emissivity of Copper

	Calculated	Measured
Bare Cu at 4.2K		
10 cm^{-1}	0.07%	0.14± .06%
30 cm^{-1}	0.13%	0.30± .09%
Bare Cu at 300K		
10 cm^{-1}	0.20%	0.28± .08%
30 cm^{-1}	0.33%	0.41± .07%
Dielectric coated Cu at 300K		
10 cm^{-1}	0.18%*	0.31± .06%
30 cm^{-1}	0.41%*	0.46± .06%

*This calculation doesn't include any loss in the dielectric.

reasonable agreement with the theory.

We can calculate the antenna emission for an arbitrary temperature profile along the antenna by combining the emissivity calculations with the ray tracing program. This calculated emission can then be compared to a measured emission. The difficulty is that it is very hard to obtain a low enough background that the cone emission can be seen. In the laboratory, a liquid helium temperature blackbody which completely covered the top of the horn would be required. The necessity of having a low emissivity window and a high thermal conductivity radiation absorber makes the construction of such a blackbody impractical. However, measurements of the antenna emission can be made during the flight. At 40 km altitude the night sky flux is small enough that the emission from a heated antenna should be measureable. Our model for the antenna emission was tested by changing the temperature profile during the flight and looking at the difference in signal. The results of this test will be discussed in Chapter IV.

E. Cryogenics

The spectrophotometer is mounted in a ≈ 60 liter liquid helium cryostat. The inside dimensions are 125 cm tall by 30.5 cm in diameter. The loss rate is only 0.25 liters/hour without the spectrophotometer inserted. With it, the loss rate is on the order of 3 liters/hour. Most of the increase in loss rate is a result of cooling the antenna.

Two superfluid helium pumps are used to transport liquid helium to the top of the copper cone and maintain the helium level in the can

containing the spectrometer and detector. These pumps operate on the thermomechanical effect of superfluid helium (Wilks, 1970,p.38). In this effect, a pressure difference across a semipermeable membrane (one which allows only the superfluid component through) can be maintained by establishing a temperature difference across that membrane. This pressure difference can be used to raise the helium level on the warm side of the membrane relative to that on the cold side and thus provide a pumping mechanism. The effect is analogous to the osmotic pressure effect in salt solutions; the temperature difference produces a gradient in the concentration of the superfluid component. The construction and operation of the pumps is described in Appendix C. The temperature drop is established by a heater which can be adjusted to determine the pumping rate. Several liters per hour of helium can be pumped at a cost of only a few tenths of a watt.

The boil off gas from the liquid helium can be used very effectively to cool parts of the antenna. A useful fact to remember is that the heat required to raise the temperature of one gram of helium gas 3.8K is the same as that required to convert one gram of liquid to gas at 4.2K. The gas flow in the cryostat can be vented past the antenna so as to aid in cooling it or diverted away so that the antenna can be warmed. There is a resistance heater at the top of the copper cone to help in heating the antenna. The temperature at the top of the cone can be varied from 3.5 to 20K during a flight by using these techniques together with turning the superfluid pumps off and on.

A third option on the gas flow is to close the normal vent tube. This forces all the gas to flow out through the antenna itself. This is necessary when the protective window over the apodizing horn aperture is removed. In this case, the outrushing helium gas is sufficient to prevent the flow of air back down the antenna where it could condense inside the cold horn and cone. A one-way valve in the normal vent path maintains a $\gtrsim 1$ torr over-pressure in the cryostat so that all leaks vent helium gas outward and do not leak air into the cryostat.

F. Calibration

The calibration procedure requires a determination of both the flux responsivity and the zero level of the spectrophotometer as functions of frequency. The flux responsivity is set by the transmission efficiency of the instrument, thruput and detector responsivity. The zero level is that spectral flux which gives no output signal. Our polarizing interferometer measures the difference in intensity between the two polarization states after the entrance polarizer. One polarization coming from the input radiation transmitted by the wire grid and the other coming from the reference beam reflected off the back of the grid. The entrance polarizer is tilted so that the reference radiation comes from the black cavity surrounding the interferometer. Thus, the zero level is the spectral flux from a blackbody at the temperature of the liquid helium which fills the cavity.

A blackbody immersed in the helium bath is used to check the zero level. This blackbody immersed in the helium bath is used to check the zero level. This blackbody is shown in Figs. II.1 and II.2.

The spectrometer can be fed with radiation from this blackbody by rotating the mirror used to direct the radiation into the spectrometer. In this condition, the box containing the spectrometer and detector is a radiation sealed isothermal chamber. No signal has been detected by the bolometer in this configuration. The bolometer itself runs a few tenths of a degree warmer than the bath but the polarizing chopper does not modulate the unpolarized radiation emitted by it.

The flux responsivity can be determined by measuring the spectrum from a blackbody at a known temperature. The room serves as a blackbody at $\approx$ 300K for laboratory calibrations. Figure II.7(a) shows the measured spectrum of the room. This spectrum together with the zero level determination was used to calculate the flux responsivity shown in Fig. II.7(b). This is also done in chapter III using inflight spectra. The inflight calibration spectra are obtained by looking at the small moveable blackbody shown in Figs. II.1 and II.2 and at the large calibration body shown in Fig. II.3. The inflight calibration is necessary since both the electrical responsivity and the detector absorptivity depend when the bath temperature and the radiation loading. Laboratory spectra were also taken of a cold blackbody inserted down the long copper cone. This measurement established that the spectrophotometer response is linear over three decades of flux intensity.

The spectral shape of the flux responisity shown in Fig. II-7(b) is determined by several different components. The low frequency roll-off comes from the decreasing bolometer absorptivity and waveguide cutoff at the small 3 mm aperture in the copper cone. The Fluorogold$^{T.M.}$

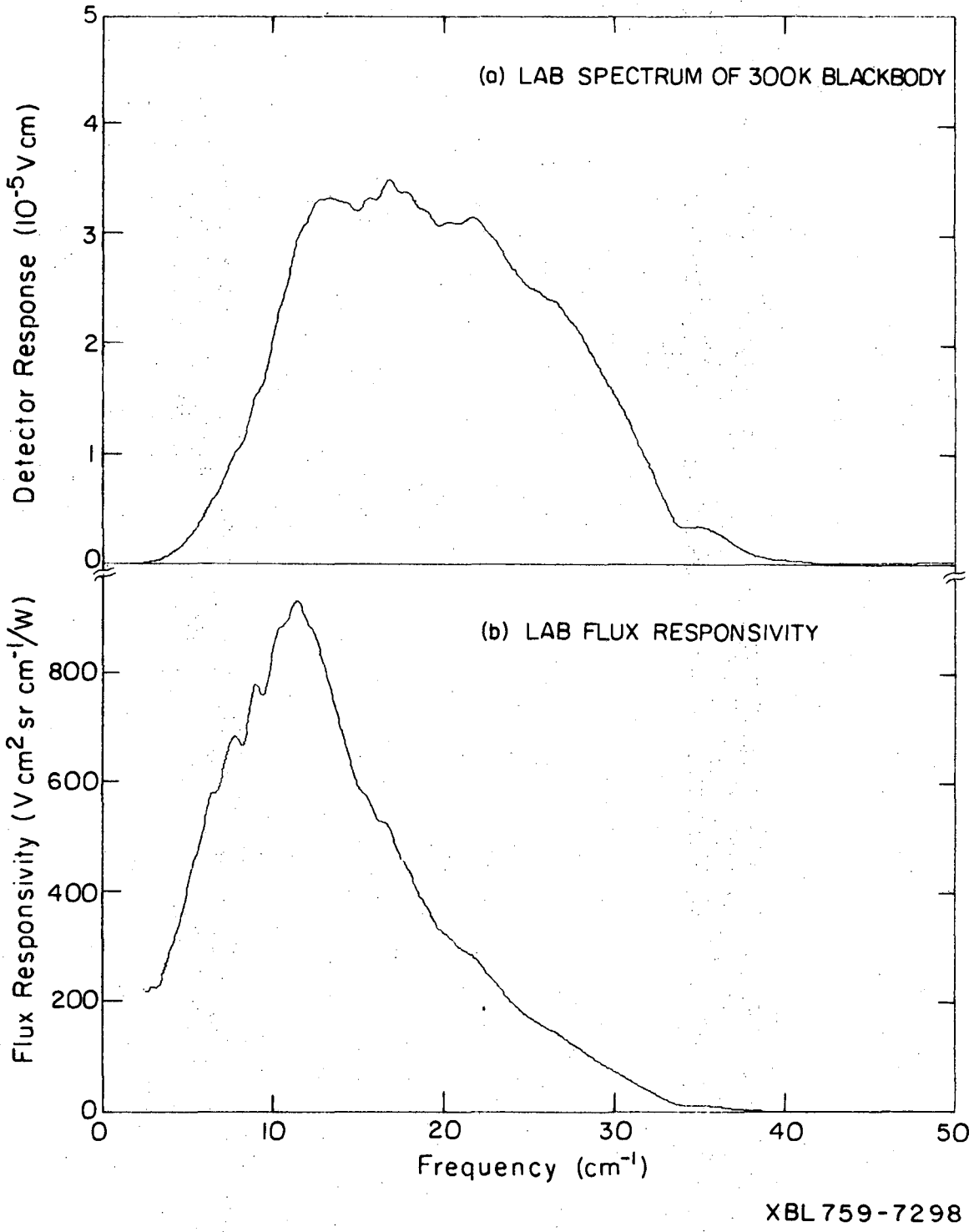

Fig. II.7. Laboratory calibration spectra.

scatter filter establishes the high frequency roll-off with the falling beamsplitter efficiency and decreasing radiation coupling efficiency between the germanium condensing cone and bolometer also contributing to this roll-off.

The measured flux responsivity and bolometer electrical responsivity can be used to compute the optical transmission efficiency for the nominal thruput of 0.25 $cm^2 sr$. The formula used is

$$\text{Efficiency} = \frac{\pi}{\sqrt{2}} \quad \frac{\text{Flux Responsivity}}{\text{Electrical Responsivity} \times \text{Thruput}} \quad . \qquad \text{(II.29)}$$

The numerical factor comes from converting a square-wave chopped signal to an r.m.s. voltage output from the lock-in amplifier. At 12 cm^{-1} this gives an efficiency of 1.2%. Table II.2 gives an accounting of this efficiency from the different components. Table II.2 also lists various other performance characteristics of the spectrophotometer.

Table II.2. Spectrophotometer performance parameters.

Frequency range	3-40 cm^{-1}
Beamwidth at half-power points	$\approx 6°$
Thruput ($A\Omega$)	0.23 $cm^2 sr$
Detector sensitivity (NEP_e)	6×10^{-14} $W/\sqrt{Hz}$
Detector responsivity	7×10^{5} V/W
Broadband Rayleigh Jean's temperature sensitivity (at zero path)	0.02 $K/\sqrt{Hz}$
Operating temperature	$\approx$ 1.6K
Chopping frequency	17.1 Hz
Net efficiency at 12 cm^{-1}	0.012
Approximate breakdown:	
antenna	.95
lenses	$(.93)^2$
input polarizer	.5
vignetting	.5
low pass filter	.8
subtotal	.16
chopping efficiency	.8
detector system efficiency	.09
Net	.012

III. FIGHT DATA

A. Flight Summary

The spectrophotometer described in chapter II has been flown twice. The first flight was on October 26, 1973. During that flight there was a failure in the system which moves the interferometer mirror and no spectral data were obtained. The flight nevertheless provided useful tests of many parts of the system, and integrated spectral intensity measurements were obtained. The results of the flight are described by Mather (1974) and by Mather, Richards, and Woody (1974). The second flight on July 24, 1975 was a complete success. This chapter describes the data obtained during the second flight and the data reduction.

The spectrophotometer was carried aloft by a 3.3×10^5 m^3 balloon on the evening of July 24, 1974 from Palestine, Texas. The launch was uneventful, except for a telemetry antenna failure which was quickly diagnosed and corrected by Henry Primbsch a few minutes before leftoff. A float altitude of 39 km was reached three hours after launch. The apparatus remained at a float altitude of $38.5\pm.5$ km for four hours before termination over Balmorhea, Texas. The last hour of the flight was monitored from the down range station at Midland, Texas and suffers from an excessive number of "telemetry dropouts" (loss of telemetry signal). The apparatus sustained only minor damage upon landing and was recovered in good condition.

The limited flight time allowed only a very simple flight scenario. The basic parameters under our control were the zenith angle, the temperature profile of the antenna, the presence or absence of the protective window over the horn and the interferogram scan length. These parameters were varied to give seven different configurations plus calibrations using both the large and small calibrators. The various configurations and calibrations are referred to as "Cases" and are listed in Table III.1 along with the time spent in each configuration. The best conditions for obtaining a spectrum of the cosmic background radiation were during Cases V and VI when there was no window in the beam and the antenna was cold. These two cases were combined by averaging the 64 points in Case V with the first 64 points of Case VI. This combination is designated as Case V + VI. The zenith angle of 24° was determined during the first flight to be the angle at which the integrated flux from the balloon, atmosphere, and earth is a minimum.

A chronological summary of the flight is given in Fig. III.1. The major events during the flight are identified in the time chart shown in Fig. III.1(i). Figure III.1(ii) shows the atmospheric pressure at the gondola after float altitude was reached. The temperature at various points on the apparatus is plotted in Fig. III.(iii). The positions range from the helium bath (a) up through the cone-to-horn junction (e) to the gondola frame (h). The helium vapor pressure for the 1.65K bath temperature is 9.3 mbar. The ≈ 6 mbar pressure drop between the bath and the outside atmosphere is a result of the gas flow impedence in the vent paths.

Table III.1 List of observational configurations

Case designation	Zenith angle	Temperature of antenna	Window position	Interferogram length	Duration	Number of scans
I	24°	cold	on	short	75 min	25
II	24°	warm	on	short	24 min	8
III small calibrator	24°	cold	on	short	3 min	1
IV	45°	cold	on	short	15 min	5
V	24°	cold	off	short	69 min	23
VI	24°	cold	off	long	24 min	2
VII large calibrator	-15°	cold	off	short	2 min	< 1

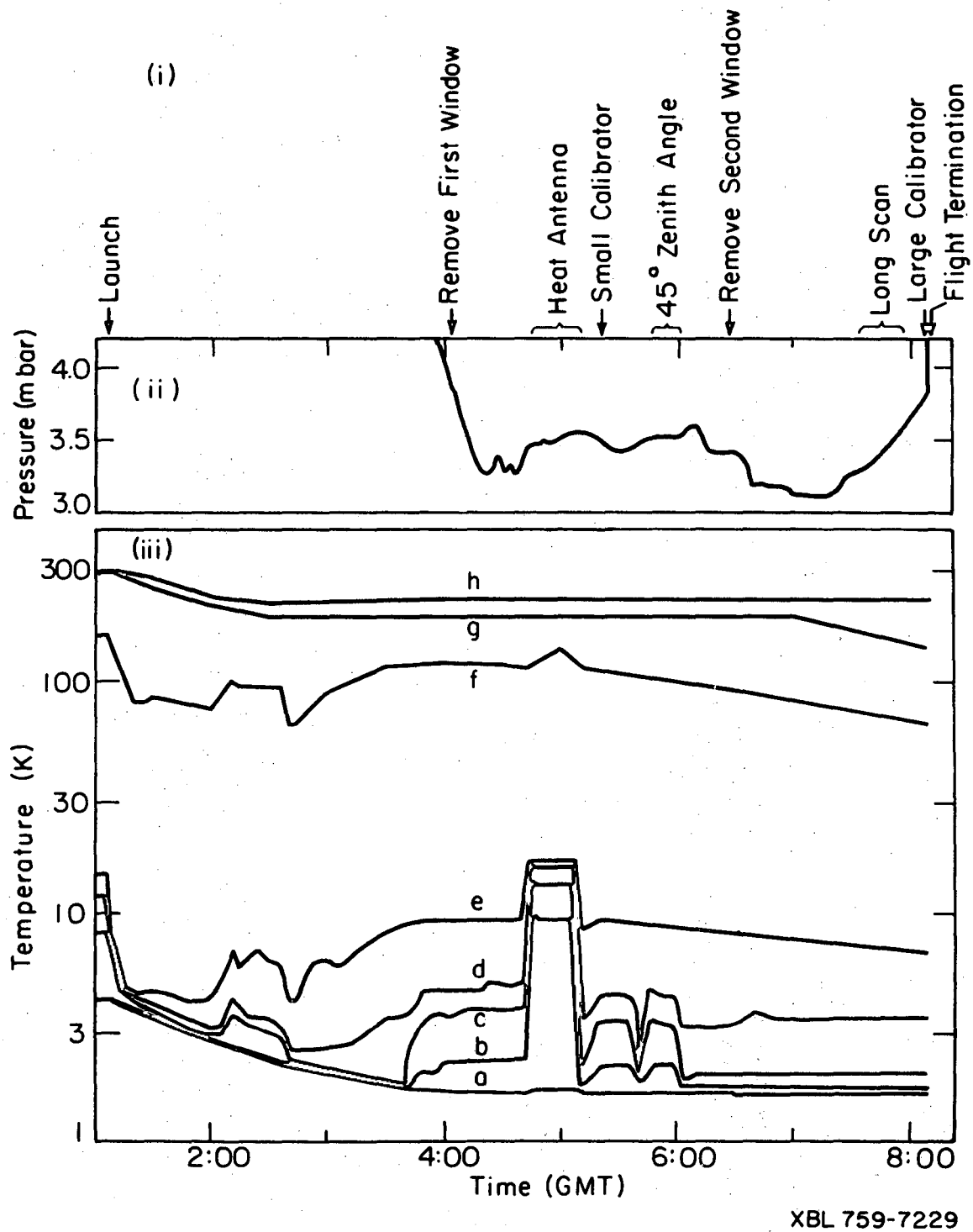

Fig. III.1. Flight summary: (i) flight scenario; (ii) atmospheric pressure; (iii) temperature profile of the apparatus, (a) helium bath, (b) bottom of cone, (c) middle of cone, (d) top of cone, (e) bottom of horn, (f) middle of horn, (g) top of horn, (h) gontola frame.

Figure III.2 is a map of the shy observed by the freely rotating apparatus. The thin line is the beam center with the beam profile covering $\approx 5°$ on each side. The map was constructed using the readings from two magnetometers for the azimuthal angle and a pendelum for the zenith angle. The resulting calculation of equatorial coordinator should be accurate to $\pm 5°$.

B. Signal Averaging

Many separate interferograms were obtained in each Case or configuration which were averaged together to produce a single interferogram. The polarizing interferometer was operated in an automatic step and integrate mode in which each individual interferogram contained either 64 or 256 separate data points. Each point in the interferogram took 2.56 sec; of which .16 sec was spent moving the mirror (increasing the optical path by 0.0082 cm), 0.4 sec waiting for transients to damp out and 2.0 sec integrating the detector signal. After a preprogrammed number of steps the interferometer mirror was returned to its initial position and another scan started the total time required for a 64 point interferogram, including returning the mirror, was 3 minutes and that for a 256 point interferogram 12 minutes.

The first step in the data reduction was to replay the audio tape recordings of the flight through the ground station. The signal and reference channels were fed into a PAR$^{T.M.}$ 124A lock-in amplifier whose output was connected to our PDP-11 computer. The computer performed a 2 sec time average of the signal at each interferogram

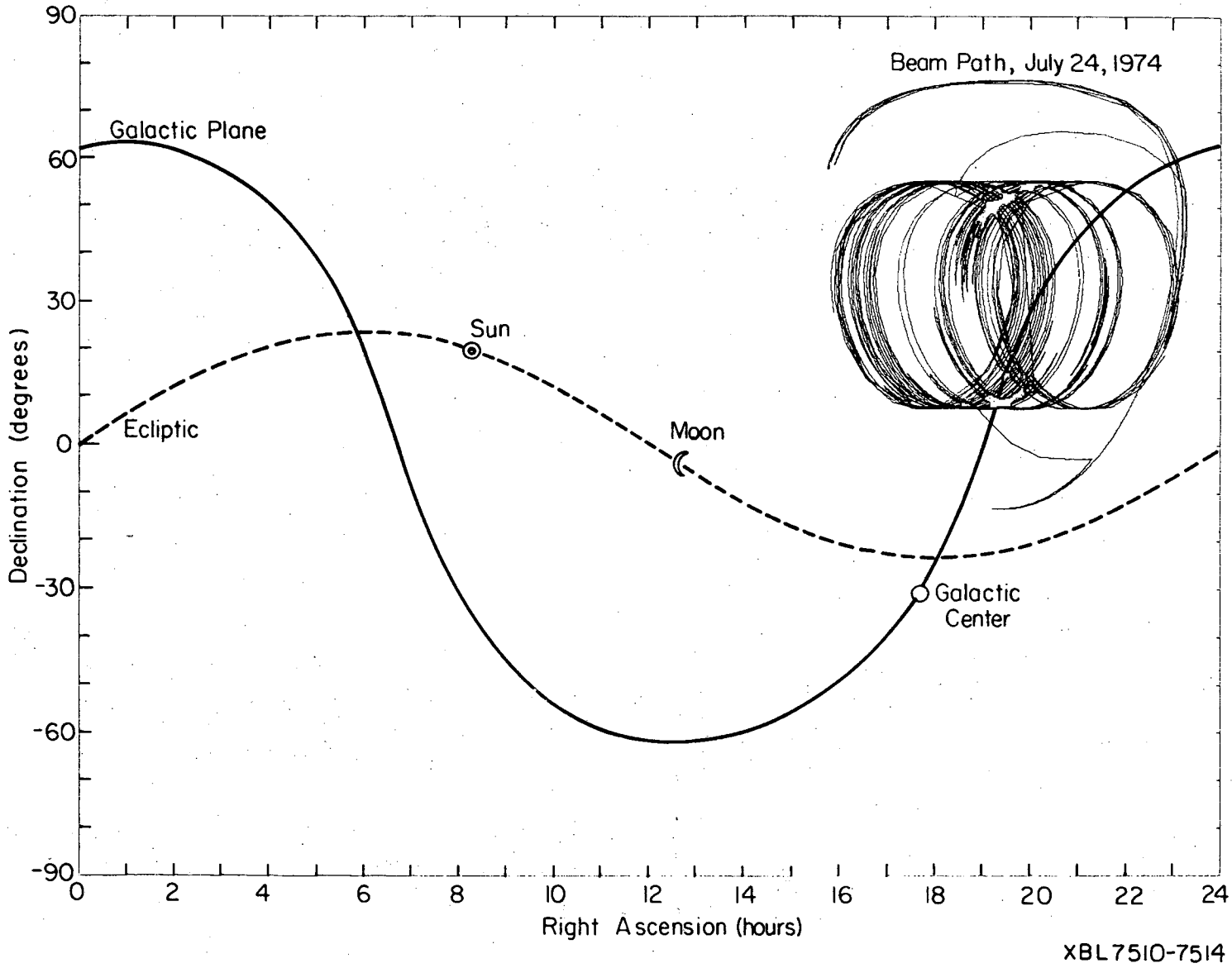

Fig. III.2. Equatorial map of sky coverage during flight on July 24, 1974.

point and produced a digital tape of each interferogram scan. Electrical zero and gain checks were made every few scans. These offsets were subtracted and gains divided out to give voltages referred to the detector.

The next step in the data reduction was to remove "glitches" from the data. Potentially bad points were identified by a program which averaged together all the scans from a given Case and computed the deviations of individual points from the average. Points deviating by more than 3σ were examined. Telemetry fade-out (particularly from the downrange Midland, Texas receiver) and magnetic tape dropout were a major source of glitches. These were clearly recognizeable since all telemetry channels would vary widely. Points associated with such "glitches" were replaced with ones from a better magnetic tape copy or not included in subsequent analysis if no better copy existed. A more subtle cause was mechanical or electrical transients in the gondola. These were usually seen only in the detector signal but were correlated with issuing commands to the various stepper motors on board. Points associated with these transients were also rejected. Out of the total of 4,480 data points, 59 were rejected, 28 of which were associated with known glitches or transients. The remaining 31 points appeared to be randomly distributed throughout the data. The standard deviation for the points not rejected was 22×10^{-9} referred to the detector. This is close to the expected value of 20×10^{-9} V based on the detector noise of 40×10^{-9} V/$\sqrt{\text{Hz}}$ measured in the laboratory and a 2 sec integration time.

It is interesting to speculate as to whether the points rejected on statistical grounds were submillimeter sources transiting the field of view of the spectrophotometer. The gondola rotation rate was on the order of 1 degree/sec so that a point in the sky spent on the order of 6 sec crossing the 6° wide beam; just long enough to be seen in two or three interferogram points. At zero path, the spectrophotometer can be used as a broadband radiometer with a temperature responsivity to a Rayleigh Jeans source of 2×10^{-6} V/K. A 10^{-7}V($\approx4\sigma$) glitch would thus correspond to a .05K source filling the beam. The problem is that the rejected points aren't at zero path but at a finite distance from zero path where the spectral response function is actually a positive and negative going cosine function. The responsivity to a broadband source is greatly dimenished and could be zero. This increases the temperature of the source required to produce a 4σ glitch. Such a source would hopefully show up in the 2nd harmonic detector signal which retains a broadband spectral response but with a factor of ten less sensitivity. A cursory check of this signal showed no clear indications of an increase in the intergrated flux at the positions of the glitches.

The individual scans in each flight configuration were averaged together to obtain a single interferogram. This produced an interferogram for each case with the noise decreased by the square root of the number of scans taken. Cases V and VI were averaged together to obtain a single interfergram of 256 points but with a factor of ≈4 less noise in the first 64 points than in the remaining 192 points. This

interferogram is shown in Fig. III.3 with the data points connected for ease of viewing. The noise is approximately twice the line thickness from -0.35 to 0.18 cm and ten times the line thickness above 0.18 cm.

Apodization is a standard technique used to eliminate "podes" and reduce the resolution (and thus to decrease the noise) in the calculated spectrum. This involves multiplying the interferogram by a weighting function which gives more weight to the points closest to zero path. The convolution theorem tells us that this is equivalent to convolving the spectrum obtained without apodization with a resolution function which is the Fourier transform of the apodizing function. Thus the decrease in noise is obtained by sacrificing resolution. The mathematical details of apodization are discussed by Bell (1972, p.51) and Mather (1974, p.157). Mather has derived an expression for the spectral noise from an apodized interferogram

$$\langle N^2(\nu) \rangle = n^2 \sum_j |A(j\Delta x)|^2 \frac{(\Delta x)^2}{t_j} \qquad \text{(III.1)}$$

where n is the detector noise, $A(j\Delta)$ the apodizing function and t_j the observing time for the jth point. We have used artificially generated gaussian noise interferograms to verify that the spectral noise predicted by Eq. (III.1) is correct. Usually, quadratic apodization of the form

$$A(x) = [1 - (x/x_{max})^2]^2 \qquad \text{(III.2)}$$

was used in our data analysis.

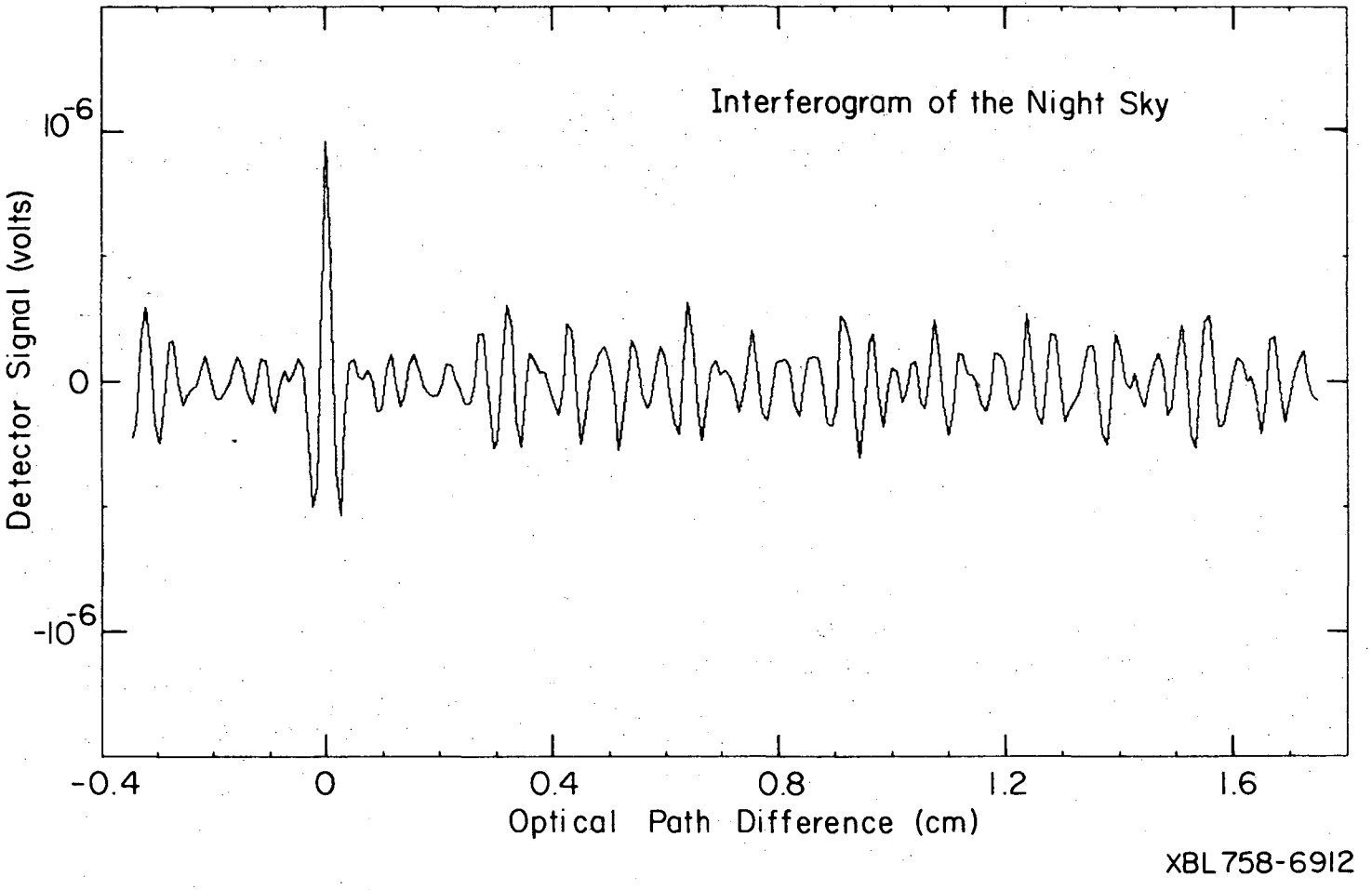

Fig. III.3. Interferogram of the night sky.

The magnitude of the spectral noise can be estimated from the high frequency part of the spectrum where there is no optical signal. The spectral noise corresponds to a detector noise of 4.4×10^{-8} V/$\sqrt{\text{Hz}}$ (or 2.2×10^{-8}V per point) when the spectrum is computed from a single interogram scan. But the spectral noise corresponds to a value of 7.8×10^{-8} V/$\sqrt{\text{Hz}}$ for n in Eq. (III.1) (or 3.8×10^{-8} V on any data point in a single scan) when the spectrum is computed from the averaged interferogram for Case V and VI. The error in this number is ±15% since only 43 independent spectral points were used, but is still nearly twice as large as the varition of any particular interferogram point measured in successive scans. That is, the spectral noise does not scale as the square root of the number of scans. This indicates that the interferograms contain reproducible but apparently random errors. That is, the error in the jth interferogram point is the same from one scan to the next but is uncorrelated with the error in the j+1th point. It takes only an error of 5×10^{-9}V (one fifth as large at the detector noise) to explain the behavior we see. Such errors could arise from mechanical errors in the interferometer, non-linearity in the detector, or most likely errors in the telemetry and interferogram recording system. The magnitude of this error corresponds to ≈1% of a telemetry bit in the preamp channel at the 10^5 gain that we were using and is at the limit of the nonlinearity specification of the analog-to-digital and digital-to-analog converters in the telemetry system.

C. Interferometer Errors

Michelson type Fourier transform spectrometers are subject to several different types of errors. These errors distort the measured interferogram so that the spectrum computed using Eq. (II.2) (or its discrete step version) differs slightly from the true spectrum. Although the deviations are small, they can hinder attempts to fit a model of the spectrum to the measured data. In particular, the merit of a model used to simulate the observed spectrum is best judged by looking at the residuals from the fit and seeing how close they are to the expected random noise. To do this correctly requires that even the errors in the interferometer be included in the model, hopefully as fixed parameters. The errors determined in this section will be included in the model calculations used in Chapter IV to analyze our data.

Some of the errors are best determined from the imaginary (or sine) transform of the interferogram. The complex version of Eq. (II.2) is

$$G(\nu) = \int_{-\infty}^{\infty} (I(x) - \text{const}\times I(o))\, e^{i2\pi\nu x}\, dx \,. \qquad \text{(III.3)}$$

The imaginary part of $G(\nu)$ is the result of interferogram noise or errors since we now that the true spectrum is strictly real.

The most prevalent error is the deviation of the baseline (the constant×I(o) appearing in Eqs. (II.2) and (III.3)) from the ideal value. In the ideal polarizing interfermeter, the baseline is zero.

Section C of chapter II shows that errors in the baseline are proportional to the integrated signal strength and are a result of alignment errors and polarizer imperfections. A baseline shift causes errors in the zero frequency spectral point by contributing a d.c. term to the integral in Eq. (III.3). It also leads to an error in the zero level for the computed spectrum through the shift in the value used for the zero path point I(o).

It is common practice to use the average value of the last several interogram points for the baseline. This works well in the case where all the spectral features are well resolved and the noise is small. In the case of unresolved features, the interferogram is still oscillating and this average is not well determined. A better method can be use if there is no spectral energy within one resolution width of zero frequency. This is the case with our spectrophotometer since there is a waveguide cutoff in the long cone at $\approx 3\ cm^{-1}$. The baseline can be set by requiring that G(o)=0. This gives a baseline that is correct to within $\pm n/\sqrt{M}$, where n is the noise on an individual interferogram point and M is the total number of points.

Another common error is that the zero path point is not the same for all spectral frequencies. This can happen if there is an uncompensated dispersive dielectric in one of the interferometer beams, the interferometer is misaligned, or in the case of a discretely sampled interferogram, when there is no sample exactly at zero path. These errors cause the measured interferogram to be asymmetric and introduce an imaginary component to the computed spectrum $G(\nu)$. (The imaginary part of $G(\nu)$

is identically zero if I(x) is symmetric). The true spectrum can be recovered by multiplying $G(\nu)$ by the correct phase function $e^{i\phi(\nu)}$. The true spectrum is completely real so that $\phi(\nu)$ can be determined by requiring that the resulting spectrum $G(\nu)\times e^{i\phi(\nu)}$ be real, ie. just use the amplitude of $G(\nu)$. This requires that the interferogram be sampled nearly symmetrically on both sides of zero path and that there be no noise or ghosts (see below) in the data. There are several phase correction techniques which work to varying degrees for asymmetrically sampled interferograms and in the presence of noise. These are discussed by Bell (1972) and Mather (1974).

The situation with our interferometer is much simpler. The phase errors from mirror misalignment and missampling of the zero path point are a simple function of frequency. Missampling of zero path by a distance ε[cm] contributes a linear term (Bell, 1972)

$$\theta(\nu) = 2\pi\varepsilon\nu. \qquad \text{(III.4)}$$

Misalignment by an angle α[radians] contributes a quadratic term (Goorvitch, 1975)

$$\phi(\nu) = 2\pi^2 R^2 \alpha^2 \nu^2 \qquad \text{(III.5)}$$

where R is the radius of the interferometer optics (2.5 cm for our interferometer). Minimization of the rms value of the imaginary spectrum (sine transform) can be used as a criterion for proper phase correction even in the presence of noise. The two constants in the quadratic phase function can be accurately determined using this criterion.

There is a short algorithm for determining the linear phase error alone based on the criterion that the average of the imaginary spectrum be zero. Using the small argument expansion of the exponential, this criterion becomes

$$\int_o^\infty [2\pi\varepsilon\nu \mathrm{Re}\ G(\nu) + \mathrm{Im}\ G(\nu)]d\nu = 0 \qquad \text{(III.6)}$$

giving

$$\varepsilon = \frac{1}{2\pi} \frac{\int_o^\infty \mathrm{Im}\ G(\nu)\ d\nu}{\int_o^\infty \nu \mathrm{Re}\ G(\nu)\ d\nu}$$

This procedure can be applied iteratively to obtain ε. Fast monatonic convergence to the correct value will occur if ε is less than one half of the step size for a discretely sampled interferogram.

A more subtle error which can occur is a periodic modulation in the size of the step used to sample the interferogram. Interferometers whose mirror position is controlled by a screw are prone to this kind of error. Screws which are not straight or have a nonuniform pitch around their circumference impart a modulation to the step size which has a period of one resolution. This introduces sidebands or ghosts on each side of a spectral feature in the computed spectrum which are shifted in frequency by $\pm$ 1/2 $\Delta\ell$, where $\Delta\ell$ is the pitch length. These sidebands are similar to the Rowland ghosts found in ruled gratings. The magnitude of the sidebands for a step modulation of amplitude δ[cm]

is

$$|g(\nu_o \pm 1/2\ \Delta\ell)| = \pi\nu_o\delta\ |G(\nu_o)| \qquad \text{(III.7)}$$

Similar sidebands are introduced if the transmission efficiency of the interferometer is modulated by the rotation of the screw. In this case, the fractional magnitude of the sidebands is just one half of the fractional modulation of the efficiency and is independent of frequency.

The ghosts can have any phase in the complex spectrum depending upon the phase of the modulations relative to zero path. They can't be removed from the real part of the spectrum without additional information about the true spectrum. However, in the absence of large phase errors or noise they are easily detected in the imaginary spectrum. The real spectrum is a close approximation to the true spectrum and can be used to calculate a model for the imaginary ghosts. This model can be used to determine the magnitude of the imaginary ghosts based on the same criterion of minimizing the rms value of the imaginary spectrum. This doesn't provide any information about the real ghosts, but does give an estimate of how large they might be.

The interferometer errors in our data were calculated by a program called IMFIT. The program first determined the baseline from the requirement that G(0) = 0. The complex spectrum was then calculated using a short two sided interferogram and a minimization program was used to determine the phase errors and ghosts. This involved four free

parameters for the linear phase error, the quadratic phase error, the imaginary ghosts due to step modulation and the imaginary ghosts due to transmission efficiency modulation. The results for the flight data are listed in Table III.2. The errors are within expected tolerances. The phase errors imply less than a 1% correction to the real spectrum in all Cases except Case IV where the correction exceeds 1% above 25 cm^{-1}. The rms values of the imaginary spectra after correction are slightly larger than that expected from the measured interferogram noise (detector noise plus reproducible random errors); except for Case III which was taken at lower gain and is limited by bit noise. This indicates that our model of the interferometer errors is incomplete. The uncorrected errors are probably random versions of the ones already discussed.

The corrections shown in Table III.2 are not made to the raw interferogram, but are only applied to the computed spectrum or to a model spectrum that is to mimic our data. The results of applying these corrections to Case V + VI are shown in Fig. III.4. This is a low resolution spectrum computed from a quadratically apodized interferogram consisting of only 22 points on each side of zero path. It shows the sine spectrum before and after correction and the cosine spectrum.

Table III.2. Interferometer Corrections.

Case	Zero Path Signal I(o)[V]	Baseline [% of I(0)]	Linear Phase $\phi=2\pi\nu\varepsilon$ ε[cm]	Quadratic Phase $\phi=2\pi^2R^2\nu^2\alpha^2$ α[radians]	Step Modulation Ghosts = $\delta\nu$ δ[cm]	Transmission Modulation Ghosts = 1/2R R[%]	rms of Sine Spectrum after Corrections [V/cm^{-1}]	Expected Detector Noise [V/cm^{-1}]
I	1.27×10^{-6}	5.4	4.5×10^{-5}	9.0×10^{-4}	-3.6×10^{-4}	0.38	3.8×10^{-10}	2.5×10^{-10}
II	1.34×10^{-6}	4.6	-3.8×10^{-5}	5.8×10^{-4}	-4.0×10^{-4}	1.9	5.4×10^{-10}	3.3×10^{-10}
III	6.82×10^{-5}	3.6	-1.8×10^{-3}	7.8×10^{-4}	-5.7×10^{-4}	5.6	4.0×10^{-8}	7.9×10^{-10}
IV	1.54×10^{-6}	5.3	1.4×10^{-3}	1.1×10^{-3}	-3.3×10^{-4}	1.1	4.1×10^{-10}	3.9×10^{-10}
V&VI	1.05×10^{-6}	4.2	4.5×10^{-6}	5.8×10^{-4}	-5.0×10^{-4}	0.70	3.0×10^{-10}	2.5×10^{-10}

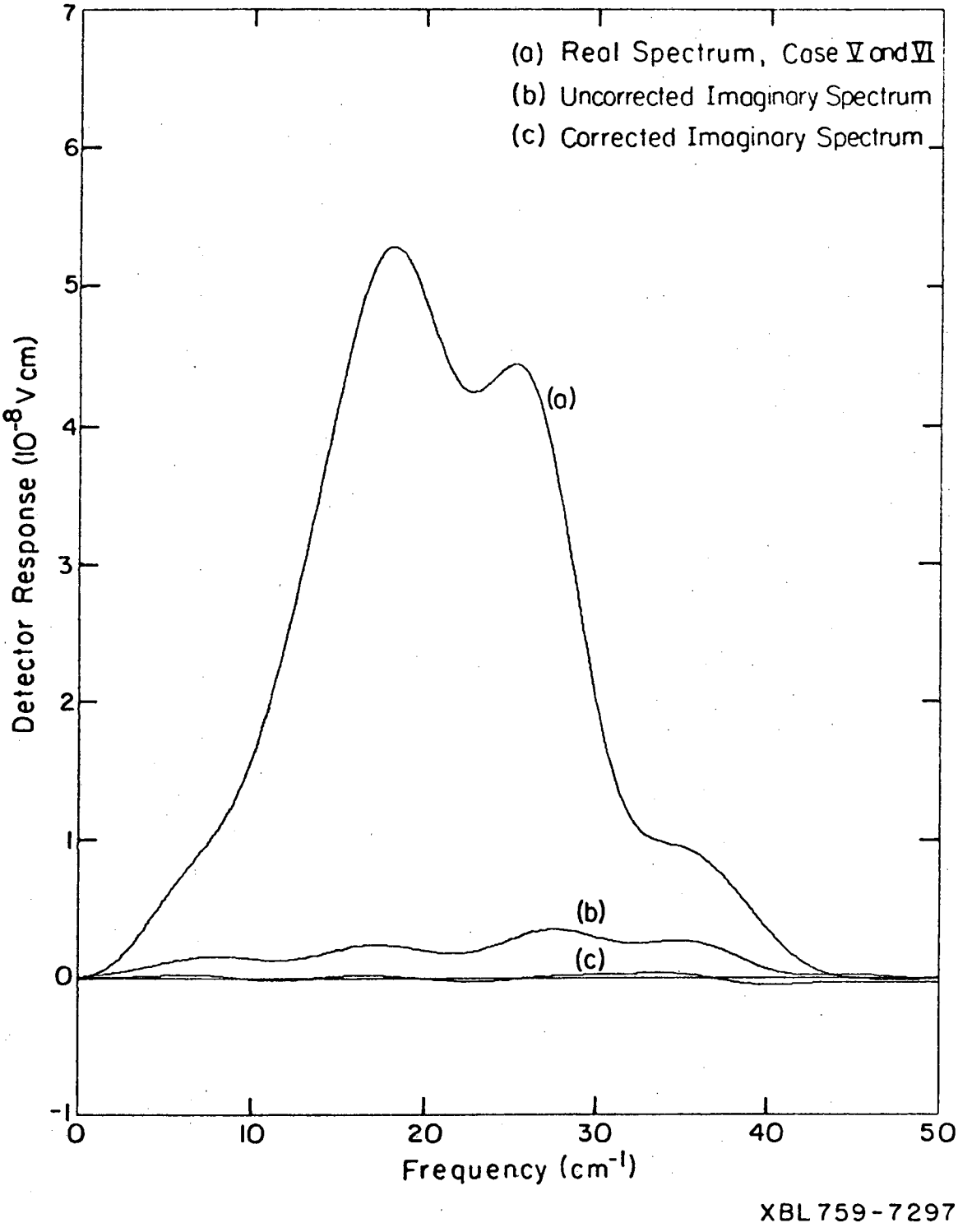

Fig. III.4. Case V + VI before and after applying interferometer corrections.

D. Calibration

The primary calibration of the spectrophotometer is the spectrum of the small calibration body obtained in Case III. This calibrator is a conical cavity with a 17° half-angle whose walls are coated with Eccosorb$^{T.M.}$ epoxy to provide a high absorptivity surface. The entrance aperture is 2.54 cm in diameter. It was expected to fill ≈15% of the beam according to rough calculations. The purpose of the large calibration body attached to the gondola frame was to measure what fraction of the beam was actually filled by the small calibrator. Unfortunately, the flight was terminated in the middle of the first interferogram scan of the large calibrator (Case VII) and its spectrum was not measured.

Other means of determining the relative size of the small calibrator had to be found. This is when the 2nd harmonic signal discussed in section of chapter II proved of great value. The signal at twice the fundamental chopping frequency is proportional to the integrated signal strength and is not modulated by the interferometer scan. Using this signal, the small calibrator was measured to fill 17% of the beam.

It was now a simple matter to calculate the spectral responsivity of the instrument from the Case III spectrum using the calibrator's measured temperature of 195K. The resulting spectral responsivity is plotted in Fig. III.5. Corrections for the bath temperature of 1.65K and the night sky filling the remaining 83% of the beam were used in calculating this spectral responsivity. Dividing by this spectral responsivity and adding the emission from a 1.65K blackbody converts our

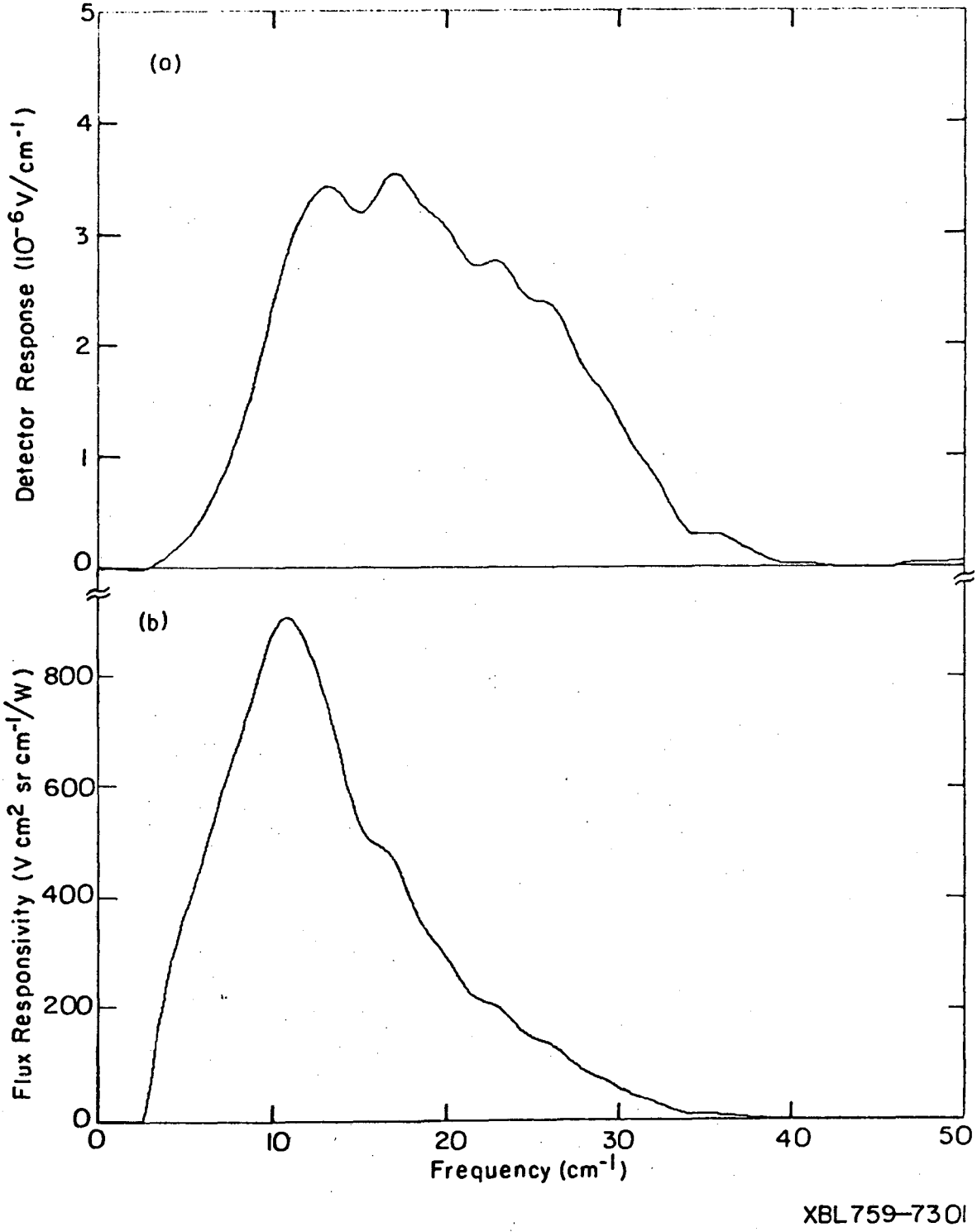

Fig. III.5. Inflight calibration spectra; (a) observed detector response to small calibrator, (b) computed flux responsivity of the spectrophotometer.

raw spectra to units of spectral flux.

The curve in Fig. III.5 differs from the laboratory calibration in Fig. II.7 by less than 10% over the frequency range from 5 to 30 cm^{-1}. The laboratory calibrations used the room as a 300K blackbody. This close agreement indicates that the small calibrator is indeed a blackbody. The inflight calibration was used for our data analysis since it was obtained under the same conditions as the rest of our flight data.

IV. DATA ANALYSIS

The procedure used to recover the CBR spectrum from the observed night sky emission spectra is discussed in this chapter. The observed night sky emission spectrum calculated from the averaged interferogram from Case V + VI is shown in Figs. IV.1(a) and (b). The detector response is plotted in (a) while the log of the spectral flux is plotted in (b). This spectrum contains the molecular line emission from the atmosphere in addition to the cosmic background radiation. Radiation from warm objects in the wings of the antenna pattern and emission from the antenna itself may also be present in the observed night sky emission spectrum. The techniques used to correct for these extraneous sources of signal are discussed in detail. The resulting CBR spectrum and the best fit blackbody temperature are presented along with error limits

A. Antenna Emission

The spectra from Cases I and II were used to determine the antenna emission. The antenna in Case I was cooled so that the temperature at the junction between the cone and horn was only 4.5K, while the temperature in Case II was 16K. The difference in signal between the two Cases is just the difference in antenna emission for the two temperature profiles. The spectra calculated for Cases I and II are plotted in Fig. IV.2 (a) along with the difference spectrum. This difference spectrum has been converted to a spectral flux in Fig. IV.2(b).

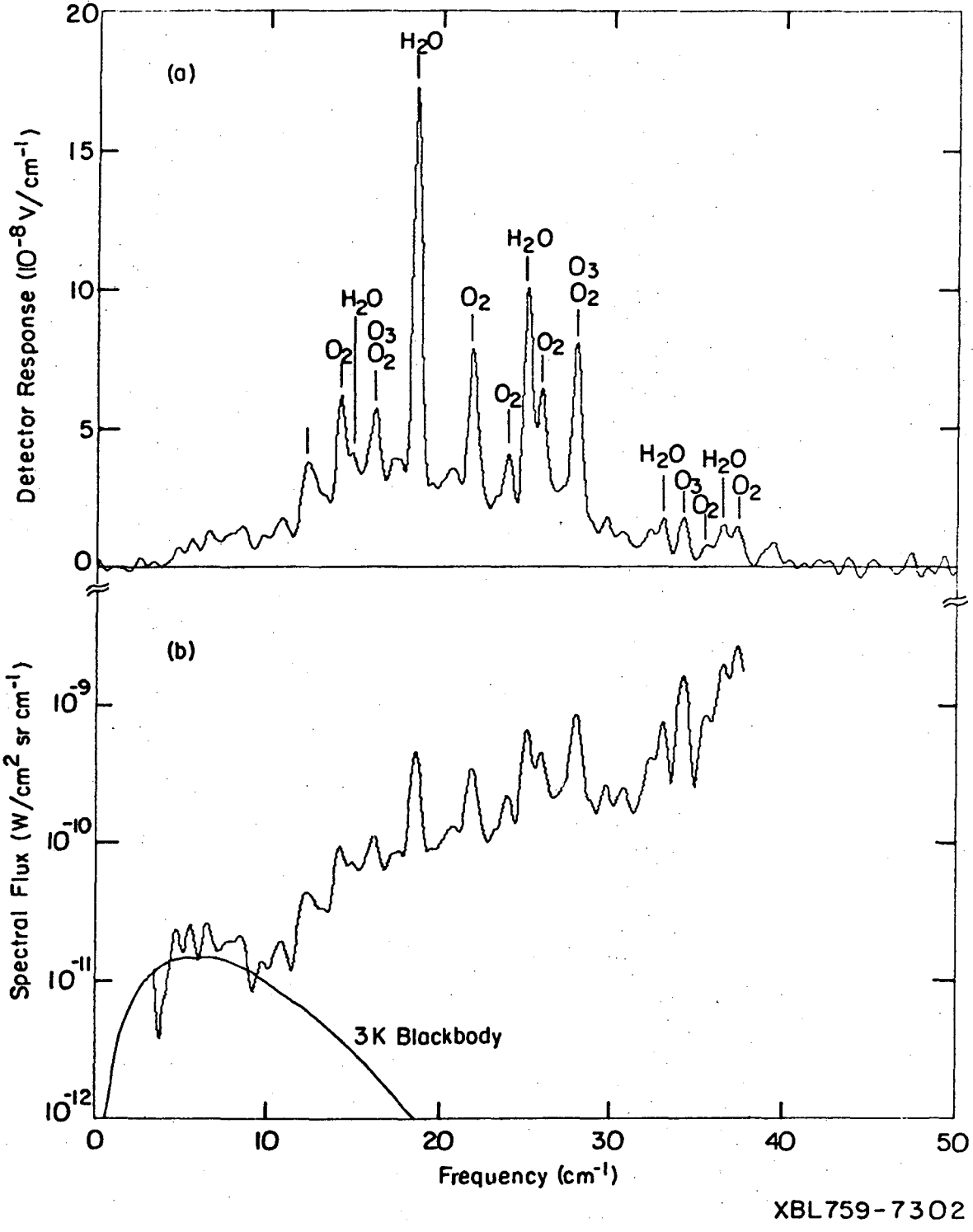

Fig. IV.1. Observed night sky emission spectrum.

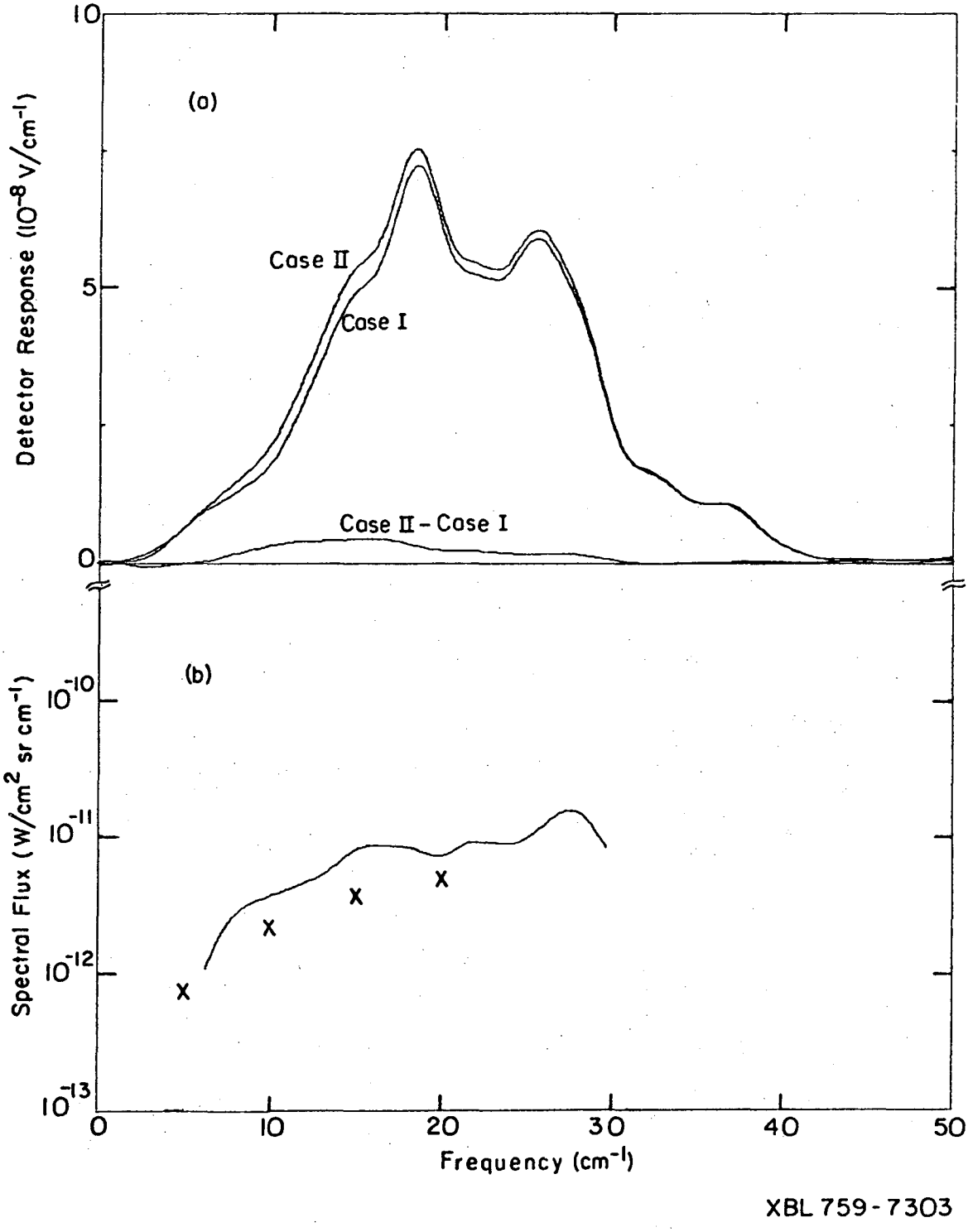

Fig. IV.2. Spectra used to calculate the antenna emission; (a) observed detector response for heated and cooled antenna, (b) measured (——) and calculated (x) increment in spectral flux from the antenna.

A model for the antenna emission was needed before the difference in spectral flux could be used to calculate the absolute antenna emission. Such a model was provided by combining the ray tracing program used in the antenna pattern calculations and the surface emissivity program (see Appendix B) used in the antenna emissivity calculations. In this combined program, a large number of rays were traced through the antenna. The flux contributed at each reflection from the antenna was calculated using the temperature at that point and the calculated emissivity for the ray's angle of incidence. The flux contributed by all the reflections was summed and normalized by the total number of rays. Typically, 10^5 rays were used. The program had to be run once for each spectral point calculated since the diffraction at the cone to horn transition is frequency dependent. This model has no free parameters once the temperature profile is given. Using the temperature profiles of Cases I and II, the difference in spectral flux was calculated at several frequencies. These points are represented by X's in Fig. IV.2(b).

The points calculated from the model are within ≈30% of the measured spectral flux. This is consistent with the discrepancies between the calculated and measured average emissivities in Table II.1. The agreement was close enough that the model could be used to produce realistic calculations of the absolute antenna emission without any free parameters or alterations. The antenna emission calculated for the temperature profile of Case V is shown in Fig. IV.3 along with a 3K blackbody spectrum. [Note that the antenna was colder in Case V than in Case I, the cone to horn junction being only 3.5K]. The antenna

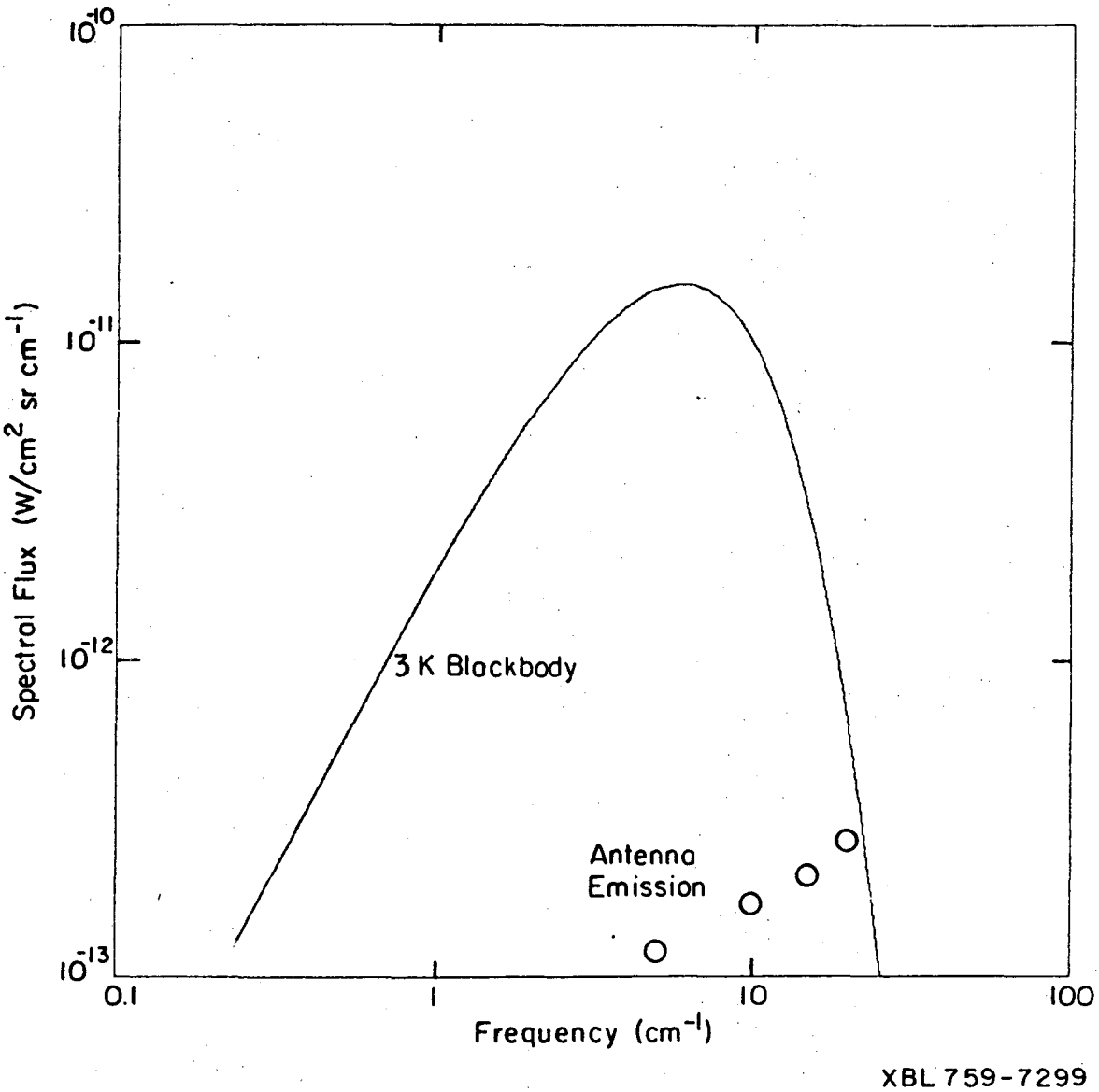

Fig. IV.3. Calculated antenna emission (0).

emission is negligble out to 20 cm^{-1}. Beyond 20 cm^{-1}, the atmospheric emission is several orders of magnitude larger than this antenna emission and the antenna contribution can be neglected.

A note of caution concerning this model calculation is in order. The calculated fluxes shown in Fig. IV.2(b) and Fig. IV.3 are dominated by different parts of the antenna. Most of the difference in flux between Case I and Case II comes from the top of the long copper cone where there is a large difference between the temperature profiles. Whereas in the calculations of the absolute flux, the horn contributes most of the radiation. Thus the inflight measurement gives only a partial check of the important part of the model. This would be particularly important if losses in the 50 μm polyethylene coating were large. The measurements discussed in chapter II indicate that these losses are small below 20 cm^{-1}, being less than the absorptivity of the copper.

The presence of the protective window over the horn also complicates the measurements. The reflectivity of the 25 μm TPX film is 4% at 10 cm^{-1}. Thus some radiation emitted by the antenna in the upward direction could have been reflected back down the antenna. This source of radiation would have increased when the temperature of the antenna was increased, thus making the measured flux difference in Fig. IV.2(b) larger than would occur without the window. This could explain the discrepancy between the observed and calculated flux differences.

In summary, there is some room for error in the measurements and model calculation which may be of importance at frequencies above 15 cm^{-1} but are insignificant in the region near the peak in the 3K blackbody spectrum. The antenna emission will be treated as negligble throughout the rest of the data analysis.

B. Atmospheric Emission Model

The dominant feature in the observed night sky emission spectrum at an altitude of 39 km is the molecular line emission from the atmospheric. This emission is due almost entirely to water, ozone and oxygen. Water and ozone emit by electric dipole transitions between rotational levels, while oxygen emits by magnetic dipole transitions between the fine structure states of different rotational levels. Water contributes about ten lines in the frequency range of interest with many of them having an optical depth much greater than unity. There is a forest of hundreds of lines from ozone, some of which have optical depths larger than unity. Oxygen has several triplets of lines with optical depths on the order of unity.

We have developed a model of the atmospheric emission which accurately fits the observed spectrum. The model includes the exponential dependence of the atmospheric pressure on altitude and its effect on the pressure broadened line widths. However the model has been simplified by assuming that the atmosphere is isothermal and that the emitting molecules are homogeneously mixed throughout the atmosphere above the balloon. The developement of the model and validity of its

assumptions are discussed below. A good reference for atmospheric emission is volume I of Goody's book Atmospheric Radiation (1964).

The atmospheric emission is somewhat easier to calculate for balloon altitudes than it is at ground level. The vertical column densities are smaller by nearly a factor of 200. The pressure broadened line widths are also 200 times narrower; the line widths being less than 5×10^{-4} cm^{-1} at a pressure of 3.4 mbar. This leaves even the tightly spaced O_3 lines separated by more than ten line widths. Thus the emission from each line can be treated separately. This is in contrast to the problem at ground level where many of the lines are heavily saturated and the overlap from neighboring lines is important.

The resolution of the spectra we obtained ($\Delta\nu > .25$ cm^{-1}) was much too low to observe the line shapes. The details of the individual lines are lost when the instrumental resolution is convolved with the actual emission spectrum. Only the total flux emitted by the individual lines need be calculated to construct a model spectrum.

The absorption (or emission) is calculated from the absorption coefficient $k(\nu)[cm^2/mol.]$. The frequency dependence of the absorption coefficient is given by the line shape and is normalized so that the line strength $S[cm^{-1}\ cm^2/mol.]$ is given by

$$S \equiv \int_0^\infty k(\nu)\, d\nu \ . \qquad \text{(IV.1)}$$

The line strength is independent of the line shape. The change in intensity of a beam traveling in the z-direction is given by

$$\frac{1}{I}\frac{dI}{dz} = -k(\nu)n \qquad \text{(IV.2)}$$

where $n[\text{mol./cm}^3]$ is the number density of absorbing molecules. The absorptivity (or emissivity) for a beam traveling a path ℓ is then given by

$$A(\nu) = 1 - e^{-\tau(\nu)} \qquad \text{(IV.3)}$$

with the dimensionless optical depth $\tau(\nu)$ defined as

$$\tau(\nu) \equiv \int_{\ell} k(\nu)n\,dz \quad . \qquad \text{(IV.4)}$$

Both $k(\nu)$ and n may be functions of z. The total emitted flux is obtained by a frequency integral of the emissivity (Eq. IV.3) times the spectral flux from a blackbody at the temperature of the atmosphere,

$$F = \int_{o}^{\infty} B(\nu,T)\, A(\nu)\, d\nu \quad . \qquad \text{(IV.5)}$$

This assumes that the path ℓ is isothermal. In our case, the blackbody spectral flux can be treated as a constant equal to its value at the line center ν_o. The integral of the emissivity over frequency is called the equivalent width $W[\text{cm}^{-1}]$,

$$W \equiv \int_{o}^{\infty} A(\nu)d\nu \quad . \qquad \text{(IV.6)}$$

Thus the total flux emitted by a single molecular line is equal to the equivalent width times the blackbody spectral flux at the line center.

It is convenient to divide the emission lines into two categories; unsaturated and saturated. The unsaturated lines are ones in which the optical depth is small enough that the linear approximation to Eq. (IV.3) is valid. Then the equivalent width can be written as a double integral

$$W = \int_o^\infty d\nu \int_\ell dz\ k(\nu)\ n(z) \qquad \text{(IV.7)}$$

$$= S \times U\ .$$

$U[\text{mol/cm}^2]$ is the column density of molecules along the path ℓ. Thus for unsaturated lines the emitted flux is simply proportional to the number of molecules and is independent of the line shape (as long as $\tau(\nu)$ remains much less than one). For saturated lines, the exponential in Eq. (IV.3) must be used and the emitted flux depends upon the line profile.

The line profiles which are important to our problem are the pressure broadened profile and the doppler broadened profile. The pressure broadened line has a Lorentzian shape with a line width parameter α which is proportional to the pressure. The absorption coefficient is

$$k(\nu) = \frac{S\alpha/\pi}{(\nu-\nu_o)^2 + \alpha^2} \qquad \text{(IV.8)}$$

(Goody, 1964, p.106). The doppler broadened line has a line width parameter which is given by

$$\alpha_D = \frac{\nu_o}{c} \left(\frac{2kT}{m}\right)^{1/2} . \qquad \text{(IV.9)}$$

In this case, the absorption coefficient is

$$k(\nu) = \frac{S}{\alpha_D \sqrt{\pi}} \, e^{-((\nu-\nu_o)/\alpha_D)^2} \qquad \text{(IV.10)}$$

(Goody, 1964, p.98). The doppler width for a H_2O line at 230K is $1.54\times10^{-6}\ \nu_o$ and the widths for O_3 and O_2 are smaller yet. This is to be compared with the typical pressure broadened width of 2×10^{-4} cm^{-1} at a 3.4×10^{-3} bar pressure. The pressure broadening is dominant for lines in the submillimeter range.

It is helpful to have an analytical expression for the equivalent width which is valid for both the saturated and unsaturated lines. Computing the integrals in Eqs. (IV.4) and (IV.6) numerically for the nearly one thousand lines would be very time consuming on even the largest of computers.

An analytical expression for the equivalent width can be derived for the case of a pressure broadened Lorentizian line shape in an isobaric and isothermal atmosphere. This is done by Goody (1964, p.126) with the result expressed in terms of Bessel's functions of the first kind with imaginary arguments,

$$W = SUe^{-SU/-2\pi\alpha}\left[I_o\left(\frac{SU}{2\pi\alpha}\right) + I_1\left(\frac{SU}{2\pi\alpha}\right)\right] . \qquad \text{(IV.11)}$$

The equivalent line width can also be derived for the case of a pressure broadened line in an atmosphere with an exponential pressure profile. The absorbing molecule is assumed to have a uniform mixing ratio throughout the atmosphere. This problem is also treated by Goody (1964, p.233). The optical depth for an atmosphere extending from a pressure P_o (at the balloon) to zero (outer space) is

$$\tau(\nu) = \frac{S}{2\pi}\frac{U}{\alpha_o}\ln\left(1 + \frac{\alpha_o^2}{(\nu-\nu_o)^2}\right) . \qquad \text{(IV.12)}$$

α_o is the line width at the pressure P_o. The equivalent width expressed in terms of the Gamma function is

$$W = 2\sqrt{\pi}\,\alpha_o\,\frac{\Gamma\left(\frac{S}{2\pi}\,\frac{U}{\alpha_o} + \frac{1}{2}\right)}{\Gamma\left(\frac{S}{2\pi}\,\frac{U}{\alpha_o}\right)} . \qquad \text{(IV.13)}$$

In the limit of $U \to 0$, W behaves like an unsaturated line despite the logarithmic singularity in Eq. (IV.12). The singularity arises from neglecting the doppler and natural widths when the pressure widths goes to zero.

The isobaric and exponential atmospheres are compared in the Matheson diagram shown in Fig. IV.4. The normalized equivalent width (W/S×U) is plotted as a function of the strength column density product

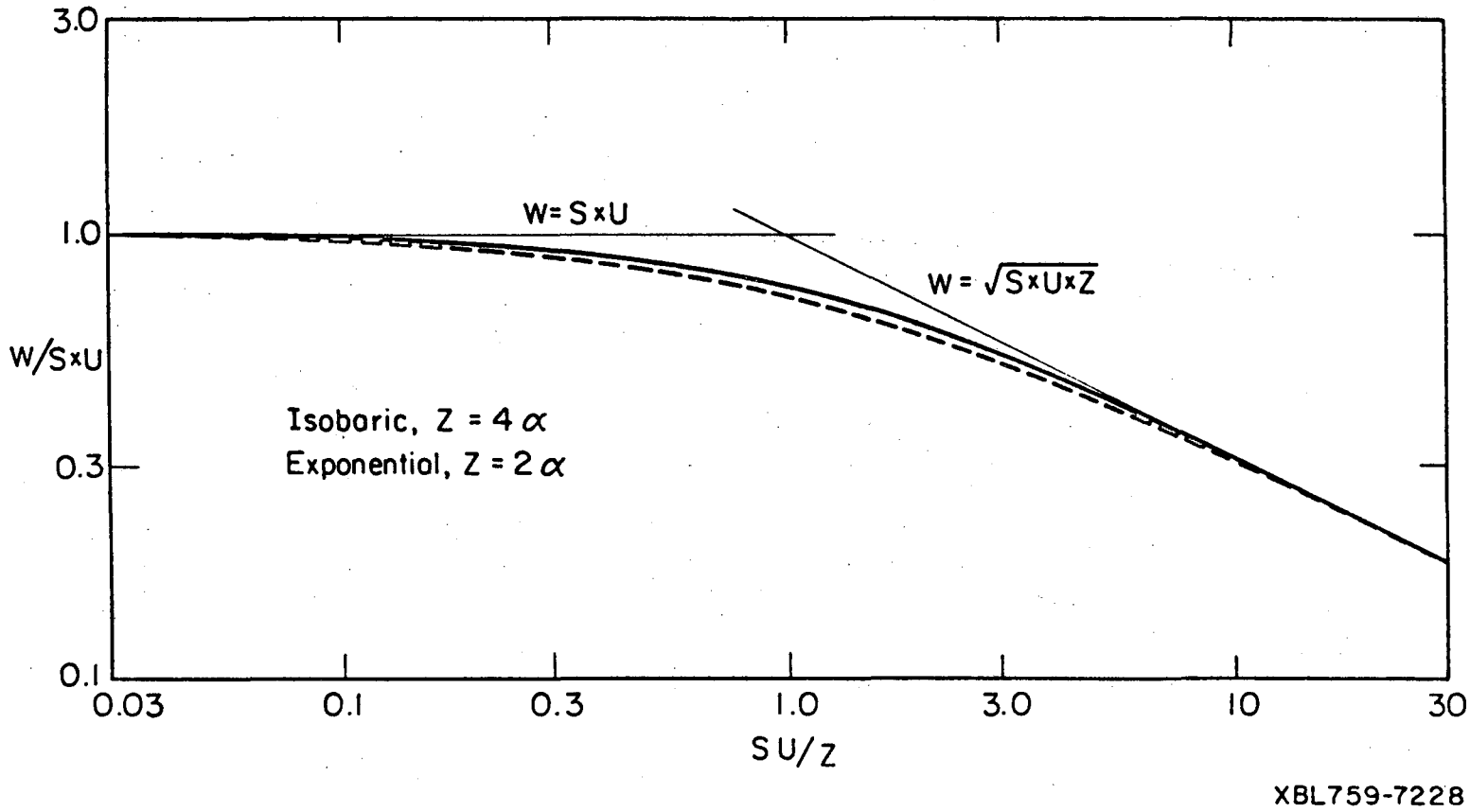

Fig. IV.4. Matheson plot for isobaric and exponential atmospheres.

(S×U) divided by a parameter (Z) related to the line width. There is very little deviation between the isobaric and exponential atmospheres. They agree exactly in the weak limit (unsaturated) and in the strong limit (saturated) if the isobaric line width α is taken to be half of α_o.

The situation with our atmospheric emission is somewhere between these two cases. The scale height of the atmosphere at an altitude of 40 km is 7.7 km. Data from the Handbook of Geophysics (1961) gives the scale heights of O_2, H_2O, and O_3 at the same altitude as 7.7 km, 3.5 km, and 4.8 km respectively. O_2 satisfies the conditions for a homogeneously mixed atmosphere very well while H_2O and O_3 have mixing ratios which decrease with altitude. In our model calculations, we will use the exponential atmosphere with a constant mixing ratio.

The temperature of the atmosphere enters into the value used for the line strength (S) as well as in the backbody spectral flux in Eq. (IV.5). The line strength scales according to

$$S \propto \frac{e^{-hE_g/kT}}{Q(T)} \times \left(1 - e^{-h\nu_o/kT}\right) . \qquad \text{(IV.14)}$$

Q(T) is the partition function; E_g is the lower state energy for the transition; and $h\nu_o$ is the resonant transition energy. The first term accounts for the Boltzman distribution of molecules among the various energy states. The second term appears when you write the absorption coefficient in terms of the Einstein coefficients. The temperature dependence of the partition function scales as the 1 or 3/2 power of

the temperature depending upon the molecule (McClatchey, et al.,1973). The line width scales as the temperature to the -1/2 power for pressure broadened lines (McClatchey, et al., 1973) in addition to scaling linearly with pressure. The atmospheric temperature increases ≈4% in one scale height at balloon altitudes (U.S. Standard Atmosphere Supplement, 1966). To make the problem tractable, the atmosphere is assumed to be isothermal in our calculations.

We can now enumerate the parameters required to calculate the flux emitted by a single molecular line. The line strength S and line width α for some standard conditions of pressure and temperature are required. The lower state energy E_g and transition frequency ν_o are needed to scale the line strength to a different temperature. [These parameters have been tabulated for the infrared and submillimeter lines of the common atmospheric molecules (including H_2O and O_3) by McClatchey, et al. (1973). The parameters for O_2 in the submillimeter region have been measured by Gebbie, Burroughs and Bird (1969) and were kindly sent to us on cards by Bill Mankin at the High Altitude Observatory in Boulder, Colorado. The parameters for O_2 in the microwave region were measured by Meeks and Lilly (1963).] The line strength and width can now be scaled to the conditions at balloon altitudes. The flux emitted is then uniquely determined by the column density U of the emitting species.

The calculated emission spectrum consists of the sum of the emitted flux from all of the lines. Each molecular transition contributes a rectangula line of height equal to the blackbody spectral flux and width

equal to the equivalent width for the given column density and located at the resonant transition frequency. This spectrum can be convolved with the instrumental resolution function for comparison with the observed spectral flux; or multiplied by the instrumental response curve and then convolved with the instrumental resolution for comparison with the detector response spectrum; or simply multiplied by the instrumental response curve and Fourier transformed for direct comparison with the raw interferogram. In the last case, any interferometer corrections should be applied before computing the Fourier transform.

The key features of the atmospheric emission calculation are summarized below. The calculations are based on four assumptions: 1) The atmosphere is isothermal, 2) the atmospheric pressure depends exponentially upon the altitude, 3) the emitting molecules have a uniform mixing ratio, and 4) the emission lines have a pressure broadened Lorentzian line shape. The published line parameters for the three molecules H_2O, O_3 and O_2 are used. The input data required are the atmospheric temperature (T), atmospheric pressure (P_o) at the gondola, and the column densities (U) for H_2O, O_3 and O_2. The temperature and pressure were measured during the flight. This leaves the column densities as the only free variables in the model.

C. Basic Fitting Procedure

Fitting a model of the night sky emission spectra to the observed data is the heart of the data analysis. The model consists of the atmospheric emission plus possible simulation of continuum contributions

such as the CBR and earthshine. The fitting procedure determines values for the model parameters which aren't set by other measurements.

Some of the considerations that arise in fitting a model to measured data can be demonstrated with a 2-dimensional problem. First, consider the case of fitting an incomplete model to the observed data. Let the measurement be represented by a point M in the xy-plane and the complete model by two vectors $\hat{a}$ and $\hat{b}$ which have fixed orientations but variable magnitudes A and B. There is a unique value for the magnitudes such that the sum of the model vectors yields the measured point. [This discussion is illustrated in Fig. IV.5]. For an incomplete model consisting of the vector $\hat{a}$ alone, a value for the magnitude A' can be found which comes closest to the measured point (least squares fit). The magnitude A' will in general not be the same as A and the incomplete model will produce an erroneous result. The two values A and A' will be the same for the special case where the vectors $\hat{a}$ and $\hat{b}$ are orthogonal. This is a corollary to the fact that a fitting procedure which minimizes the magnitude of the residual between the model and the measurement produces a residual which is orthogonal to the model vectors.

We can also illustrate the case in which there are error limits on the measurement. This time the measurement is a circle in the xy-plane. If the two model vectors are close to parallel, then there is a relatively large range of magnitudes which will fit the observation, as is demonstrated in Fig. IV.5(c). Once again the orthogonality of the vectors is important since the range of magnitudes is a minimum

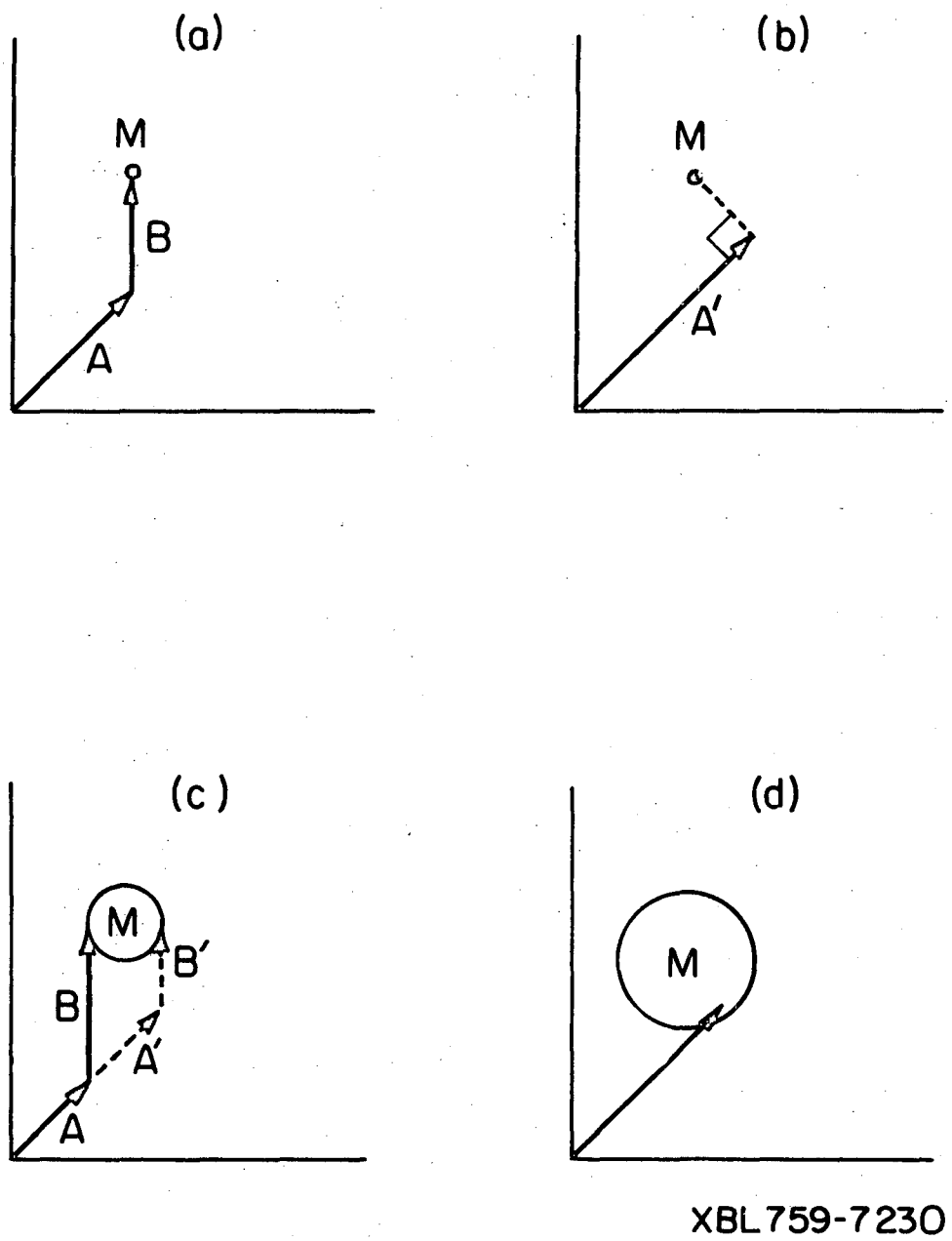

Fig. IV.5. Illustration of 2-dimensional fitting procedures.

for orthogonal vectors. The adequacy of the one vector model is judged by how close it comes to the circle. There is no justification for adding a second vector if the single vector producer a point within the error limits.

It is useful to develop a measurement of the orthogonality of the parameters in a model. The N-point interferogram in our experiment can be treated as an N-dimensional vector. Over any small range in column density, the separate interferograms for H_2O, O_3 and O_2 are vectors whose magnitude is a function of the column density. The interferogram for a blackbody spectrum or any other source can be added to the set of model vectors. Computing the scalar product between these vectors gives a measure of their orthogonality. It is found that the model vectors are closer to orthogonal when longer interferograms are used. This is in agreement with our intuition that as the resolution is increased the various spectra become more distinguishable.

The requirements of obtaining high resolution spectra and low noise are conflicting. This is easily seen when a step apodizing function ($A(x)=1$ for $x<x_{max}$ and $A(x)=0$ for $x>x_{max}$) is substituted into Eq. (III.1) for the spectral noise, giving

$$\langle N^2(\nu) \rangle^{1/2} = \frac{1}{\Delta\nu} \frac{n}{\sqrt{T}} \qquad \text{(IV.15)}$$

where n[V/$\sqrt{Hz}$] is still the detector noise, T[sec] the total observing time, and $\Delta\nu$[cm^{-1}] the nominal resolution given by Eq. (II.4). Thus for a measurement of fixed duration, you gain resolution at the expense of increased noise. The height of a sharp unresolved feature increases linearly with resolving power (longer interferogram) so that the signal to noise ratio remains constant if the total observing time remains constant. Of course the increased resolution aids in identification and separation of features. For a broad resolved feature, decreasing $\Delta\nu$ doesn't change its height and the signal-to-noise ratio decreases linearly with increasing resolution (assuming a constant total observing time). Mather (1974, p.157) shows that the minimum noise for a given apodizing function (or equivalently, a given resolution function) is achieved when the time spent measuring a given interferogram point is proportional to the apodizing function at that point.

The organization of the interferograms we took during the flight was designed to maximize our ability to measure the CBR in the presence of atmospheric emission. Interferogram scans consisting of 64 and 256 points were measured with the zero path at the 43 rd point in both cases. This produced interferograms with effective lengths of 22, 43, and 214 points from zero path, corresponding to nominal resolutions of 2.8, 1.4, and 0.28 cm^{-1}. In Case V + VI, the points closest to zero path were measured more often; 50 times for the 22 point interferograms, 27 times for the 43 point interferograms, and twice for the 214 point

interograms. The long path data allowed us to separate and quantify the atmospheric lines, while the extra observation time near zero path increased the signal-to-noise ratio for low resolution features. The longest interferograms were high enough resolution to make the model interferograms nearly orthogonal; the normalized scalar product being less than 1% for any combination of molecular line emission and 3K blackbody interferograms. This orthogonality greatly diminished the model fitting problems discussed above.

The relationship between spectral resolution and spectral noise in the flight data is demonstrated in Fig. IV.6. This is a sequence of spectra computed from the averaged interferogram for Case V + VI with apodization varying from long (214 points) unapodized at the bottom to short (43 points) quadratic apodization at the top. The spectral noise can be estimated by looking at the region above 40 cm^{-1} where there is no optical signal. The resolution (FWHM) and spectral noise ($\pm$ 1σ) are indicated in the right hand side of the figure. Note the dramatic decrease in noise at low resolution when the apodization emphasizes the points near zero path which have the longest integration time.

There are several different procedures which could have been used to fit a calculated spectrum to our flight data. We chose to Fourier transform the calculated spectrum and do a least squares fit to the measured interferogram. [The interferometer corrections determined were applied to the calculated spectrum before taking the Fourier transform.] The difference between the calculated and measured

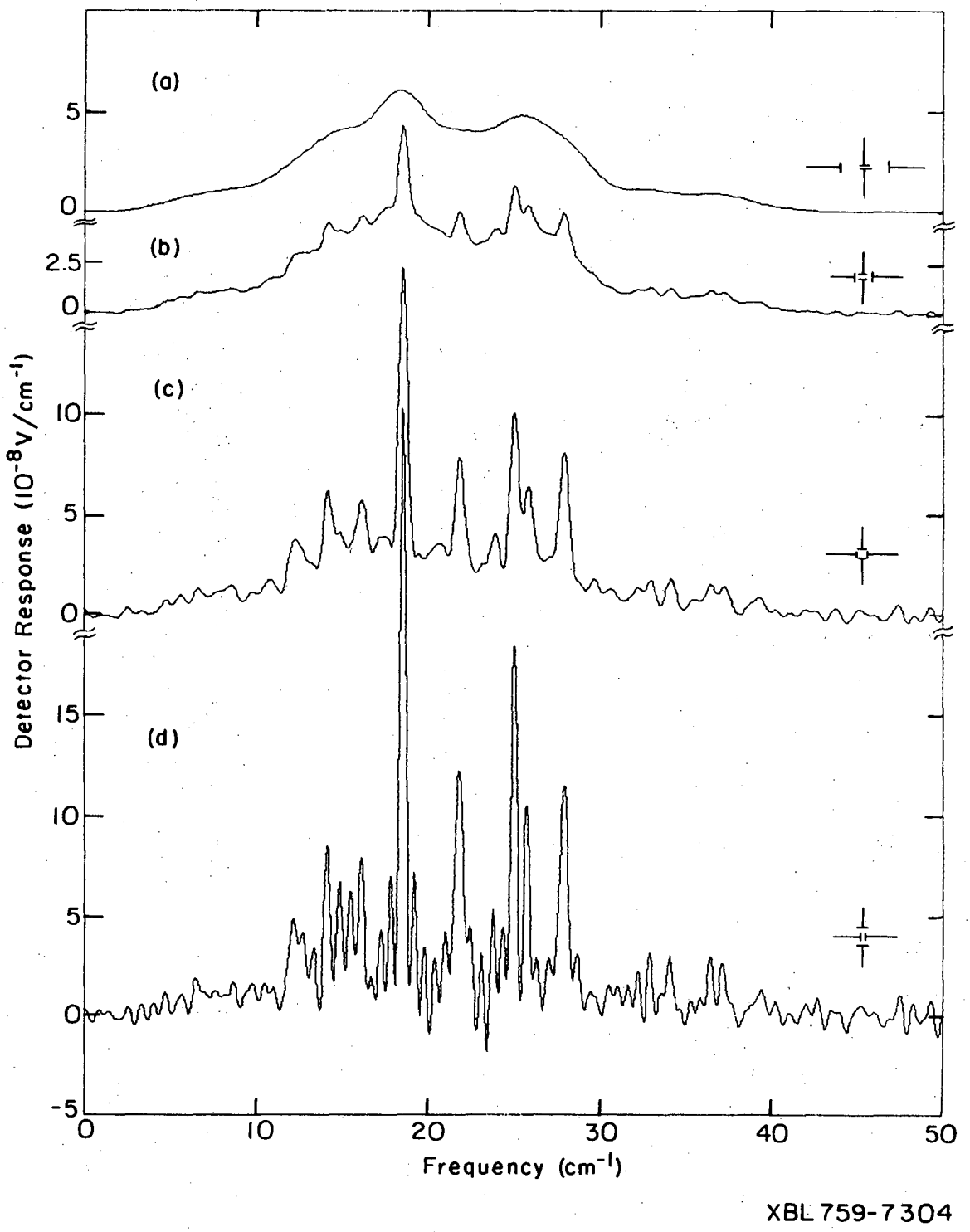

Fig. IV.6. Observed night sky emission spectrum at different resolutions.

interferograms was Fourier transformed to obtain the difference between the two spectra.

Making the comparison in interferogram space offered several advantages. It was not necessary to convolve the calculated spectrum with the instrumental resolution curve computed from an apodizing function. This was already taken into account by comparing interferograms of equal length. The proper weighting of the data points was also easily done. The points near zero path which had more integration time were simply given more weight in the least squares fitting procedure. In addition, no information or integration time was lost from the use of an apodizing function.

The basic model we used to simulate the night sky spectrum consisted of the emission spectra for the three molecular species H_2O, O_3 and O_2 plus a blackbody spectrum to simulate the CBR. The vertical column density of O_2 was fixed at 1.54×10^{22} mol/cm^2 (or 1.69×10^{22} mol/cm^2 for a zenith angle of 24°) by its mixing ratio of 21% and the measured pressure of 3.4 mbar. The concentrations of H_2O and O_3 vary from day to day, so their column densities are left as free parameters to be determined by the fit. The temperature of the blackbody used to simulate the CBR was also a free parameter.

This model was fit to the composite interferogram for Case V + VI. The best fit values for the three free parameters were as follows: a vertical column density of 3.92×10^{17} mol/cm^2 (4.30×10^{17} mol/cm^2 at a zenith angle of 24°) for H_2O, a vertical column density of 3.50×10^{17} mol/cm^2 (3.87×10^{17} mol/cm^2 at a zenith angle of 24°) for O_3 and a

temperature of 2.99K for the blackbody temperature of the CBR. The rms value of the residual from the fit was 4.12×10^{-8} V when normalized to the error in any single data points in a single scan.

There is no evidence of systematic deviation between the calculated interferogram and the measured data. The residual is within the error limits for the interferogram noise discussed in chapter III. A statistical analysis showed that both the residual interferogram and its Fourier transform are consistent with a gaussian distribution of errors with a standard deviation of 4.0×10^{-8} V.

The spectrum of the CBR is obtained by subtracting the atmospheric contribution to the night sky spectrum from the observed spectrum. This is done in Fig. IV.7. The top spectrum is the observed spectrum and the one below it is the best fit atmospheric contribution determined above. The CBR spectrum is shown at several different resolutions. Figure IV.8 shows the $\pm$ 2σ error limits on the CBR spectral flux computed from the residuals shown in Fig. IV.7 (c), (d), and (e) together with the spectral flux for a 2.99K blackbody.

D. Earthshine Correction

The contributions to the observed night sky spectrum from earthshine and other sources of continuum radiation in the wings of the antenna pattern are difficult to determine. We obtained a rough estimate of the earthshine contribution using the spectra obtained at two different zenith angles and the analytic formula for the antenna pattern in Eq. (II.18). The increment in earthshine upon increasing the zenith angle from 24° (Case I) to 45° (Case IV) was used to check the validity

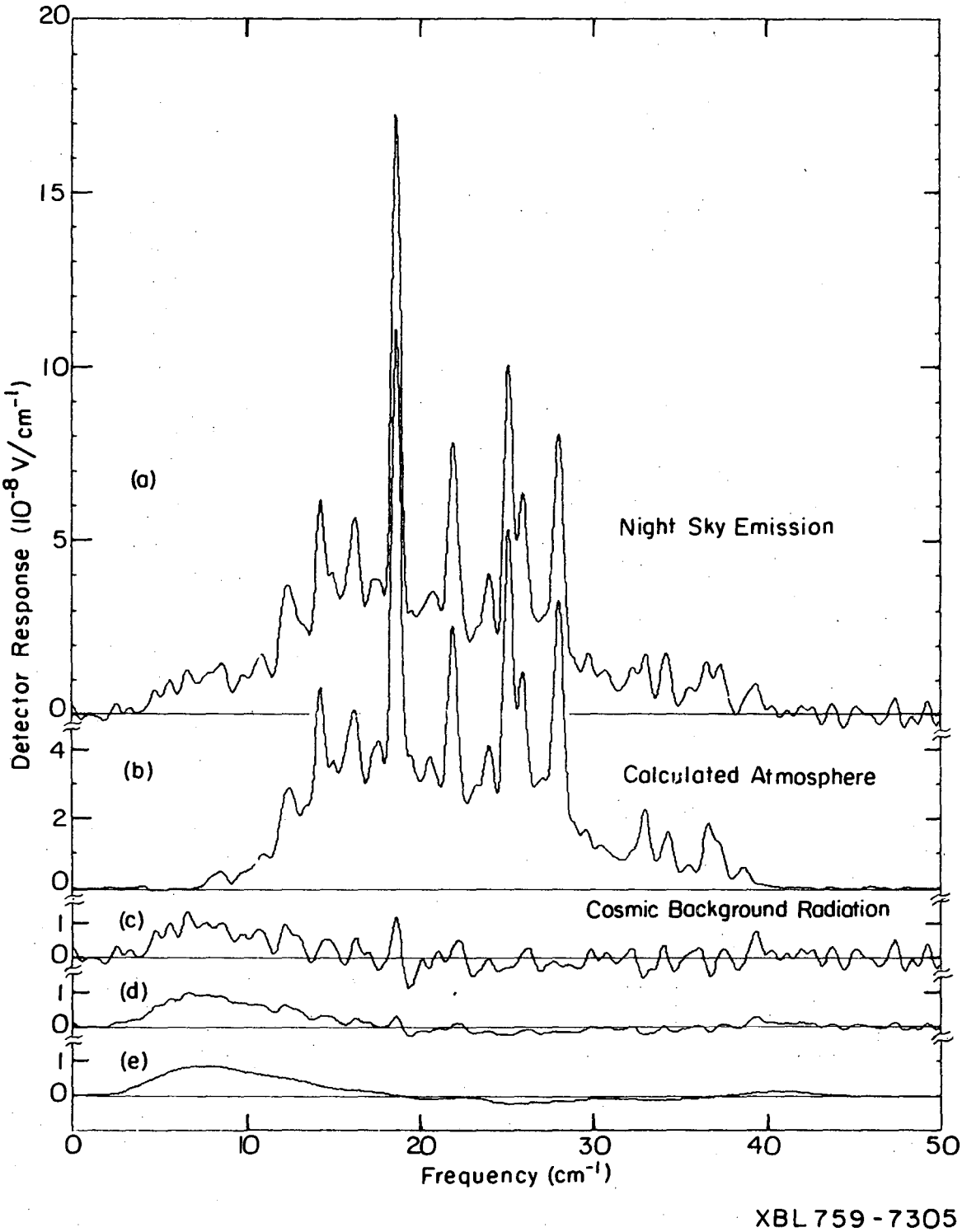

Fig. IV.7. (a) Night sky emission spectrum, (b) calculated best fit atmospheric spectrum, (c,d and e) CBR spectrum (residual of (a) - (b)) at three different resolutions.

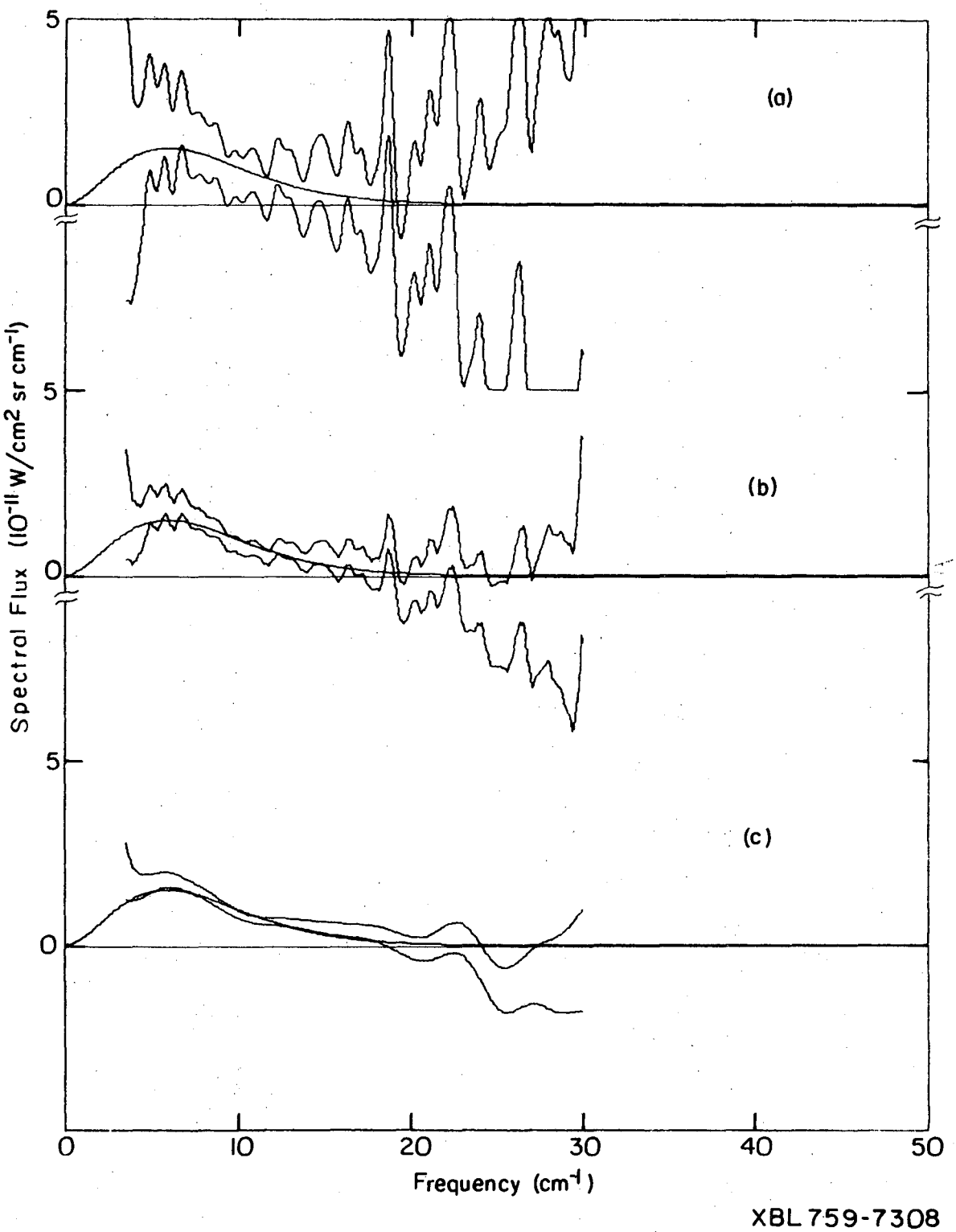

Fig. IV.8. The ±2σ error limits on the CBR spectral flux together with the Planck curve for a 2.99K blackbody.

of calculations based on the analytic form for the antenna pattern.

It was necessary to correct the spectral difference between Case IV and Case I for the increased atmospheric emission since the column densities scale as the secant of the zenith angle. This was done using the atmospheric emission model discussed in section B and the vertical column densities determined in section C. The original spectra from Cases IV and I, the difference spectra, and the difference spectra corrected for atmospheric emission are all shown in Fig. IV.9(a). The increment in earthshine has been converted to a spectral flux in Fig. IV.9(b).

This measurement has some large uncertainties in it. Only four scans were made in Case IV so that the noise is much larger than in Case I where twenty five scans were made. Another problem was the variation in column densities as the balloon altitude changed (see Fig. III.1), which made it hard to compare spectra measured at different times. Since we are computing a small difference between two large signals, these errors are greatly amplified. The phase correction used in Case IV alone increased the high frequency increment in the earthshined by a factor of ten.

This measured increment in earthshine can be compared with that calculated from the analytic formula for the antenna pattern in Eq. (II.18). The calculated earthshine is also uncertain because there is no direct information about the backlobe response of the antenna. If the backlobe is ignored, the increment in earthshine in going from a zenith angle of 24° to 45° is 1.5×10^{-12} W/cm^{2}sr cm^{-1} independent of frequency.

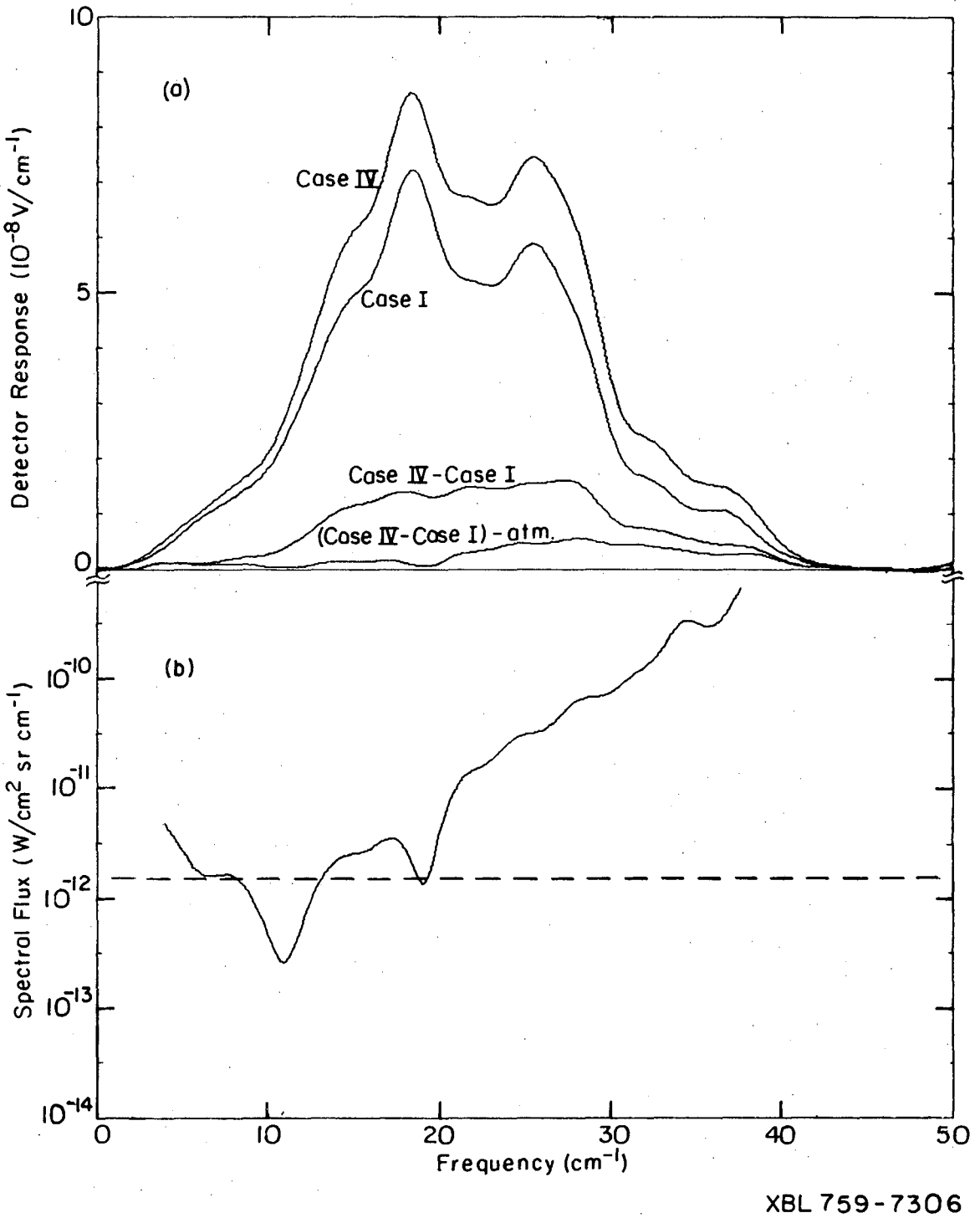

Fig. IV.9. Spectra used to estimate the earthshine contribution; (a) observed detector response a two different zenith angles and calculated differences, (b) increment earthshine calculated from inflight observations shown above (——) and calculated from measured antenna pattern (---).

This is shown as a dashed line in Fig. IV.9(b). The increment in earthshine is 1.3×10^{-12} W/cm^{2}sr cm^{-1} if Eq. (II.18) is assumed to be valid out to $\theta=\pi$ radians and the radiation coming from more $\theta=\pi/2$ off-axis (the backlobe) is included. The measurement is within a factor of three of the calculated increment over the range from 4 to 20 cm^{-1}. But the spectral shape is more nearly that expected for scattering than for double diffraction.

We can now calculate the absolute magnitude of the earthshine at the zenith angle of 24° where our best observations were made. Again the backlobe is important. If the backlobe is ignored, the earthshine increases by a factor of ≈3 upon going from 24° to 45°. Whereas the earthshine only increases by a factor of ≈1.5 if Eq. (II.18) is used all the way to the backlobe. Thus the calculated earthshine at 25° ranges from 7.5 10^{-13} to 2×10^{-12} W/cm^{2}sr cm^{-1}.

This analysis hasn't produced any reliable value for the earthshine contribution, but has shown that it could be as large as one tenth of the peak in a 3K blackbody spectrum (1.5×10^{-11} W/cm^{2}sr cm^{-1}) and should probably be put in the model for the night sky spectrum as a free parameter. The earthshine is simulated by a power law continuum in the fitting procedures discussed in the following section.

E. Error Analysis

Both the random and possible systematic errors in the CBR spectrum produced in section C have been investigated. The random errors are in the measured interferograms and show up as spectral noise. This was treated in chapter III. The systematic errors are in the calculated

model, either in the form of incorrect spectra calculations or imperfect simulation of the spectrophotometer.

There are several possible sources of systematic errors in the model. The most obvious is that something was left out of the model, such as earthshine; although the small residual for the fit done in section C indicates that it can't be anything very large. Another possibility is that including a blackbody in the model somehow biased the results. This is unlikely in light of the orthogonality between the blackbody interferograms and the atmospheric interferograms. The atmospheric model could also be in error.

A series of fitting procedures was used to check for such systematic errors. The basic model was extended to six parameters; three column densities, a blackbody temperature, plus two parameters for a power law continuum ($A\nu^{\beta}$). Any of these could be set to fixed values with the remainder being free parameters determined by the fit. The procedures used are tabulated in Table IV.1 along with the best fit values for the various parameters.

The quality of the fit is judged by the normalized rms residual r in the last column of Table IV.1. The statistical errors in this number are quite small since it is the result of averaging over the 256 independent points in the interferogram. In fact, the χ^2 value for the fit is given by

$$\chi^2 = 256 \times (r/n)^2 \qquad \text{(IV.16)}$$

Table IV.1. Fitting Procedures and Parameter Values*

#	Vertical Column Densities [molecules/cm^2]			Blackbody Temperature [K]	Continuum [$W/cm^2 sr\ cm^{-1}$]		Normalized Residual [10^{-8} V]
	$H_2O[10^{17}]$	$O_3[10^{17}]$	$O_2[10^{22}]$		Coefficient	frequency exponent	
1	3.93	3.53	1.54	2.99	≡ 0	≡ 0	4.12
2	3.92	3.51	1.66	2.99	≡ 0	≡ 0	4.11
3	3.76	3.58	1.54	2.83	≡ 2×10^{-12}	≡ 0	23.8
4	3.92	3.51	1.67	2.98	6.49×10^{-14}	0.338	4.09
5	3.71	3.22	1.54	≡ 0	1.27×10^{-12}	0.785	5.27
6	3.93	3.66	1.54	≡ 0	≡ 0	≡ 0	6.88
					use limited data		
7	4.02	3.52	1.54	≡ 0	resolution $\Delta\nu \lesssim 3.0\ cm^{-1}$		-
8	3.75	3.61	1.54	≡ 0	frequency $\nu > 17.0\ cm^{-1}$		-
					include ghosts		
					step modulation	thruput modulation	
9	3.90	3.53	1.54	2.94	2.57×10^{-2}	-1.92×19^{-3}	4.08

*Parameters values which are fixed are preceded by ≡.

where n is the actual normalized standard deviation for that interferogram noise. The expected value of χ^2 for a fit limited by random noise is 256 ± 16. Thus a variation in r of more than 3% is significant. We have no accurate way of calculating n other than using the lowest value of r obtained in the various fitting procedures.

The first six fitting procedures are straight forward. The first entry is the fit discussed in section C. The next five have different sets of fixed and free parameters. The upper estimate of the earthshine was put into fit #3 as a fixed parameter.

The fitting procedure was modified in fits #7 and #8 to increase the orthogonality between the atmospheric emission and the CBR. Only high resolution ($\Delta\nu < 3$ cm^{-1}) data was used in #7; that is only the interferogram points more than 0.17 cm from zero path were used. This prevented broad features such as the CBR from influencing the fit. Fit #8 was restricted to high frequency ($\nu > 17$cm^{-1}) spectral information. Thus the CBR was again excluded, since it is assumed to be negligble above 17 cm^{-1}. These fits suffer from a decrease in signal-to-noise in the fitted parameters because of the loss of the data not used in the fit. The rms residuals in these fits include the unfitted part of the interferogram and thus are very large.

The last fit tested for the presence of ghosts by including parameters for step size modulation and thruput modulation in the cosine (real) spectrum. The results show no indication of significant ghosts. In addition, the corrections to the sine (imaginary) spectrum discussed in chapter III had no effect on the best fit value for the

parameters in any of the fits.

There are several important conclusions that can be drawn from the data in Table IV.1. 1) The three free parameters in fit #1 (H_2O and O_3 column densities and blackbody temperature) were necessary and sufficient to produce a good fit. None of the fits had a significantly lower residual and leaving out the blackbody (#5 and #6) gave a residual more than ten standard deviations too large. 2) The column densities of H_2O and O_3 showed very little dependence upon the fitting procedure used. Comparing fit #1 and #6 shows that the column densities increased less than 3% when the blackbody is not included. The largest change was a 6% decrease when an large continuum was forced into the model (fit #3) and when the continuum was left in and the blackbody removed (fit #5). Both of these fits had an rms residual much larger than the interferogram noise. These results verify that the atmospheric model parameters are indeed orthogonal to the other fitted parameters. 3) The atmospheric model is a close approximation to the actual atmosphere. The model produces a value for the O_2 column density which is within 7% of the a priori value calculated from the mixing ratio and pressure. This is well within the accuracy of the calculation. The column densities of H_2O and O_3 are in agreement with the values obtained by Muehlner and Weiss (1973) at a similar altitude.

The limits on the vertical column densities due to systematic errors in the model are $3.9^{+.1}_{-.2}\times10^{17}$ for H_2O, $3.6\pm.1\times10^{-17}$ for O_3 and $1.6\pm.1\times10^{-22}$ for O_2. Figure IV.10 shows the CBR spectrum obtained when the upper and lower column density limits are used. For the upper

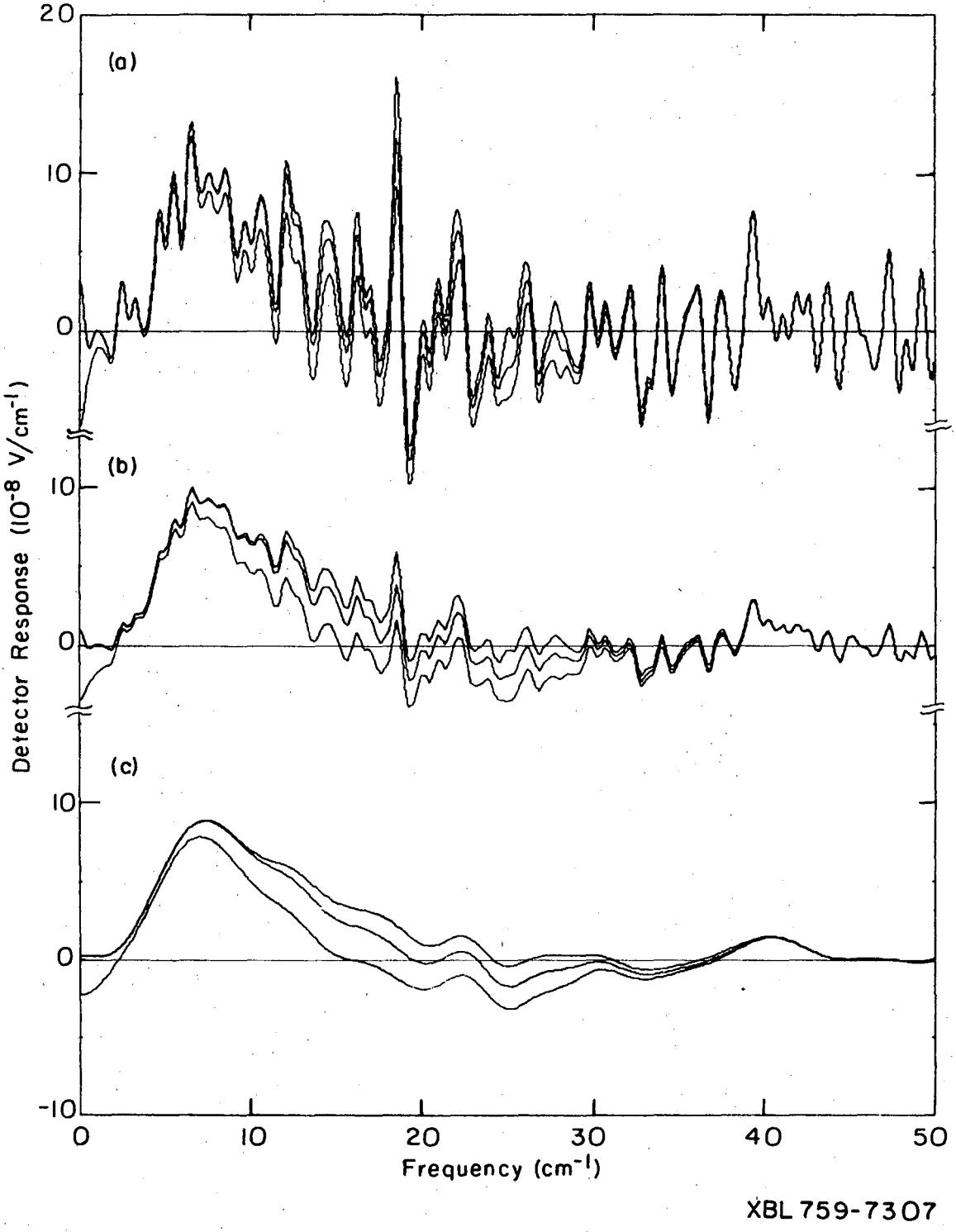

Fig. IV.10. CBR spectrum computed using the limiting values for the column densities.

limits a continuum of $6\times10^{-13}\ \nu^{1/2}$ W/cm^2 sr cm^{-1} was included (this is ten times larger than the value given by fit #4). These limits have almost no effect on the CBR near the peak in the Planck curve and do not degrade the turn over of the spectrum at higher frequencies.

Errors in the measured atmospheric parameters can effect the fit. While the pressure is measured to a few percent, the atmospheric temperature is difficult to measure accurately and could lie in the range from 205 to 250K. The largest effect from changing the temperature is in the blackbody part of the atmospheric emission calculation. This changes the column densities required to achieve a given spectral flux but has almost no effect on the spectral shape or intensity of the CBR. There is a small effect on the spectral shape because a change in temperature alters the lower state occupation numbers which changes the relative strength of the molecular transitions.

An error in the effective size or temperature of the inflight calibrator will also effect the fit. The product of the calibrator temperature and effective size is the calibration factor. Changing this calibration factor rescales the flux responsivity which will result in a shift in the column densities. Again there is no effect on the spectral shape of the CBR, but its magnitude is altered.

We have estimated the errors in the calibration factor and atmospheric temperature and calculated the resulting errors in the fitted parameters. A similar calculation was done for errors in the amount of earthshine continuum included in the model. The uncertainties in the most important parameters and the implied errors in the

blackbody temperature are shown in Table IV.2. The dominant error in this temperature comes from the uncertainty in the continuum contribution. An rms sum of the errors gives a best fit temperature for the CBR of $2.99^{+.07}_{-.14}$ K at the 90% confidence level.

We can now combine all of the error estimates to produce the limits on the CBR spectrum. The errors which are included are the interferogram noise of 4.0×10^{-8} V for any point in a single scan and the systematic errors in the model which would effect the spectral shape plus a ±10% error for the calibration factor uncertainty. The decrease in noise at low resolution can be exploited by plotting the spectrum on a log-log plot at a 20% constant fractional resolution. This improves the signal-to-noise ratio at high frequencies where the signal is diminishing. This shown in Fig. IV.11 with the error limits.

These results differ only slightly from the results we reported earlier (Woody, Mather, Nichioka and Richards, 1974). Previously we had used the results of fitting procedure #2 in Table IV.1 to calculate the CBR spectrum. In this work the number of free parameters was reduced by using the results of fitting procedure #1 which has the oxygen column density fixed at its a priori calculated value. This produced no noticeable change in the CBR spectrum. The only observeable change is in the error limits. The more thorough error analysis discussed in this work has produced slightly tighter error limits.

Our observations clearly show that the submillimeter CBR spectrum definitely does turn over and follow the 3K Planck curve at high frequencies at least until the curve has fallen to 20% of its peak

Table IV.2. Model parameters and errors

	Value with 90% confidence limits	Error in blackbody temperature[a]
Fixed Parameters:		
Atmospheric temperature	$215 \begin{smallmatrix} +35 \\ -10 \end{smallmatrix}$ K	$\begin{smallmatrix} +.05 \\ -.02 \end{smallmatrix}$ K
Calibration factor[b]	$33.2 \begin{smallmatrix} +3.3 \\ -3.3 \end{smallmatrix}$ K	$\begin{smallmatrix} +.05 \\ -.06 \end{smallmatrix}$ K
Earthshine	$0 \begin{smallmatrix} +6 \\ -0 \end{smallmatrix} \times 10^{-13} \nu^{1/2} \frac{W}{cm^2 sr\ cm^{-1}}$	$\begin{smallmatrix} -.13 \\ +.00 \end{smallmatrix}$ K
Fitted Parameters:		
H_2O vertical column density	$3.92 \begin{smallmatrix} +.20 \\ -.20 \end{smallmatrix} \times 10^{17} \frac{\text{molecules}}{cm^2}$	$\begin{smallmatrix} -.001 \\ +.001 \end{smallmatrix}$ K
O_3 vertical column density	$3.50 \begin{smallmatrix} +.18 \\ -.18 \end{smallmatrix} \times 10^{17} \frac{\text{molecules}}{cm^2}$	$\begin{smallmatrix} -.02 \\ +.02 \end{smallmatrix}$ K
O_2 vertical column density	$1.67 \begin{smallmatrix} +.17 \\ -.17 \end{smallmatrix} \times 10^{22} \frac{\text{molecules}}{cm^2}$	$\begin{smallmatrix} -.01 \\ +.01 \end{smallmatrix}$ K
Blackbody temperature[c]	$2.99 \begin{smallmatrix} +.07 \\ -.14 \end{smallmatrix}$ K	

[a] Error induced in fitted blackbody temperature by parameter errors quoted in column two.

[b] Product of calibrator temperature and filling factor.

[c] Error determined by the rms sum of the detector noise plus the errors shown in column three.

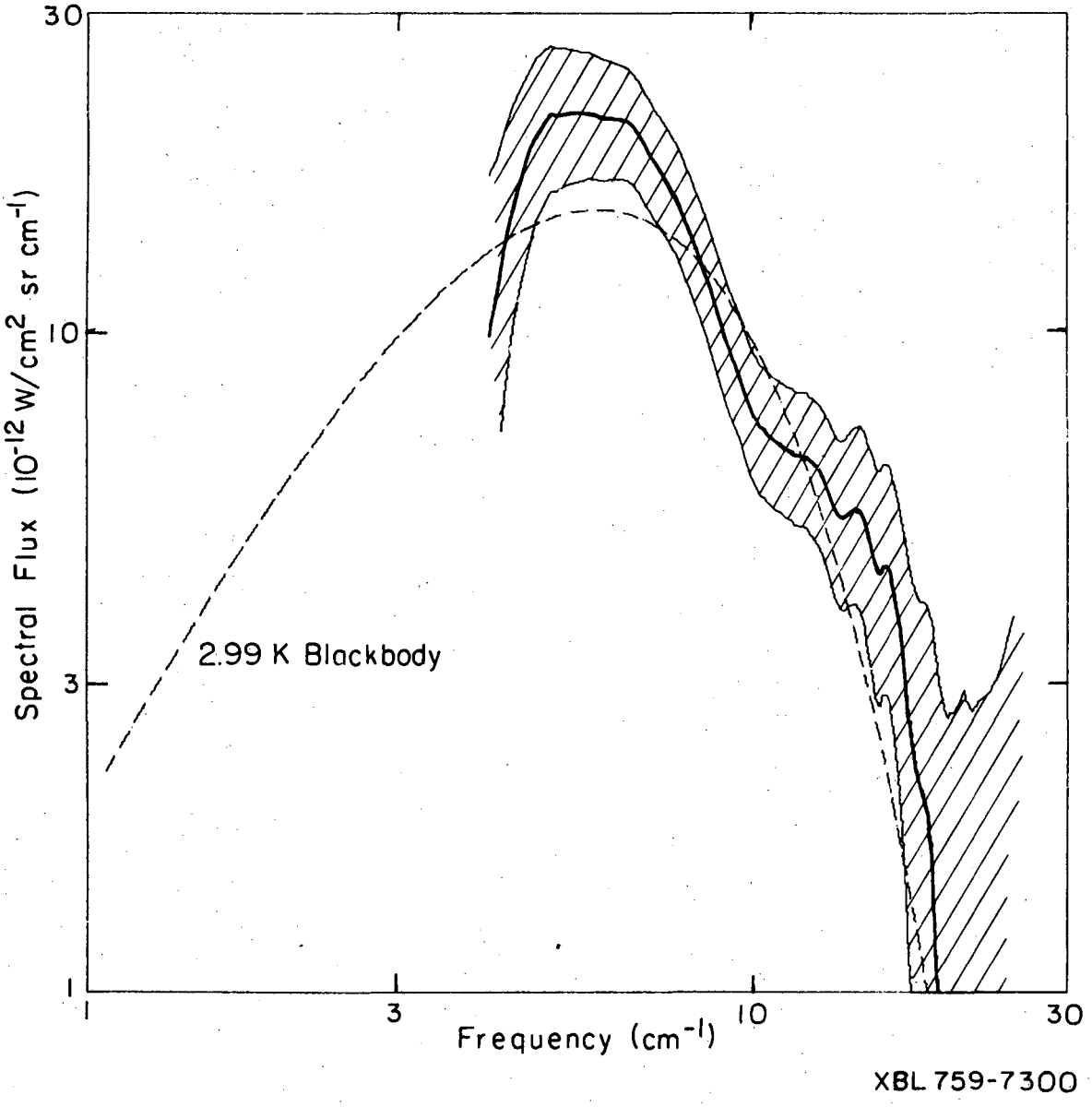

Fig. IV.11. CBR spectrum with 95% confidence limits.

value. The signal-to-noise in our measurement is greater than two in the range from 4 to 17 cm^{-1}.

V. CONCLUSION

A. Present Status of the Observations

We have measured the night sky emission spectrum at an altitude of 39 km and analyzed the data to produce the first moderate resolution spectrum of the CBR in the submillimeter frequency range (see Fig. IV.11). The instrument used was a fully calibrated liquid helium cooled spectrophotometer carried aloft by a high altitude balloon. The spectrophotometer was thoroughly characterized before the flight, including a measurement of the antenna pattern out to nearly 70° off-axis. This allowed us to determine the possible sources of contaminating radiation, mainly antenna emission and earthshine, and make corrections to the data based on inflight measurements. The calibration of the instrument during the flight agreed with the preflight laboratory calibration. The data were analyzed to remove the atmospheric contribution to the observed spectra and to check for other possible sources of radiation. The 256 independent data points were successfully fit to a model containing only three free parameters; the column densities of water and ozone (the column density of oxygen was fixed by the atmospheric pressure and known mixing ratio) and the temperature of the blackbody used to simulate the CBR. The residual from the fit was within the expected noise level. Both the random noise and possible systematic errors are included in the 95% confidence limits shown in Fig. IV.11.

Our measurement can be combined with previous observations to establish the CBR spectrum over three decades of frequency. Figure V.1 is a log-log plot of the microwave, interstellar CN and our submillimeter data. Also shown is the spectrum of a 2.9K blackbody. These measurements extend from the Rayleigh Jean's limit well into the quantum cutoff region. Our results show that the CBR does turn over and follow the Planck curve on the high frequency side of the peak.

All of the measurements are consistent with a 2.9K blackbody temperature. A convenient way to check this consistency is to convert the observed fluxes to equivalent blackbody temperature. The results of this conversion are shown in Fig. V.2. All of the data are in close agreement with a temperature of ≈3K. This can be made quantitative by carrying out a χ^2 squared analysis similar to the one Peebles (1971) used for the microwave data alone. The data point provided by our measurement is $2.99^{+.04}_{-.07}$ K. We conclude that all of the measurements over a frequency range from 0.013 to 17 cm^{-1} are consistent with a blackbody temperature of 2.90±.04K (1σ error limits). The value of χ^2 from the fit is 16, which is within the range 18±6 expected for 19 independent measurements. The most recent broadband submillimeter measurements (Muehlner and Weiss, 1973; Houch, et al, 1972; Williamson, et al., 1973) are in agreement with this value and don't affect its precision. The Los Alamos work (Williamson, et al., 1973) extends the measurement to 33 cm^{-1} but at low precision. The Queen Mary College report (Robson, et al., 1974) did not provide any temperature or error limits which could be included in this analysis.

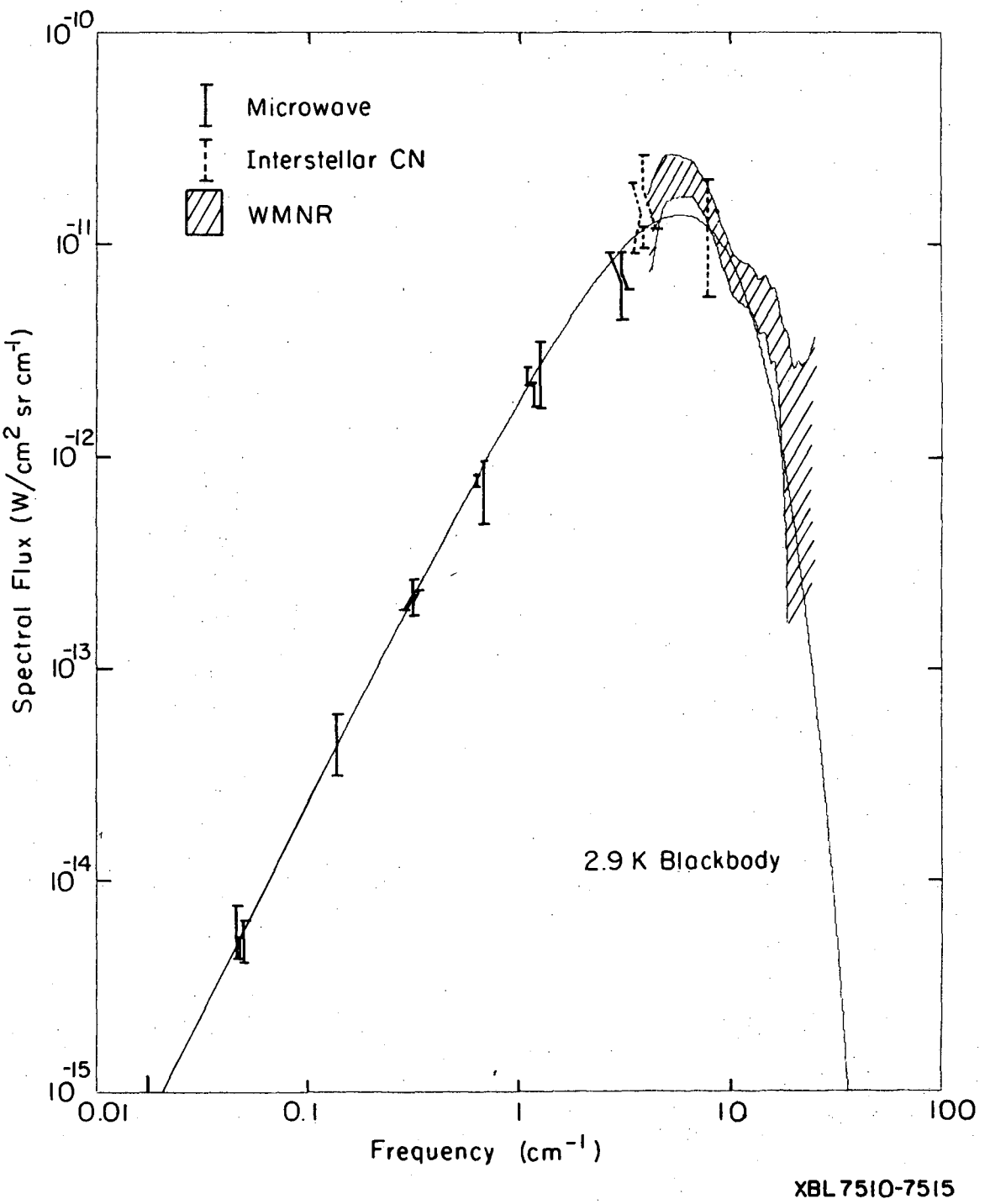

Fig. V.1. Plot of the microwave, interstellar CN and our submillimeter data.

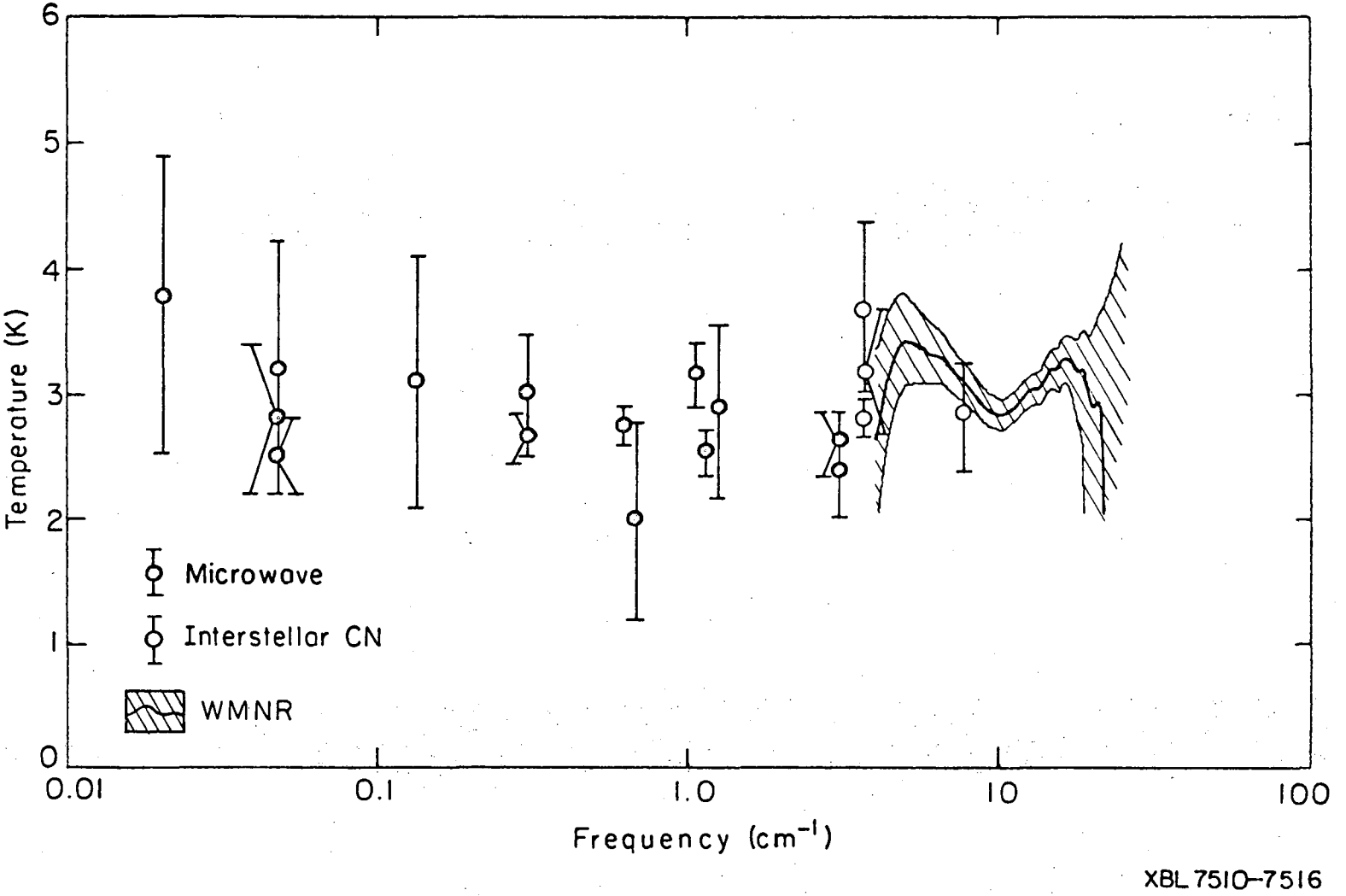

Fig. V.2. Blackbody temperatures depaced from the individual observations.

Many experiments have been carried out to measure any anisotropy in the CBR (Peebles, 1971, p.39 and the references given there). These measurements have been made using groundbased microwave radiometers with sensitivities as high as 0.1%. No definite anisotropy has been detected at angular resolutions ranging from a few minutes of arc to a full 24 hour sidereal variation.

These spectral and anisotropy measurements firmly support the "Big Bang" cosmological model and requires that any alternative model produce a universe filled with ≈2.9 blackbody radiation.

B. Future Experiments

The next step is to improve the sensitivity of the measurements and look for deviations from an ideal blackbody. Just as the present observations tell us about the general evolutionary history of the universe, any deviations from a blackbody will have to be explained by the details of that evolution at the time the radiation last interacted with the matter.

A promising approach is to look for anisotropy in the CBR. The next generation of microwave measurements will have greatly increased sensitivity (Alvarez, et al., 1974). They expect to detect the motion of the earth relative to the comoving reference frame of the Universe; in particular, the motion of the earth around the sun. Muehlner and Weiss at M.I.T. have modified their apparatus to measure the anisotropy of the submillimeter CBR (private communication). The fractional change in signal for a given change in temperature should be larger at

the higher frequencies where the flux depends exponentially upon the temperature.

It is also of interest to look for deviations in the spectral flux of the CBR. A convenient way to display the data for analysis of such deviations is to plot the photon occupation spectrum, since this is an invariant scalar quantity. The occupation spectrum is derived from the observed spectral flux by dividing by the density of states and the photon energy

$$N(\nu) = I(\nu)/2h\nu^3c^2 \qquad (V.1)$$

where $I(\nu)$ is the spectral flux and ν the frequency in cm^{-1}. This can be compared with a universal plot plot of the occupation number as a function of $x \equiv hc\nu/kT$ for a blackbody. Figure V.3 is a plot of this universal curve $[N(x) = (\exp(x) - 1)^{-1}]$. The observations in Fig. V.1 have been added to the plot assuming a value of 2.9K for temperature in the equation for x. Altering the temperature corresponds to shifting the data to the left or right. Decreasing the blackbody emissivity corresponds to shifting the universal curve downward.

A possible perturbation to the CBR is that it interacted with matter sometime after the initial combining of the electrons with the nuclei to form neutral atoms. This might have occurred during the formation of galaxies if the matter became re-ionized. The CBR could establish equilibrium with the matter through photon conserving Compton scattering, but with the Bremsstrahlung process too slow to establish an equilibrium

number of photons. There would not be enough photons to produce a blackbody distribution if the matter were hotter than the radiation. In this case, Bose-Einstein statistics would still apply, but with a nonzero chemical potential μ

$$N(\nu,T,\mu) = [\exp \frac{hc\nu+\mu}{kT} - 1]^{-1} . \qquad (V.2)$$

The chemical potential is set by requiring the total number of photons to be correct. As the universe expands, the number density distribution is retained, but μ scales the same way as T; so that μ/kT can be added to the universal curve of N vs. x and are shown in Fig. V.3. The biggest effect is seen at low frequencies where the photon modes are depleted. The data put a limit on of $\mu/kT < 0.001$.

This type of analysis has been carried out in much greater detail (and in terms of the spectral flux) by Chan and Jones (1975 and 1975). They carry out a time-dependent numerical analysis which includes both Compton and Bremsstrahlung processes.

Other as yet unexpected perturbations in the early evolution of the universe may be revealed as the precision of the spectral measurements improves.

Contrary to the work of Noerdlinger (1973), the observed data don't give information about the secular variation in Planck's constant in this interpretation. The density of states is determined locally and the occupation number is a function of the single dimensionless quantity $x=hc\nu/hT$. The consistency between different types of measurements may

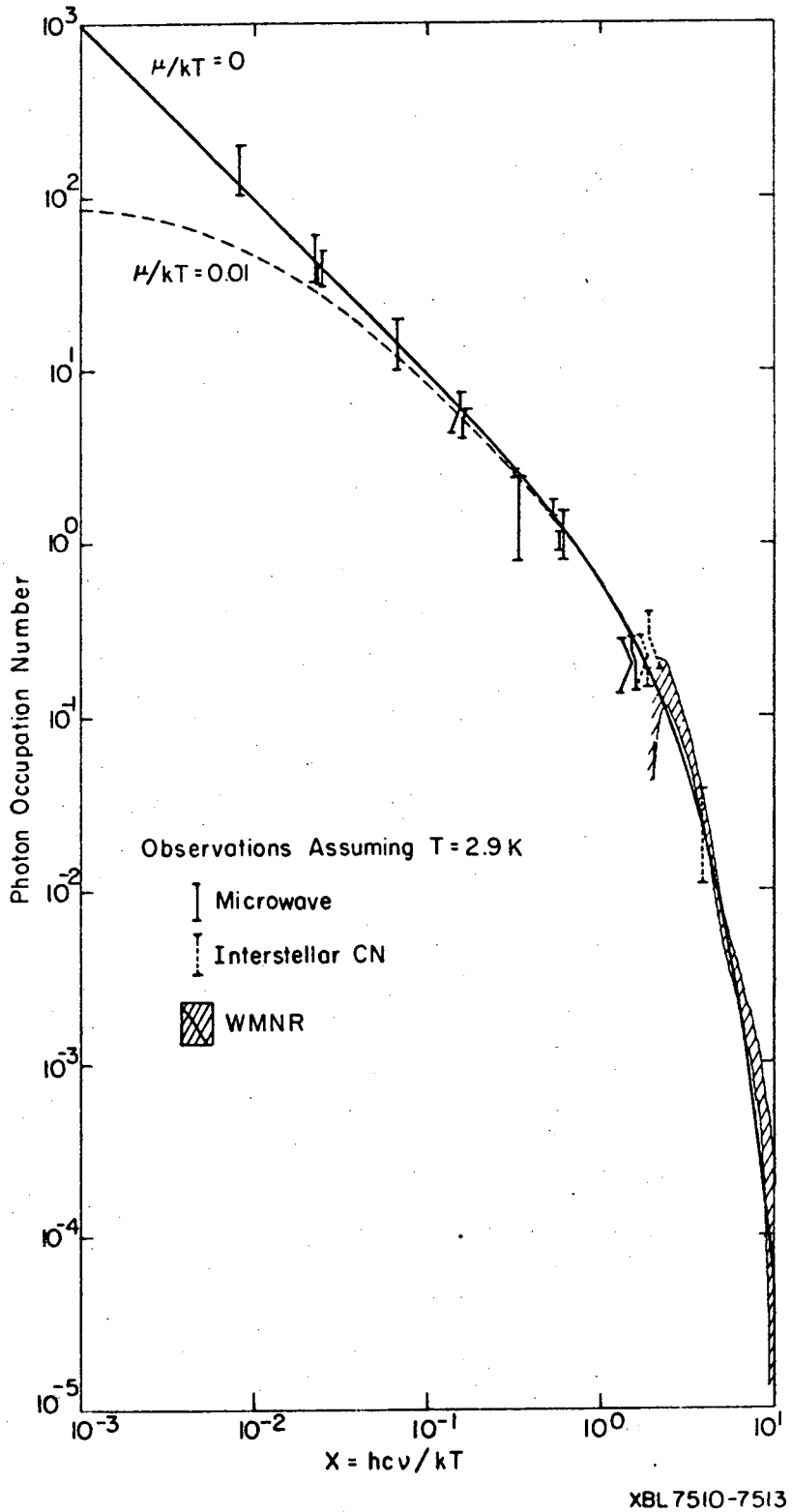

Fig. V.3. Plot of the photon occupation number depaced from the observations assuming T=2.9K.

test for variation in the speed of light, however, since the microwave observations measured the frequency and we measured the wavelength.

The future of measurements of the CBR promises to be very interesting. The sensivity of the measurements is steadily improving and significant unexpected features are bound to be found. We are repeating our experiment with a factor of ten improvement in sensitivity in 1976. Dr. J. Mather is proposing to repeat our measurement from a satellite. There also are satellite proposals for anisotropy measurements. A satellite measurements would avoid the one large problem of the atmospheric emission and provide for many months of observation time. It will still have the same problems of instrumental and earthshine contamination that we observed. With our better sensitivity and higher altitude we will come close to reaching the limit for terrestial submillimeter measurements of the CBR spectrum.

APPENDIX A

Low Emissivity Material for Use in Cryogenic Applications

We have fabricated a laminated material with a very low emissivity at sub-mullimeters wavelengths and low thermal conductivity which can be cycled to low temperatures. It consists of a stainless steel backing which is electroplated with copper and coated with a pro-reflection coating of polyethylene. The low emissivity (high reflectivity) is produced by ≈ 25 μm of copper which has a high electrical conductivity. The copper also dominates the transverse thermal conductivity. Mechanical strength is provided by the 127 μm thick stainless steel sheet. The theory and measurement of the optical properties of this composite is discussed in part 2 of section D in chapter II.

The difficult part of the fabrication procedure for this material is applying the 50 μm polyethylene coating. The starting material is 50 μm polyethylene film heated to ≈ 115°C. No additional adhesive is required. Figure A.1 shows how the layers are assembled before heating in a vacuum oven. The layers are tightly wrapped around a cylinder to bring the polyethylene into good contact with the copper. It is critical that the surfaces which are to be joined be clean. The polyethylene is wiped with xylene which actually removes a surface layer of material. The copper is vapor degreased in trichloroethylene. A teflon sheet is used to keep the polyethylene from sticking to the back of the stainless steel. This assembly is evacuate to ≈10 μm of Hg for ≈ 12 hours and then heated to 115°C for ≈ 1 hour. This

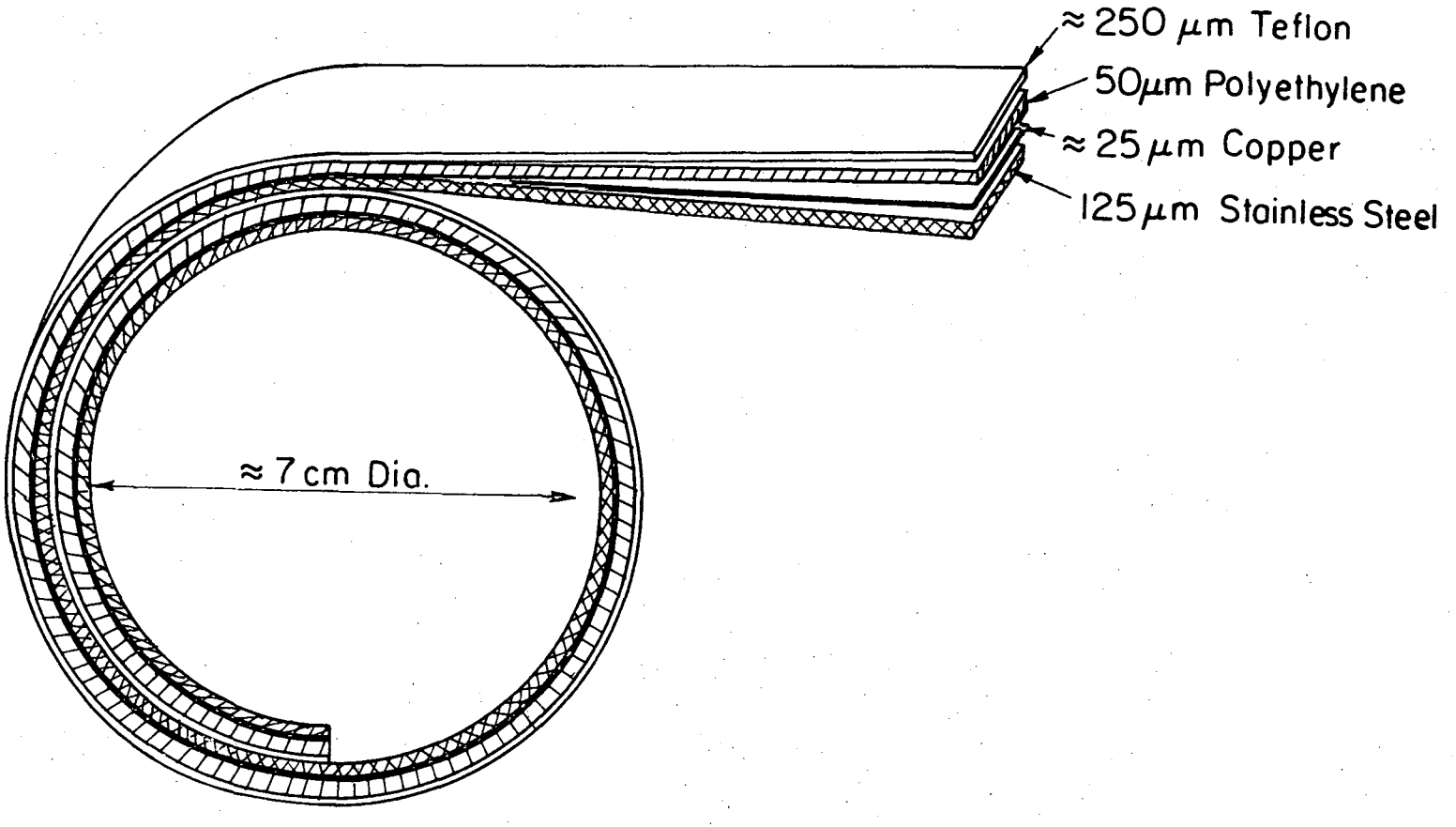

Fig. A.1. Laminating polyethylene to copper plated stainless steel.

produces a firm bond which can withstand the stress of cooling to liquid helium temperatures.

APPENDIX B

A Program to Calculate the Optical Properties of a Stratified Medium

STRAD is a program which calculates the reflectivity, absorptivity, and transmissivity of a plane stratified medium. It uses the method of characteristic matrices described by Born and Wolf (1970, p.55). A single homogeneous layer is characterized by a 2×2 complex matrix whose coefficients are a function of the complex index of refraction, thickness, optical frequency and direction of propagation. There are separate matrices for the TE and TM modes. This method is valid for any medium in which the propagation of a plane wave is described by a complex index of refraction. A combination of any number of layers is characterized by the product of the individual matrices.

The version of STRAD listed below is a general purpose program. It has been written in modular form to make it easy to follow and modify. The input data cards can direct the program to perform a large number of different calculations. The optical properties of a plane stratified medium consisting of up to ten layers can be calculated for a series of frequencies, angle of incidence and thickness of the layer. The complex index of refraction for each layer can be derived from a choice of input parameters, such as the dielectric constant or the d.c. electrical conductivity. Even the anomalous skin and relaxation effects described in chapter II can be included in the calculations. The results can be displayed in several different different ways, including in the form of a Cal-Comp plot.

Program Control Cards

A set of data cards is required for each series of calculations about a given stratified medium. Any number of different calculations can be done by in including additional sets of cards.

1. Title: Any title in col 1-80; a blank field in the first 10 columns terminates the program.

2. Execution data: Data telling the program what to calculate;

col. 1-2 (I2) number of layers (10 or less)

col. 3-4 (I2) variable for x-axis

1 = wavenumber

2 = angle of incidence

I+2 = thickness of the Ith layer

col. 5-6 (I2) variable for y-axis; same code as for x-axis

col. 7-8 (I2) property to be calculated (z-axis)

1 = reflectivity for TE mode

2 = reflectivity for TM mode

3 = transmissivity for TE mode

4 = transmissivity for TM mode

5 = absorptivity for TE mode

6 = absorptivity for TM mode

col. 9-10 (I2) whether to average over angle of incidence

0 = don't average

1 = weighted average
$F = \int F(\theta) 2\pi \cos\theta \sin\theta d\theta / \int 2\pi \cos\theta \sin\theta d\theta$

col. 11-12 (I2) what to print in output

0 = no printing

1 = density plot, y-axis across page (upto 20 different values), x-axis down page, the value of the calculated property (z-axis) is printed

2 = straight listing, one line for each calculation, all six properties are calculated and printed, the x-axis variable is varied most rapidly.

col. 13-14 (I2) plot information

0 = no plot

1 = plot calculated property (z-axis) as a function of x-axis variable

2 = special plot of calculated property as a function of angle from grazing incidence

Note: If a plot is done, there is no printing of the calculated results.

3. Wavenumber limits:

col. 1-10 (E10.3) smallest wavenumber

col. 11-20 (E10.3) largest wavenumber

col. 21-30 (E10.3) wavenumber increment

4. Angle limits:

col. 1-10 (E10.3) smallest angle from normal incidence

col. 11-20 (E10.3) largest angle from normal incidence

col. 21-30 (E10.3) angle increment

5. Incident Medium:

col. 1-2 (I2) code for calculating complex index of refraction N

col. 3-22 (2E10.3) D_1, D_2 data from which the complex index of refraction is to be calculated

code = 0, complex index of refraction is given

= 1, complex dielectric constant is given

= 2, real dielectric constant and conductivity in esu units in given

= 3, conductivity in esu is given as D_2

= 4, impedence in ohms per square is given as D_1

= 5, conductivity and electron density is given for use in anomalous skin effect calculation

6. Exit medium: same data as required for the incident medium.

7. Layer data: one card for each layer

col. 1-22 (I2, 2E10.3) complex index of refraction data, same data as required for the incident medium.

col. 23-32 (E10.3) minimum thickness of layer in cm.

col. 33-42 (E10.3) maximum thickness of layer.

col. 43-52 (E10.3) thickness increment

If no plotting is to be done, another set of cards starting with the title card can be added. A blank card here terminates the program.

If a plot is to be done, a set of plot data cards is required. These cards are the input data for a general purpose plotting subroutine (SKETCH) based on the LBL Cal-Comp plotting package.

1. Title Control:

col. 1-10 (A10); determines plot sequence

NO PLOT , nothing is plotted.

, nothing is plotted.

NEW PLOT , plot on a new section of paper.

SAME PLOT , plot on top of last plot using same coordinates, cards 2 thru 7 are not used.

SAME SET__, plot on a new section of paper using coordinate data from last plot, cards 6 thru 7 are not used.

NEW RANGES, plot on top of the last plot but with new coordinate data, cards 4 thru 7 not used.

PLOT GRID_, plot just the coordinates.

Anything else in interpreted as NEW PLOT__.

col. 11-16 (A6); determines whether or not to write the values for the coordinate variables.

LABELS___ write the values.

NOLBLS___ don't write the values.

col. 17-20 (I4); character size for title (usually 2).

Letter height = character size × 0.06 inches.

col. 21-24 (I4); maximum number of characters in title (usually 80)

col. 25-28 (I4); character size for program identification (usually 1)

col. 29-32 (I4); maximum number of characters in identification (usually 40)

col. 33-52 (2E10.3); x and y paper coordinates in inches for locating title (usually 0.0, 10.2)

col. 53-72 (2E10.3); x and y paper coordinates for locating identification (usually 0.0, 10.4)

2. Coordinate ranges: determines coordinate limits.

col. 1-10 (E10.3); minimum for x coordinate.

col. 11-20 (E10.3); maximum for x coordinate.

col. 21-30 (E10.3); minimum for y coordinate.

col. 31-40 (E10.3); maximum for y coordinate.

col. 41-50 (E10.3); determines whether a linear or log x-axis is to be used.

≤ 0.0 gives a linear plot.

> 0.0 gives a log plot.

col. 51-60 (E10.3); determines whether a linear or log y-axis is to be used.

3. Plot location: determines the size and location of the plot in inches measured from the lower left corner of the paper.

   col. 1-10 (E10.3); beginning of x-axis (usually 1.0)

   col. 11-20 (E10.3); end of x-axis

   col. 21-30 (E10.3); beginning of y-axis (usually 1.0)

   col. 31-40 (E10.3); end of y-axis (usually less than 10.0)

4. x-axis data:

   col. 1-4 (I4); number of divisions separated by grid lines ($\geq$ 1).

   col. 5-8 (I4); number of subdivisions separated by large tic marks ($\geq$ 1).

   col. 9-15 (I4); number of subdivisions separated by small tic marks ($\geq$ 1).

   col. 13-16 (I4); character size for x-axis label.

   col. 17-20 (I4); maximum number of characters (usually 80).

   col. 21-40 (2E10.3); paper coordinates for locating x-axis label (usually 1.0, 0.1).

5. y-axis data: same data as for the x-axis. The maximum number of characters is usually 40 and the coordinates are usually 0.0, 1.1.

6. x-axis label:

   col. 1-80 (8A10); anything

7. y-axis label:

   col. 1-80 (8A10); anything

Another series of calculations can be done by starting again with the title card in the program control card set.

```
STRAD,7,70000.406812,HOGGY
*USERPK
*NOSTAGE
MNF.
LINK,P=SYSLIB,X.
EXIT.
DUMP,0.
C****** 789 CARD
C
C
      PROGRAM STRAD1(INPUT,OUTPUT,PUNCH,PLOT,TAPE98,TAPE99=PLOT)
      COMMON /JOBDATA/ JTITLE(8),JIDENT(4)
      DIMENSION PARAM(12),PSTRT(12),PEND(12),PDLTA(12),FOUT(6)
      COMPLEX CINDIN,CINDOUT,CINDEX
      COMMON/LAYDATA/WAVNUM,ANGLE,THICK(10),RTE,RTM,TTE,TTM,ATE,ATM
     1   ,NUMLAY,INDIN,D1IN,D2IN,INDOUT,D1OUT,D2OUT,IND(10),D1(10)
     2   ,D2(10),CINDIN,CINDOUT,CINDEX(10)
      COMMON/PRMTR/WAVSTRT,ANGSTRT,THSTRT(10),WAVEND,ANGEND,THEND(10)
     1   ,WAVDLTA,ANGDLTA,THDLTA(10)
      EQUIVALENCE (PARAM(1),WAVNUM),(PSTRT(1),WAVSTRT),(PEND(1),
     1    WAVEND),(PDLTA(1),WAVDLTA),(FOUT(1),RTE)
      JIDENT(1)=10H  PROGRAM
      JIDENT(2)=10H STRAD1
      CALL DATE(JIDENT(3))
      CALL HOUR(JIDENT(4))
      PI=4.0*ATAN(1.0)
   10 READ 100, JTITLE
  100 FORMAT (8A10)
      IF (JTITLE(1) .EQ. 10H           ) GO TO 1000
      PRINT 50, JTITLE,JIDENT
   50 FORMAT (1H1,5X,8A10,4X,4A10,//)
      READ 110, NUMLAY,IX,IY,IZ,KAVRG,KPRNT,KPLOT
  110 FORMAT (9I2)
      IF (IX .LT. 1) IX=1
      IF (IZ .LT. 1) IZ=1
      READ 120, WAVSTRT,WAVEND,WAVDLTA
  120 FORMAT (3E10.3)
      PRINT 125, WAVSTRT,WAVEND,WAVDLTA
  125 FORMAT (* WAVNUMBER RANGE *,F8.2,* CM-1 TO *,F8.2,* CM-1 IN STEPS
     1OF *,F8.2,* CM-1*)
      READ 120, ANGSTRT,ANGEND,ANGDLTA
      PRINT 127, ANGSTRT,ANGEND,ANGDLTA
  127 FORMAT (* ANGLE FROM NORMAL  *,F8.5,* RADS TO *,F8.5,* RADS IN STE
     1PS OF *,F8.5,* RADS*)
      IF (KAVRG .EQ. 1) PRINT 128
  128 FORMAT (*  A LAMBERTIAN AVERAGE OVER THE ANGULAR RANGE IS PERFORME
     1D *)
      PRINT 129
  129 FORMAT (//,*   INDEX COMPUTATION CODE AND DATA*,20X
     1   ,* LAYER THICKNESS DATA IN CENTIMETERS*)
      READ 130, INDIN,D1IN,D2IN
  130 FORMAT (I2,5E10.3)
      PRINT 135, INDIN,D1IN,D2IN
  135 FORMAT (* INCIDENT MEDIUM *,I2,2X,2(1X,1PG10.3))
      READ 130, INDOUT,D1OUT,D2OUT
      PRINT 140, INDOUT,D1OUT,D2OUT
  140 FORMAT (*   EXIT   MEDIUM *,I2,2X,2(1X,1PG10.3))
      IF (NUMLAY .LT. 1) GO TO 300
      DO 200 I=1,NUMLAY
      READ 130, IND(I),D1(I),D2(I),THSTRT(I),THEND(I),THDLTA(I)
      PRINT 180, I,IND(I),D1(I),D2(I),THSTRT(I),THEND(I),THDLTA(I)
```

```
  180 FORMAT (* LAYER NO. *,I2,4X,I2,2X,2(1X,1PG10.3),3X,*FROM *
     1   ,1PG10.3,* CM TO *,1PG10.3,* CMM IN STEPS OF*,1PG10.3,* CM*)
  200 CONTINUE
  300 CONTINUE
      NUMPRM=NUMLAY+2
      DO 400 I=1,NUMPRM
  400 PARAM(I)=PSTRT(I)
      IL=1
      IF (IX .GT. 2) IL=IX-2
      IF (IY .GT. 2) IL=IY-2
      IF (KPLOT .EQ. 2) KPRNT=0
      IF (KPRNT .GE. 2) CALL LISTOUT(KPRNT,KAVRG,IX,IY,IZ,IL)
      IF (KPRNT .EQ. 1) CALL XYZPRNT(      KAVRG,IX,IY,IZ,IL)
      IF (KPLOT .EQ. 1) CALL PLOTFIL(IX,IZ,IL,KPRNT,KAVRG)
      IF (KPLOT .EQ. 2) CALL LOGPLOT(IZ,KPRNT)
      GO TO 10
 1000 CONTINUE
      IF (KPLOT .GT. 0) CALL CCEND
      STOP  $  END
C
C
      SUBROUTINE LISTOUT(KPRNT,KAVRG,IX,IY,IZ,IL)
      DIMENSION PARAM(12),PSTRT(12),PEND(12),PDLTA(12),FOUT(6)
      COMPLEX CINDIN,CINDOUT,CINDEX
      COMMON/LAYDATA/WAVNUM,ANGLE,THICK(10),RTE,RTM,TTE,TTM,ATE,ATM
     1   ,NUMLAY,INDIN,D1IN,D2IN,INDOUT,D1OUT,D2OUT,IND(10),D1(10)
     2   ,D2(10),CINDIN,CINDOUT,CINDEX(10)
      COMMON/PRMTR/WAVSTRT,ANGSTRT,THSTRT(10),WAVEND,ANGEND,THEND(10)
     1   ,WAVDLTA,ANGDLTA,THDLTA(10)
      EQUIVALENCE (PARAM(1),WAVNUM),(PSTRT(1),WAVSTRT),(PEND(1),
     1    WAVEND),(PDLTA(1),WAVDLTA),(FOUT(1),RTE)
      PRINT 100, IL
  100 FORMAT (////,17X,*   REFLECTIVITY       TRANSMISSIVITY      ABSORP
     1TIVITY   *,/,* WAVNUM  ANGLE       TE        TM         TE       TM
     2      TE        TM            EXIT INDEX      LAYER NO.*,I2,* INDEX
     3AND THICKNESS*,/)
  200 CONTINUE
      IF (KAVRG .GE. 1) GO TO 300
      CALL RTA
      PRINT 210, WAVNUM,ANGLE,RTE,RTM,TTE,TTM,ATE,ATM,CINDOUT
     1   ,CINDEX(IL),THICK(IL)
  210 FORMAT (1X,F6.1,1X,F8.5,1X,3(1X,1P2G9.2),1X,5(1X,1PG9.2))
      GO TO 400
  300 CALL ANGAVRG(KPRNT)
      PRINT 310, WAVNUM,      RTE,RTM,TTE,TTM,ATE,ATM,CINDOUT
     1   ,CINDEX(IL),THICK(IL)
  310 FORMAT (1X,F6.1,1X,*AVERAGED*,1X,3(1X,1P2G9.2),1X,5(1X,1PG9.2))
  400 PARAM(IX)=PARAM(IX)+PDLTA(IX)
      IF (PARAM(IX) .LE. PEND(IX)) GO TO 200
      PARAM(IX)=PSTRT(IX)
      IF (IY .LT. 1) GO TO 1000
      PARAM(IY)=PARAM(IY)+PDLTA(IY)
      IF (PARAM(IY) .LE. PEND(IY)) GO TO 200
      PARAM(IY)=PSTRT(IY)
 1000 CONTINUE
      RETURN  $  END
C
C
      SUBROUTINE XYZPRNT(KAVRG,IX,IY,IZ,IL)
      DIMENSION Y(20),Z(20)
      COMMON /JLABELS/JPARAM(3),JOUT(6)
      DIMENSION PARAM(12),PSTRT(12),PEND(12),PDLTA(12),FOUT(6)
```

```
      COMPLEX CINDIN,CINDOUT,CINDEX
      COMMON/LAYDATA/WAVNUM,ANGLE,THICK(10),RTE,RTM,TTE,TTM,ATE,ATM
     1   ,NUMLAY,INDIN,D1IN,D2IN,INDOUT,D1OUT,D2OUT,IND(10),D1(10)
     2   ,D2(10),CINDIN,CINDOUT,CINDEX(10)
      COMMON/PRMTR/WAVSTRT,ANGSTRT,THSTRT(10),WAVEND,ANGENC,THEND(10)
     1   ,WAVDLTA,ANGDLTA,THDLTA(10)
      EQUIVALENCE (PARAM(1),WAVNUM),(PSTRT(1),WAVSTRT),(PEND(1),
     1    WAVEND),(PDLTA(1),WAVDLTA),(FOUT(1),RTE)
      DATA JOUT/10H RFLCT TE ,10H RFLCT TM ,10H TRANS TE ,
     1  10H TRANS TM ,10H ABSORB TE,10H ABSORB TM/
      DATA JPARAM/10H  WAVNUM   ,10H ANGLE     ,10H THICKNESS /
      IF (IY .LT. 1) IY=1
      PRINT 100, JOUT(IZ)
  100 FORMAT (1H1,10X,* INTENSITY PLOT OF *,A10)
      IF (IY .GT. 2) PRINT 110,IL
  110 FORMAT (//,20X,* THICKNESS OF LAYER NO. *,I2)
      IF (IY .LE. 2) PRINT 120, JPARAM(IY)
  120 FORMAT (//,2X,A10)
      PARAM(IY)=PSTRT(IY)
      DO 200 I=1,20
      Y(I)=PARAM(IY)
      PARAM(IY)=PARAM(IY)+PDLTA(IY)
      IF (PARAM(IY) .GT. PEND(IY)) GO TO 300
  200 CONTINUE
  300 IEND=I
      PARAM(IY)=PSTRT(IY)
      PRINT 310, (Y(I),I=1,IEND,2)
  310 FORMAT (8X,10(1PG10.3,2X))
      PRINT 320, (Y(I),I=2,IEND,2)
  320 FORMAT (14X,10(1PG10.3,2X))
      PRINT 330, JPARAM(IX)
  330 FORMAT (1X,A10)
  350 CONTINUE
      DO 400 I=1,IEND
      PARAM(IY)=Y(I)
      IF(KAVRG .GE. 1) CALL ANGAVRG(0)
      IF (KAVRG .LT. 1) CALL RTA
      Z(I)=FOUT(IZ)
  400 CONTINUE
      PRINT 410, PARAM(IX),(Z(I),I=1,IEND)
  410 FORMAT (1X,1PG9.2,1X,0P20F6.4)
      PARAM(IX)=PARAM(IX)+PDLTA(IX)
      IF (PARAM(IX) .LE. PEND(IX)) GO TO 350
      PARAM(IX)=PSTRT(IX)
      PARAM(IY)=PSTRT(IY)
      RETURN  $  END
C
C
      SUBROUTINE PLOTFIL(IX,IZ,IL,KPRNT,KAVRG)
      COMMON /PLTINFO/ X(1000),Z(1000)
      COMMON /JLABELS/JPARAM(3),JOUT(6)
      COMMON /JDATA/ JTITLE(8),JIDENT(4)
      DIMENSION PARAM(12),PSTRT(12),PEND(12),PDLTA(12),FOUT(6)
      COMPLEX CINDIN,CINDOUT,CINDEX
      COMMON/LAYDATA/WAVNUM,ANGLE,THICK(10),RTE,RTM,TTE,TTM,ATE,ATM
     1   ,NUMLAY,INDIN,D1IN,D2IN,INDOUT,D1OUT,D2OUT,IND(10),D1(10)
     2   ,D2(10),CINDIN,CINDOUT,CINDEX(10)
      COMMON/PRMTR/WAVSTRT,ANGSTRT,THSTRT(10),WAVEND,ANGENC,THEND(10)
     1   ,WAVDLTA,ANGDLTA,THDLTA(10)
      EQUIVALENCE (PARAM(1),WAVNUM),(PSTRT(1),WAVSTRT),(PEND(1),
     1    WAVEND),(PDLTA(1),WAVDLTA),(FOUT(1),RTE)
      IF (IX .LE. 2) PRINT 100, JOUT(IZ),JPARAM(IX)
```

```
  100 FORMAT (///,5X,* PLOT OF *,A10,* AS A FUNCTION OF *,A10)
      IF (IX .GT. 2) PRINT 110, JOUT(IZ),IL
  110 FORMAT (///,5X,* PLOT OF *,A10,* AS A FUNCTION OFTHE THICKNESS OF
     1 LAYER NO. *,I2)
      IXAXIS=0
  200 IXAXIS=IXAXIS+1
      IF (KAVRG .GE. 1) CALL ANGAVRG(0)
      IF (KAVRG .LT. 1) CALL RTA
      X(IXAXIS)=PARAM(IX)
      Z(IXAXIS)=FOUT(IZ)
      PARAM(IX)=PARAM(IX)+PDLTA(IX)
      IF (PARAM(IX) .LE. PEND(IX)) GO TO 200
      PARAM(IX)=PSTRT(IX)
      CALL SKETCH(IXAXIS,X,Z,JTITLE,JIDENT)
      RETURN  $  END
C
C
      SUBROUTINE LOGPLOT(IZ,KPRNT)
      COMMON /PLTINFO/ X(1000),Z(1000)
      COMMON /JLABELS/JPARAM(3),JOUT(6)
      COMMON /JDATA/ JTITLE(8),JIDENT(4)
      DIMENSION PARAM(12),PSTRT(12),PEND(12),PDLTA(12),FOUT(6)
      COMPLEX CINDIN,CINDOUT,CINDEX
      COMMON/LAYDATA/WAVNUM,ANGLE,THICK(10),RTE,RTM,TTE,TTM,ATE,ATM
     1   ,NUMLAY,INDIN,D1IN,D2IN,INDOUT,D1OUT,D2OUT,IND(10),D1(10)
     2   ,D2(10),CINDIN,CINDOUT,CINDEX(10)
      COMMON/PRMTR/WAVSTRT,ANGSTRT,THSTRT(10),WAVEND,ANGEND,THEND(10)
     1   ,WAVDLTA,ANGDLTA,THDLTA(10)
      EQUIVALENCE (PARAM(1),WAVNUM),(PSTRT(1),WAVSTRT),(PEND(1),
     1    WAVEND),(PDLTA(1),WAVDLTA),(FOUT(1),RTE)
      PI=4.0*ATAN(1.0)
      PRINT 100, JOUT(IZ),JPARAM(2)
  100 FORMAT (///,5X,* PLOT OF *,A10,* AS A FUNCTION OF *,A10)
      IL=1
      PRINT 105, IL
  105 FORMAT (////,17X,*   REFLECTIVITY        TRANSMISSIVITY       ABSORP
     1TIVITY    *,/,* WAVNUM  ANGLE        TE        TM         TE        TM
     2       TE         TM            EXIT INDEX       LAYER NO.*,I2,* INDEX
     3AND THICKNESS*,/)
      IF (ANGSTRT .EQ. 0) ANGSTRT=ANGDLTA
      GANG =ANGSTRT
      FACTOR=1.0+ANGDLTA/ANGSTRT
      IXAXIS=0
  200 IXAXIS=IXAXIS+1
      ANGLE=(PI/2.0)-GANG
      CALL RTA
      PRINT 110, WAVNUM,ANGLE
     1   ,RTE,RTM,TTE,TTM,ATE,ATM,CINDOUT,CINDEX(1),THICK(1)
  110 FORMAT (1X,F6.1,1X,F8.5,1X,3(1X,1P2G9.2),1X,5(1X,1PG9.2))
      X(IXAXIS)=GANG
      Z(IXAXIS)=FOUT(IZ)
      GANG=GANG*FACTOR
      IF (GANG .LE. ANGEND) GO TO 200
      CALL SKETCH(IXAXIS,X,Z,JTITLE,JIDENT)
      RETURN  $  END
C
C
      SUBROUTINE ANGAVRG(KPRNT)
      COMPLEX CINDIN,CINDOUT,CINDEX
      COMMON/LAYDATA/WAVNUM,ANGLE,THICK(10),RTE,RTM,TTE,TTM,ATE,ATM
     1   ,NUMLAY,INDIN,D1IN,D2IN,INDOUT,D1OUT,D2OUT,IND(10),D1(10)
     2   ,D2(10),CINDIN,CINDOUT,CINDEX(10)
```

```
      COMMON/PRMTR/WAVSTRT,ANGSTRT,THSTRT(10),WAVEND,ANGEND,THEND(10)
     1   ,WAVDLTA,ANGDLTA,THDLTA(10)
      DIMENSION FOUT(6),TOTZ(6)
      EQUIVALENCE (RTE,FOUT(1))
      PI=4.0*ATAN(1.0)
      DO 50 I=1,6
   50 TOTZ(I)=0.0
      TOTOMGA=0.0
      ANGLE=ANGSTRT
  100 CALL RTA
      IF (KPRNT .EQ. 3) PRINT 110, WAVNUM,ANGLE
     1   ,RTE,RTM,TTE,TTM,ATE,ATM,CINDOUT,CINDEX(1),THICK(1)
  110 FORMAT (1X,F6.1,1X,F8.5,1X,3(1X,2E9.2),1X,5(1X,E9.2))
      DOMGA=2.0*PI*COS(ANGLE)*SIN(ANGLE)
      DO 200 I=1,6
  200 TOTZ(I)=TOTZ(I)+DOMGA*FOUT(I)
      TOTOMGA=TOTOMGA+DOMGA
      ANGLE=ANGLE+ANGDLTA
      IF (ANGLE .LE. ANGEND) GO TO 100
      IF (TOTOMGA .EQ. 0.0) GO TO 1000
      DO 300 I=1,6
  300 FOUT(I)=TOTZ(I)/TOTOMGA
 1000 CONTINUE
      RETURN  $  END
C
C
      SUBROUTINE RTA
      COMPLEX CINDIN,CINDOUT,CINDEX
      COMMON/LAYDATA/WAVNUM,ANGLE,THICK(10),RTE,RTM,TTE,TTM,ATE,ATM
     1   ,NUMLAY,INDIN,D1IN,D2IN,INDOUT,D1OUT,D2OUT,IND(10),D1(10)
     2   ,D2(10),CINDIN,CINDOUT,CINDEX(10)
      CALL COMIND(INDIN,D1IN,D2IN,WAVNUM,1.0,CINDIN)
      CALL COMIND(INDOUT,D1OUT,D2OUT,WAVNUM,1.0,CINDOUT)
      IF (NUMLAY .LT. 1) GO TO 200
      DO 100 J=1,NUMLAY
      CALL COMIND(IND(J),D1(J),D2(J),WAVNUM,THICK(J),CINDEX(J))
  100 CONTINUE
  200 CONTINUE
      CALL OPTICS(NUMLAY,CINDIN,CINDOUT,CINDEX,ANGLE,WAVNUM,THICK
     1   ,1,RTE,TTE,ATE)
      CALL OPTICS(NUMLAY,CINDIN,CINDOUT,CINDEX,ANGLE,WAVNUM,THICK
     1  ,-1,RTM,TTM,ATM)
      RETURN  $  END
C
C
      SUBROUTINE OPTICS(NUMLAY,CINDIN,CINDOUT,CINDEX,ANGLE,WAVNUM,
     1   THICK,MODE,R,T,A)
      COMPLEX CINDEX(1),CMAT1(2,2),CMAT2(2,2),CMAT3(2,2),COMSIN(1),
     1   CINDIN,CINDOUT,CSININ,CSINOUT
      DIMENSION THICK(1)
      CMAT1(1,1)=1.0
      CMAT1(1,2)=0
      CMAT1(2,1)=0
      CMAT1(2,2)=1.0
      CSININ=CSIN(CMPLX(ANGLE,0.0))
      CSINOUT=CINDIN*CSININ/CINDOUT
      DO 100 LNUM=1,NUMLAY
      IF (NUMLAY .LT. 1) GO TO 300
  100 COMSIN(LNUM)=CINDIN*CSININ/CINDEX(LNUM)
      DO 200 LNUM=1,NUMLAY
      CALL MATRIX(WAVNUM,THICK(LNUM),CINDEX(LNUM),COMSIN(LNUM),
     1   MODE,CMAT2)
```

```
      CALL MULTI(CMAT1,CMAT2,CMAT3)
      CMAT1(1,1)=CMAT3(1,1)
      CMAT1(1,2)=CMAT3(1,2)
      CMAT1(2,1)=CMAT3(2,1)
      CMAT1(2,2)=CMAT3(2,2)
  200 CONTINUE
  300 CALL RESULT(CMAT1,MODE,CSININ,CSINOUT,CINDIN,CINDOUT,R,T,A)
      RETURN  $  END
C
C
      SUBROUTINE CCMIND(I,D1,D2,WAVNUM,THICK,CINDEX)
      COMPLEX CINDEX
      DATA CLIGHT/2.997925E+10/
C***I=0 COMPLEX INDEX GIVEN
      IF (I .EQ. 0) CINDEX=CMPLX(D1,D2)
C***I=1 COMPLEX DIELECTRIC GIVEN
      IF (I .EQ. 1) CINDEX=CSQRT(CMPLX(D1,D2))
C***I=2 REAL DIELECTRIC AND CONDUCTIVITY GIVEN
      IF (I .EQ. 2) CINDEX=CSQRT(CMPLX(D1,2.0*D2/(WAVNUM*CLIGHT)))
C***I=3 CONDUCTIVITY GIVEN
      IF (I .EQ. 3) CINDEX=CMPLX(SQRT(D2/(WAVNUM*CLIGHT)),
     1                           SQRT(D2/(WAVNUM*CLIGHT)))
C***I=4 OHMS PER SQUARE GIVEN
      IF (I .EQ. 4) CINDEX=CMPLX(SQRT(30.0/(D1*WAVNUM*THICK)),
     1                           SQRT(30.0/(D1*WAVNUM*THICK)))
C***I=5 ANOMALOUS SKIN EFFECT FROM DINGLE
      IF (I .EQ. 5) CALL ASKIN(WAVNUM,D1,D2,CINDEX)
      RETURN  $  END
C
C
      SUBROUTINE ASKIN(WNUM,COND,EDENS,CINDEX)
      COMPLEX CINDEX,X1,X2,X3,DUM,ADMNOR,ADM
      DATA CLIGHT,EMASS,ECHRG,PLANCK/2.997925E+10,9.109558E-28
     1   ,4.80325E-10,1.0545919E-27/
      PI=4.0*ATAN(1.0)
      FREQ=WNUM*CLIGHT
      TAU=SQRT(3.0*PI*EMASS/(EDENS*ECHRG*ECHRG))
      VFERMI=(3.0*PI*PI*EDENS)**(1.0/3.0)*PLANCK/EMASS
      VNOR=VFERMI/CLIGHT
      FREQNOR=FREQ*TAU*2.0/(3.0*VNOR)
      CONNOR=COND*TAU*VNOR
      ALPHA=FREQNOR*(CONNOR**3)
      X3=CMPLX(1.0,FREQNOR*CONNOR)
      X2=CMPLX(0.0,ALPHA)
      X1=X2/(X3*X3*X3)
      X2=CSQRT(X1)
      X3=CEXP(CLOG(X1*PI)/3.0)
      IF (CABS(X1) .LE. 0.8)
     1   DUM=1.1547*X2-0.2500*X1+0.1540*X2**3-0.1262*X1*X1
     2   +0.1188*X2**5-0.1214*X1**3+0.1307*X2**7-0.148*X1**4
     3   +0.1685*X2**9
      IF (CABS(X1) .GT. 0.8)
     1   DUM=1.1547*X3-0.1351*CLOG(PI*X1)-0.5330+0.0416/X3
     2   -0.0649/(X3*X3)+1.0/(PI*X1)
      ADMNOR=      (0.0,-1.0)*DUM*CMPLX(1.0,CONNOR*FREQNOR)
      ADM=ADMNOR*CLIGHT/(4.0*PI*FREQNOR*CONNOR*VNOR)
      CINDEX=4.0*PI*ADM/CLIGHT
      CINDEX=CONJG(CINDEX)
      RETURN
      END
C
C
```

```
      SUBROUTINE MATRIX(WAVN,THICK,CN,CSINE,MODE,CMAT)
      COMPLEX CN,CMAT(2,2),CNCOS,CBETA,CI,CSINE
      CI=(0.0,1.0)
      PI=3.1415927
      CNCOS=CSQRT(1-CSINE**2)*CN**MODE
      CBETA=2*PI*WAVN*THICK*CN*CSQRT(1-CSINE**2)
      CMAT(1,1)=CCOS(CBETA)
      CMAT(1,2)=-CI*CSIN(CBETA)/CNCOS
      CMAT(2,1)=-CI*CSIN(CBETA)*CNCOS
      CMAT(2,2)=CCOS(CBETA)
      RETURN
      END
C
C
      SUBROUTINE MULTI(CMAT1,CMAT2,CMAT3)
      COMPLEX CMAT1(2,2),CMAT2(2,2),CMAT3(2,2)
      CMAT3(1,1)=CMAT1(1,1)*CMAT2(1,1)+CMAT1(1,2)*CMAT2(2,1)
      CMAT3(1,2)=CMAT1(1,1)*CMAT2(1,2)+CMAT1(1,2)*CMAT2(2,2)
      CMAT3(2,1)=CMAT1(2,1)*CMAT2(1,1)+CMAT1(2,2)*CMAT2(2,1)
      CMAT3(2,2)=CMAT1(2,1)*CMAT2(1,2)+CMAT1(2,2)*CMAT2(2,2)
      RETURN
      END
C
C
      SUBROUTINE RESULT(CMAT,MODE,CSINI,CSINE,CNI,CNE,R,T,A)
      COMPLEX CMAT(2,2), CR, CT, CA, CB, CNCOSI, CNCOSE
     1, CSINI, CSINE, CNI, CNE
      CNCOSI=CSQRT(1-CSINI**2)*CNI**MODE
      CNCOSE=CSQRT(1-CSINE**2)*CNE**MODE
      CA=(CMAT(1,1)+CMAT(1,2)*CNCOSE)*CNCOSI
      CB=CMAT(2,1)+CMAT(2,2)*CNCOSE
      CR=(CA-CB)/(CA+CB)
      R=CABS(CR)**2
      CT=2*CNCOSI/(CA+CB)
      T=CABS(CT)**2*REAL(CNCOSE)/REAL(CNCOSI)
      A=1-R-T
      RETURN
      END
C
C
      SUBROUTINE SKETCH(NPTS,X,Y,JTITLE,JIDENT)
      DIMENSION X(1),Y(1),JTITLE(8),JIDENT(4)
      COMMON /PLOTCAT/XS,XL,YS,YL,XLOG,YLOG,A(2050),B(2050)
      COMMON/CCPOCL/XMIN,XMAX,YMIN,YMAX,CCXMIN,CCXMAX,CCYMIN,CCYMAX
      COMMON/CCFACT/FACTOR
      DIMENSION ICONT(5),IREAD(8),JXLABEL(8),JYLABEL(8),NREAD(8)
      FACTOR=100.0
      PRINT 50, NPTS,JTITLE,JIDENT
   50 FORMAT (//,5X,I4,12A10)
      NGRF=NPTS
      READ 110, IREAD
  110 FORMAT (8A10)
      PRINT 115, IREAD
  115 FORMAT (10X,8A10)
      IF (IREAD(1) .EQ. 10HNO PLOT     ) GO TO 900
      IF (IREAD(1) .EQ. 10H            ) GO TO 900
      IF (IREAD(1) .EQ. 10HSAME PLOT   ) GO TO 200
      IF (IREAD(1) .EQ. 10HSAME SET    ) GO TO 150
      READ 110, NREAD
      PRINT 115, NREAD
      DECODE (80,120,NREAD(1)) XS,XL,YS,YL,XLOG,YLOG
  120 FORMAT (6E10.3)
```

```
      READ 110, NREAD
      PRINT 115, NREAD
      DECODE(80,120,NREAD(1)) CCXMIN,CCXMAX,CCYMIN,CCYMAX
      XMIN=XS
      XMAX=XL
      YMIN=YS
      YMAX=YL
      IF (XLOG .GT. 0.0) XMIN=ALOG10(XS)
      IF (XLOG .GT. 0.0) XMAX=ALOG10(XL)
      IF (YLOG .GT. 0.0) YMIN=ALOG10(YS)
      IF (YLOG .GT. 0.0) YMAX=ALOG10(YL)
      IF (IREAD(1) .EQ. 10HNEW RANGES ) GO TO 200
      DECODE(70,100,IREAD(2))
     1                    LABYORN,ITITSZ,ITITCHR,IIDSZ,IIDCHR,TITX,TITY
     1    ,ZIDX,ZIDY
  100 FORMAT (    A6,4I4,4E10.3)
      READ 110, NREAD
      PRINT 115, NREAD
      DECODE(80,130,NREAD(1)) NX1,NX2,NX3,IXSZ,IXCHR,XLABX,XLABY
      READ 110, NREAD
      PRINT 115, NREAD
      DECODE(80,130,NREAD(1)) NY1,NY2,NY3,IYSZ,IYCHR,YLABX,YLABY
  130 FORMAT (5I4,2E10.3)
      READ 110, NREAD
      PRINT 115, NREAD
      DECODE(80,110,NREAD(1)) JXLABEL
      READ 110, NREAD
      PRINT 115, NREAD
      DECODE(80,110,NREAD(1)) JYLABEL
  150 CALL CCNEXT
  180 CALL CCGRID(NX1,NX2,NX3,LABYORN,NY1,NY2,NY3)
      CALL CCLTR(XLABX,XLABY,0,IXSZ,JXLABEL,IXCHR)
      CALL CCLTR(YLABX,YLABY,1,IYSZ,JYLABEL,IYCHR)
      CALL CCLTR(TITX,TITY,0,ITITSZ,JTITLE,ITITCHR)
      CALL CCLTR(ZIDX,ZIDY,0,IIDSZ,JIDENT,IIDCHR)
  200 CONTINUE
      IF (IREAD(1) .EQ. 10HPLOT GRID    ) GO TO 900
  400 CALL LIMITS(NGRF,X,Y)
      CALL CCPLOT(A,B,NGRF,4HJOIN,0,0)
      PRINT 410, NGRF,XS,XMIN,XL,XMAX,YS,YMIN,YL,YMAX
  410 FORMAT (5X,I4,* POINTS PLOTTED  *,8E11.3)
  900 CONTINUE
      RETURN  $  END
C
C
      SUBROUTINE LIMITS(NPTS,X,Y)
      DIMENSION X(1),Y(1)
      COMMON /PLOTCAT/XS,XL,YS,YL,XLOG,YLOG,A(2050),B(2050)
      COMMON/CCPOOL/XMIN,XMAX,YMIN,YMAX,CCXMIN,CCXMAX,CCYMIN,CCYMAX
      J=0
      DO 200 I=1,NPTS
      XX=X(I)
      IF (XX .LT. XS) GO TO 200
      IF (XX .GT. XL) GO TO 300
      IF (J .GE. 2050) GO TO 250
      J=J+1
      A(J)=X(I)
      IF (XLOG .GT. 0.0) A(J)=ALOG10(A(J))
      B(J)=Y(I)
      IF (B(J) .LT. YS) B(J)=YS
      IF (B(J) .GT. YL) B(J)=YL
      IF (YLOG .GT. 0.0) B(J)=ALOG10(B(J))
```

```
  200 CONTINUE
      GO TO 300
  250 PRINT 270, J
  270 FORMAT (/////,5X,* TOO MANY POINTS, FIRST *,I6,* WERE USED*,///)
  300 NPTS=J
      RETURN  $  END
C****** 789 CARD
C
C***** CONTROL CARDS WHICH PRODUCED PLOT IN FIGURE II.6
C
 EMISSIVITY AS A FUNCTION OF ANGLE FOR BARE COPPER
 0 2 0 3 0 2 2
 10.0
 1.0  E-041.57079633 0.1  E-04
 0 1.0        0.0
 5 5.39 E+17 8.5  E+22
NEW PLOT  NOLBLS   2  80   1  40 0.0        10.2       0.0        10.4
 1.0  E-041.57079633 1.0  E-04 1.0        1.0        1.0
 1.0        8.76       1.0        8.40
   1   1   1   2  80 1.0        0.1
   1   4   1   2  40 0.0        1.1
 ANGLE FROM GRAZING INCIDENCE (RADIANS)
 EMISSIVITY
 EMISSIVITY AS A FUNCTION OF ANGLE FOR BARE COPPER
 0 2 0 4 0 2 2
 10.0
 1.0  E-041.57079633 0.1  E-04
 0 1.0        0.0
 5 5.39 E+17 8.5  E+22
SAME PLOT
 EMISSIVITY AS A FUNCTION OF ANGLE FOR  DIELECTRIC  COATED COPPER
 1 2 0 3 0 2 2
 10.0
 1.0  E-041.57079633 0.1  E-04
 0 1.0        0.0
 5 5.39 E+17 8.5  E+22
 0 1.5        0.0        0.00508
SAME PLOT
 EMISSIVITY AS A FUNCTION OF ANGLE FOR  DIELECTRIC  COATED COPPER
 1 2 0 4 0 2 2
 10.0
 1.0  E-041.57079633 0.1  E-04
 0 1.0        0.0
 5 5.39 E+17 8.5  E+22
 0 1.5        0.0        0.00508
SAME PLOT
```

APPENDIX C

Superfluid Helium Pump

We have developed a simple pump for transporting superfluid helium inside our crystat. It operates on the superfluid fountain effect which is briefly described in section E of chapter II. The pump is capable of pumping 3 liters of liquid helium per hour a height of 1 meter while dissipating less than 0.1 Watts of heat in the bath.

The pump is very easy to construct. Figure C.1 is a scale drawing of the device. The lower inlet chamber is machined out of Lava Stone™ (American Lava Company). This is a ceramic material which is porous to the superfluid component of liquid helium but impervious to the normal component. It is an easily machined material before being fired which turns into a hard ceramic after firing. The heater in the chamber is a metal film resistor used to establish the temperature gradient required to run the pump. Glass tubing is used to convey the helium to the desired location. The various parts are fastened together with Miller-Stephenson 907 epoxy. The only part that requires any care is the exit nozzle in the glass tube. This nozzle must offer enough gas flow impedence that the desired temperature gradient (and thus a corresponding gradient for the vapor pressure) can be achieved without excessive power dissipation. We found empirically that an aperture of $\approx$.7 mm worked well. None of the other dimensions are critical.

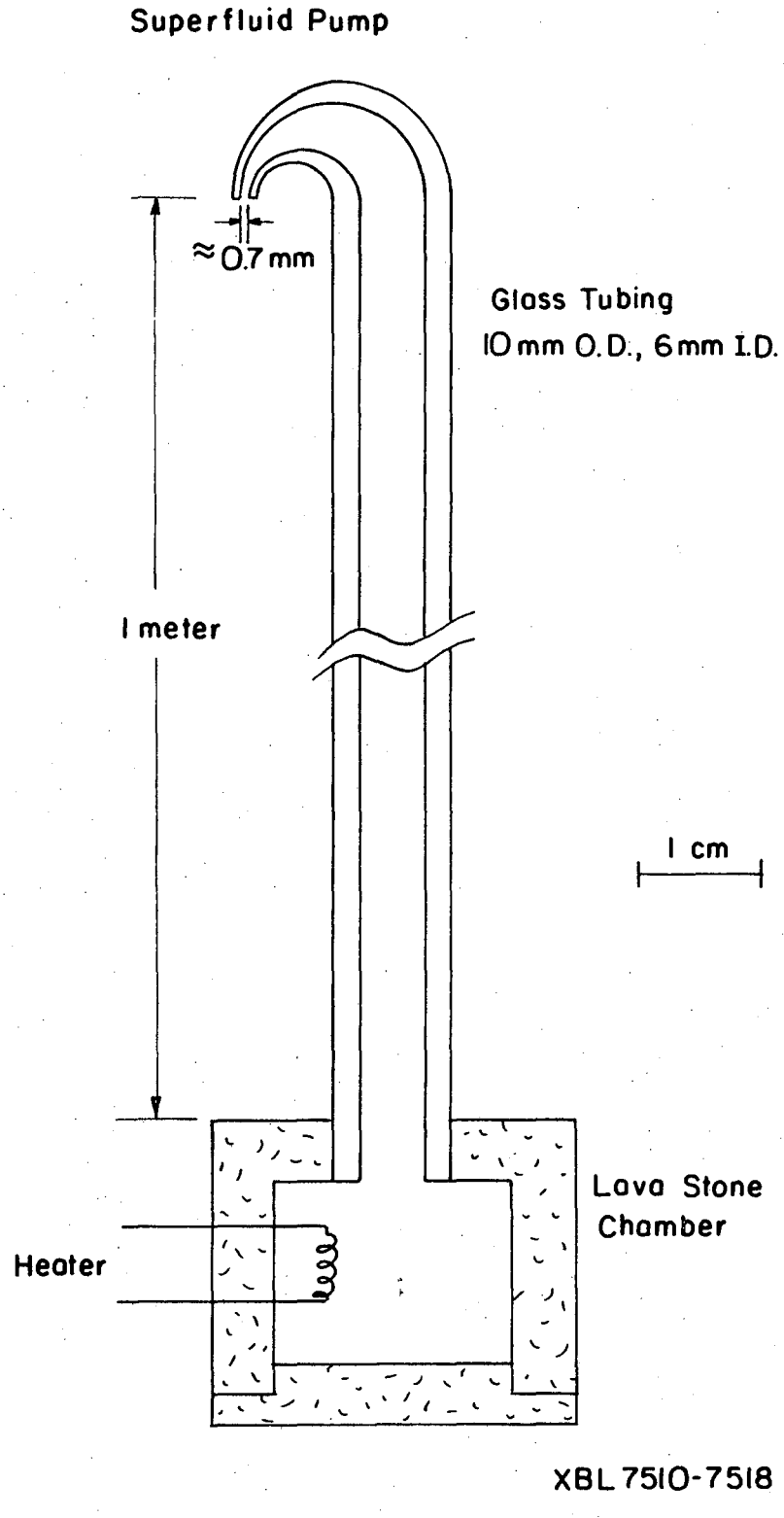

Fig. C.1. Scale drawing of superfluid helium pump.

ACKNOWLEDGEMENTS

I am greatly indebted to my thesis adviser, Paul L. Richards. He initiated this project and provided invaluable assistance and advice. His conscientiousness and patience made him an excellent adviser. Dr. John C. Mather was my partner in developing the spectrophotometer. His ability to identify and critically analyze the problems in the measurement was important to our success. Norman S. Nishioka assisted in the environmental testing and operation of the apparatus. He also provided the expertise in computing required for the data analysis. I want to thank especially Henry Primbsch whose assistance and expertise in electronics and ballooning proved to be indispensable. His enthusiasm and friendly disposition made the experiment more enjoyable. I want to thank Dr. Richard Aurbach for interfacing our experiment to the PDP-11 computer. I want to thank Prof. Kinsey Anderson for his support of our ballooning program.

This work was done under the auspices of the U.S. Energy Research and Developement Administration. Parts of this work were supported by National Aeronautics and Space Administration grant NGL05-003-497.

REFERENCES

R. A. Alpher and R. Herman, Nature 162, 774 (1948).

L. Alvarez, et al., "Aether Drift and the Isotropy of the Universe," research proposal, University of California Space Sciences Laboratory and Lawrence Berkeley Laboratory, 1974.

R. J. Bell, Introduction Fourier Transform Spectroscopy, (Academic Press, New York; 1972).

A. G. Blair, et al., Phys. Rev. Lett. 27, 1154 (1971).

M. Born and E. Wolf, Principles of Optics (Pergamon Press, New York; 1970), 4th edition.

V. Bortolot, J. Clauser, P. Thaddeus, Phys. Rev. Lett. 22, 307 (1969).

J. P. Casey and E. A. Lewis, J. Opt. Soc. Am., 42, 971 (1952).

J. Chamberlain and H. A. Gebbie, Infrared Phys. 11, 57 (1971).

K. Chan and B. Jones, Astrophys. J. 195, 1 (1975).

K. Chan and B. Jones, Astrophys. J. 195, 245 (1975).

R. Dicke, P. Peebles, P. Roll, and D. Wilkinson, Astrophys. J. 142, 414 (1965).

R. B. Dingle, Physica 19, 311 (1953).

P. Fellgett, J. Phys. Radium 19, 187 (1958).

H. A. Gebbie, W. J. Burroughs, and G. R. Bird, Proc. Roy. Soc. A. 310, 579 (1969).

R. M. Goody, Atmospheric Radiation, vol. I, (Oxford at the Clarendon Press; 1964).

D. Goorwitch, Appl. Optics 4, 1387 (1975).

J. Gott, J. Gunn, D. Schramm, and B. Tinsley, Astrophys. J. 194, 543 (1974).

Handbook of Geophysics, C. Z. Campen, et al., Ed. (MacMillan Company, New York; 1961).

D. Heggi, W. Traub, N. Carleton, Astrophys. J., 190, 543 (1974).

J. R. Houck and M. Harwit, Astrophys. J. 157, L45 (1969).

J. R. Houck, B. L. Soifer, M. Harwit, J. L. Pipher, Astrophys. J. 178, L29 (1972).

J. D. Jackson, Classical Electrodynamics (John Wiley and Sons, Inc., New York; 1967).

J. B. Keller, J. Opt. Soc. Am. 52, 116 (1962).

C. Kittel, Introduction to Solid State Physics, (John Wiley and Son, New York; 1966) 3rd edition.

D. H. Martin and F. Puplett, Infrared Phys. 10, 105 (1969).

J. C. Mather, Ph.D. thesis, University of California, LBL-2258 (1974).

J. C. Mather, P. L. Richards, D. P. Woody, IEEE Trans. Microwave Theory Tech. 22, 1046 (1974).

R. A. McClathchey et al., Air Force Cambridge Research Laboratory Atmospheric Absorption Line Parameters Compilation, AFCRL-TR-73-0096, Environmental Research Papers No. 434 (1973).

M. L. Meeks and A. E. Lilley, J. Geophys. Res. 68, 1683 (1963).

C. Misner, K. Thorne, and J. Wheeler, Gravitation (W. H. Freeman and Comp., San Francisco; 1973).

K. D. Möller and W. G. Rothschild, Far-Infrared Spectroscopy (John Wiley and Sons, Inc., New York; 1971).

D. Muehlner and R. Weiss, Phys. Rev. Lett, 24, 742 (1970).

D. Muehlner and R. Weiss, Phys. Rev. D 7, 326 (1973).

D. Muehlner and R. Weiss, Phys. Rev. Lett. 30, 757 (1973).

P. Noerdlinger, Phys. Rev. Lett. 30, 781 (1973).

P. J. E. Peebles, Physical Cosmology (Princeton University Press, New Jersey; 1971).

A. Penzias and R. Wilson, Astrophys. J. 142, 419 (1965).

J. L. Pipher, J. R. Houck, B. W. Jones, and M. Harwit, Nature 231, 375 (1971).

A. B. Pippard, Advances in Electronics and Electron Physics (Academic Press, New York, 1954), vol. 6, p. 1.

G. E. H. Reuter and E. H. Sondheimer, Proc. Roy. Soc. A 195, 336 (1948).

P. L. Richards, Spectroscopic Techniques, D. H. Martin Ed. (North-Holland Publishing Comp., Amsterdam; 1967), p. 33.

E. Robson, D. Vickers, J. Huizinga, J. Beckman, and P. Clegg, Nature 251, 591 (1974).

K. Shivanandan, J. R. Houck, M. O. Harwit, Phys. Rev. Lett. 21, 1460 (1968).

J. M. Stone, Radiation and Optics (McGraw-Hill Book Comp., New York; 1963).

R. Tolman, Relativity, Thermodynamics, and Cosmology (Oxford at the Clarendon Press; 1934).

U. S. Standard Atmosphere Supplement, Environmental Science Services Administration, National Aeronautics and Space Administration (1966).

A. N. Vystavkin, V. N. Gubanhov, V. N. Listvin, and V. V. Migulin, Proc. Polytech. Inst. Brooklyn Conf. Submillimeter Waves, J. Fox, Ed. (Polytechnic Press, New York; 1971) vol. 20, p. 321.

S. Weinberg, Gravitation and Cosmology (John Wiley and Sons, Inc., New York; 1972.

J. Wilks, An Introduction to Liquid Helium (Clarendon Press, Oxford; 1970).

C. S. Williams, Appl. Optics 5, 1084 (1966).

K. D. Williamson et al., Nature Phys. Sci. 241, 79 (1973).

D. P. Woody, J. C. Mather, N. S. Nishioka, and P. L. Richards, Phys. Rev. Lett. 34, 1036 (1975).

TECHNICAL INFORMATION DIVISION
LAWRENCE BERKELEY LABORATORY
UNIVERSITY OF CALIFORNIA
BERKELEY, CALIFORNIA 94720